

## **ABSTRACT**

VEYTSKIN, YURIY BORISOVICH. Nanomechanics of Asphalt Binder and Mastic Viscoelasticity and Cohesion. (Under the direction of Dr. Christopher P. Bobko).

A need exists to develop accepted measurement techniques for characterizing the cohesive and linear viscoelastic properties of asphalt binder and mastic that can motivate, inform, and enable multiscale and macroscale modeling approaches. Efforts to develop better analytical models for asphalt binder and mastic behavior are challenged by various aspects of the multiscale nature of asphalt concrete, including small length scales, nonlinear material behavior, high cohesion, high heterogeneity at multiple length scales, and complexity in experimental methods to measure properties at the smaller length scales.

Nanoindentation, a widely used experimental technique for obtaining quantitative data on the mechanical properties of heterogeneous materials, addresses this need. This flexible probe-based technique is particularly well-suited for characterizing material properties of individual phases within complex composite materials. While most nanoindentation testing and analysis methods are focused on hard materials with the aim of determining the elastic modulus and hardness, this research considers the behaviors of more complicated materials including viscoelastic and cohesive behaviors.

Exploratory nanoindentation techniques for determining the viscoelastic and cohesive properties of Rolling Thin-Film Oven (RTFO) aged asphalt binders and mastics, with mineral and manufactured fillers and varying filler volumetric concentrations, are developed, tested, verified, and validated. New ways to calculate and interpret important viscoelastic and cohesive properties from nanoindentation data through low-load sphero-conical (blunt) nanoindentation are described. Microstructural observations from atomic force microscopy approaches are combined with information about mechanical properties for a variety of samples, shedding light on the nature of composite behaviors in asphalt mastics. Ultimately, improved characterization and modeling of asphalt binder and mastic as related to the bulk performance of asphalt concrete will enable improved material selection and engineering for longer infrastructure lifecycles.

© Copyright 2015 by Yuriy Borisovich Veytskin

All Rights Reserved

Nanomechanics of Asphalt Binder and Mastic Viscoelasticity and Cohesion

by  
Yuriy Borisovich Veytskin

A dissertation submitted to the Graduate Faculty of  
North Carolina State University  
in partial fulfillment of the  
requirements for the degree of  
Doctor of Philosophy

Civil Engineering

Raleigh, North Carolina

2015

APPROVED BY:

---

Dr. Christopher Bobko  
Chair of Advisory Committee

---

Dr. Cassie Castorena

---

Dr. Murthy Guddati

---

Dr. Y. Richard Kim

## **DEDICATION**

This dissertation is dedicated to my late grandmother Khaya Dobrushkina, great-aunt Tanya Stinsky, and dog Gabby, all of whom passed away during my tenure in graduate school since August 2010. This dissertation is also dedicated to the seventy year anniversary of Victory Day, on May 9, and to my grandparents who served in World War II.

## **BIOGRAPHY**

Yuriy Veytskin was born in Kharkov, Ukraine and immigrated with his family to the United States at the age of three. He attended A.C. Flora High School in Columbia, South Carolina and graduated with his B.S.E. in Civil & Environmental Engineering from Duke University in the spring of 2010. He then entered graduate school at North Carolina State University in the fall of 2010, earning his Master of Civil Engineering and spending a year down under in Melbourne, Australia en route to this PhD.

## **ACKNOWLEDGMENTS**

Thank you to my parents Boris Veytskin and Zhenya Krupnik, and my uncle Viktor, for supporting me throughout my doctoral program over the past five years. Thank you to my brother Igor and sister Olga for being brotherly and sisterly. Thank you to Dr. Bobko for being such a caring, insightful, perspicacious, patient, and easygoing mentor and advisor. I am deeply indebted to you for shaping me into the scientist and researcher who I am today, and I sincerely enjoyed the experience of learning from and collaborating with you. Thank you to my committee members for their continued guidance. Special thanks to Dr. Castorena for being such an easily accessible advisor with thoughtful input on the direction of the research. Thank you to my friends in graduate school, past and present, especially Isaac Kumar Isukapati, Vahid Zanjani Zadeh, Andrew Edwards, Machel Morrison, and Mehdi Mashayekhi. Special thanks to Isaac for the countless philosophical conversations and late night drives around Raleigh, North Carolina.

I would also like to acknowledge the financial support provided throughout my program by the Department of Civil, Construction, and Environmental Engineering at North Carolina State University. This research would not have been possible without the department's financial support.

## TABLE OF CONTENTS

LIST OF TABLES .....	viii
LIST OF FIGURES .....	ix
CHAPTER 1. INTRODUCTION .....	1
1.1 Industrial Context and Problem Statement.....	1
1.2 Intellectual Merit .....	4
1.3 Outline of Dissertation .....	5
CHAPTER 2. LITERATURE REVIEW .....	7
2.1 Asphalt Binder and Mastic Material Composition and Behavior .....	7
2.2 Viscoelastic Indentation and Nanoindentation on Asphalt .....	10
2.3 Atomic Force Microscopy for Adhesion and Cohesion Properties.....	12
CHAPTER 3. NANOINDENTATION APPROACH .....	16
3.1 Nanoindentation Overview .....	16
3.2 Creep Compliance and Nanoindentation.....	17
3.3 Cohesion and Nanoindentation .....	21
CHAPTER 4. MATERIALS & METHODS .....	29
4.1 Materials.....	29
4.2 Superpave Grading.....	30
4.3 Micrographs .....	31
4.4 Methods.....	33
4.4.1 Sample Preparation .....	33
4.4.2 CSM Instruments Ultra-Nanoindenter (UNHT).....	34
4.4.3 Experimental Methods for AFM.....	36
4.4.4 Experimental Challenges .....	37
4.5 Loading Procedures.....	38
4.5.1 Creep Loading Procedures and Commentary .....	38
4.5.2 Cohesion Loading Procedures and Commentary.....	43
CHAPTER 5. ANALYSIS FOR CREEP COMPLIANCE AND COHESION .....	45
5.1 Governing Equation for Creep .....	45

5.2	Generalized Power Law (GPL) .....	51
5.3	Modeling Scheme.....	53
5.4	Limitations of the Chosen Model.....	55
5.5	Analytic Formulations for Interconversions .....	57
5.5.1	Options for Interconversion to Shear Relaxation Modulus .....	57
5.5.2	Formulation for Interconversion to $ E^* $ Mastercurve.....	60
5.6	Analytic Formulation for Cohesion.....	62
CHAPTER 6. VISCOELASTIC RESULTS.....		66
6.1	Sample Creep Data.....	66
6.2	Results of Initial Trials: Creep Compliance Data Analysis .....	66
6.3	Results of Interconversions of Creep Compliance .....	70
6.3.1	Interconversion to Shear Relaxation Modulus.....	70
6.3.2	Interconversion to $ E^* $ Mastercurve .....	72
6.3.3	Potential Sources of Error.....	74
6.4	Results of RTFO-Aged Materials Creep Compliance Data Analysis .....	75
6.4.1	Extraction of Fitted Parameters .....	75
6.4.2	Linearity Check.....	78
6.4.3	Comparisons of Creep Compliance and Dynamic Modulus Results.....	80
6.4.4	Time-Scaling for Lower Temperature Tests.....	85
CHAPTER 7. COHESION RESULTS.....		88
7.1	Fillers and Representative Cohesion Data .....	88
7.2	Cohesion Results and Discussion.....	91
CHAPTER 8: AFM IMAGING.....		103
8.1	Microstructures from AFM Imaging.....	103
8.2	Image Processing Results.....	105
CHAPTER 9: DISCUSSION ON SYNTHESIS OF ALL RESULTS .....		110
9.1	Possible Reinforcement Mechanisms .....	111
9.1.1	Volume Filling in Mastics .....	111
9.1.2	Physicochemical Interactions.....	113

9.1.3 Particle Interactions .....	114
CHAPTER 10. CONCLUSIONS AND RESEARCH CONTRIBUTIONS .....	116
10.1 Summary of Main Findings .....	116
10.3 Future Perspectives / Future Research Beyond the Dissertation .....	119
REFERENCES .....	123
APPENDICES .....	132
APPENDIX A.....	133

## LIST OF TABLES

Table 1: All materials used in creep and cohesion testing.....	30
Table 2: The set of 15 creep loading programs used per sample.....	40
Table 3: Fitted creep compliance parameters for RTFO-aged materials.....	77
Table 4: DSR results for shift factors .....	86
Table 5: Fitted creep compliance parameters for RTFO-aged materials using DSR shift factors (for the materials available from DSR testing) .....	87
Table 6: Specific Surface Area .....	90
Table 7: Means and standard deviations for work of cohesion and penetration depth.....	93
Table 8: Number of bees and average bee size for all materials tested in AFM .....	107

## LIST OF FIGURES

Figure 1: Multi-scale representation of the constituents of asphalt concrete.....	9
Figure 2: Asphalt binder and filler micrographs (316 $\mu\text{m}$ by 242 $\mu\text{m}$ ): (a) PG 70-28 SBS binder; (b) PG 70-22 binder; (c) PG 64-22 binder; (d) PG 70-28 SBS binder after full recovery; (e) PG 64-22 binder after full recovery; (f) Baghouse fine granite dust (mineral); (g) Hydrated lime filler (manufactured) .....	32
Figure 3: (a) PG 70-22 pre-indentation; (b) PG 64-22 pre-indentation .....	33
Figure 4: Nanoindentation test set-up: (a) Schematic of indenter construction; (b) 0.635 cm height and 1.5875 cm radius sample holder (thimble) with binder; (c) UNHT module in operation .....	35
Figure 5: (a) typical rigid material curve; (b) binder cohesion curve; (c) binder creep curve	42
Figure 6: Sphero-conical indenter.....	45
Figure 7: Schematic of conical indenter geometry .....	48
Figure 8: Representative complex modulus mastercurve for binder and mastic .....	52
Figure 9: Schematic of numerical modeling approach for constitutive relation.....	55
Figure 10: Sample creep data: (a) 17000 $\mu\text{N}/\text{min}$ loading rate, 27 $\mu\text{N}$ max load; (b) Ramp-and-hold curve for (a); (c) 5000 $\mu\text{N}/\text{min}$ loading rate, 65 s hold time; (d) Ramp-and-hold curve for (c); (e) 59 $\mu\text{N}$ max load, 45 s hold time; (f) Ramp-and-hold curve for (e) .....	67
Figure 11: $h_c$ vs. $t$ and $h_c(t)^2$ vs. $t$ for PG 64-22 binder (a and b), PG 70-22 binder (b and c), and PG 70-22 mastic, 0.67 DR (e and f) for initial trials.....	68
Figure 12: Shear relaxation modulus (initial trials) .....	71
Figure 13: $/E^*$ / mastercurve from nanoindentation (initial trials).....	73
Figure 14: $/E^*$ / mastercurve from DSR (initial trials).....	73
Figure 15: $h_c$ vs. $t$ and $h_c(t)^2$ vs. $t$ for PG 64-22 (a and b), PG 70-22 (b and c), and PG 70-28 SBS (e and f).....	76
Figure 16: Creep compliance vs. maximum load (5000 $\mu\text{N}/\text{s}$ loading rate, 70 sec. hold time) for (a) PG 70-22 and (c) PG 70-28 SBS; (b) Creep compliance function vs. time for (a) to 100 sec. using fitted GPL parameters; (d) Creep compliance function vs. time for (c) to 100 sec. using fitted GPL parameters .....	78
Figure 17: Creep compliance vs. maximum load (5000 $\mu\text{N}/\text{s}$ loading rate, 70 sec. hold time) for (a) PG 70-22 mastic, 1.26 DR (lime) and (c) PG 70-28 SBS mastic, 1.29 DR (lime); (b) Creep compliance function vs. time for (a) to 100 sec. using fitted GPL parameters; (d) Creep compliance function vs. time for (c) to 100 sec. using fitted GPL parameters.....	79

Figure 18: Creep compliance vs. maximum load (5000 $\mu\text{N/s}$ loading rate, 70 sec. hold time) for (a) PG 70-22 mastic, 1.20 DR (granite) and (c) PG 70-28 SBS mastic, 1.20 DR (granite); (b) Creep compliance function vs. time for (a) to 100 sec. using fitted GPL parameters; (d) Creep compliance function vs. time for (c) to 100 sec. using fitted GPL parameters .....	80
Figure 19: Dynamic modulus comparisons between nanoindentation and DSR for (a) highest dust ratios of PG 70-22 and PG 70-28 SBS mastics and (b) PG 70-22 and PG 70-28 SBS binders.....	82
Figure 20: Nanoindentation results for dynamic modulus for PG 70-28 SBS, PG 70-22, and PG 64-22 mastics using lime and granite filler for (a) 0.6 DR; (b) 0.8 DR; and (c) 1.0 DR..	82
Figure 21: Shear relaxation modulus comparisons between nanoindentation and DSR for highest dust ratios of PG 70-22 and PG 70-28 SBS mastics and PG 70-22 and PG 70-28 SBS binders.....	83
Figure 22: Nanoindentation results for shear relaxation modulus for PG 70-28 SBS, PG 70-22, and PG 64-22 mastics using lime and granite filler for (a) 0.6 DR; (b) 0.8 DR; (c) 1.0 DR; and (d) 1.2 DR.....	84
Figure 23: (a) dynamic modulus vs. dust ratio at 0.08 Hz; (b) dynamic modulus vs. dust ratio at 0.08 Hz; (c) relaxation modulus vs. dust ratio at $t = 1$ sec.; (d) relaxation modulus vs. dust ratio at $t = 1$ sec. ....	85
Figure 24: Micrographs of common fillers used in asphalt concrete: (a) cement dust; (b) baghouse fine granite; (c) hydrated lime; and (d) fly ash .....	89
Figure 25: Representative cohesion-protocol nanoindentation curves .....	90
Figure 26: Parameters used in Equation (63) for a sample curve .....	91
Figure 27: Work of cohesion vs. penetration depth (lime) .....	94
Figure 28: Work of cohesion vs. penetration depth (granite) .....	95
Figure 29: Pull-off force vs. penetration depth (lime) .....	97
Figure 30: Pull-off force vs. penetration depth (granite) .....	97
Figure 31: Pull-off force vs. contact load (lime).....	98
Figure 32: Pull-off force vs. contact load (granite).....	99
Figure 33: (a) work of cohesion vs. dust ratio for mastics with lime; (b) work of cohesion vs. dust ratio for mastics with granite; (c) work of cohesion vs. filler volume fraction for mastics with lime; and (e) work of cohesion vs. filler volume fraction for mastics with granite.....	101
Figure 34: Example AFM image with labeled microstructures.....	103
Figure 35: Bees' proportion of phase image for binders and mastics.....	105
Figure 36: Average bee size for all materials tested in AFM .....	108

Figure 37: Average bee size vs. number of bees .....	109
Figure 38: Stiffening ratio $ G^* _{\text{mastic}} /  G^* _{\text{binder}}$ vs. filler volume fraction for (a) lime mastics and (b) granite mastics .....	112
Figure A.1: (a) PG 70-28 SBS, 1.29 DR lime (height); (b) PG 70-28 SBS, 1.29 DR lime (phase); (c) PG 70-28 SBS, 0.6 DR lime (height); (d) PG 70-28 SBS, 0.6 DR lime (phase); (e) PG 70-28 SBS, 1.2 DR granite (height); (f) PG 70-28 SBS, 1.2 DR granite (phase); (g) PG 70-28 SBS, 0.6 DR granite (height); (h) PG 70-28 SBS, 0.6 DR granite (phase) .....	133
Figure A.2: (a) PG 70-22, 1.26 DR lime (height); (b) PG 70-22, 1.26 DR lime (phase); (c) PG 70-22, 0.6 DR lime (height); (d) PG 70-22, 0.6 DR lime (phase); (e) PG 70-22, 1.2 DR granite (height); (f) PG 70-22, 1.2 DR granite (phase); (g) PG 70-22, 0.6 DR granite (height); (h) PG 70-22, 0.6 DR granite (phase) .....	134
Figure A.3: (a) PG 64-22, 1.2 DR lime (height); (b) PG 64-22, 1.2 DR lime (phase); (c) PG 64-22, 0.6 DR lime (height); (d) PG 64-22, 0.6 DR lime (phase); (e) PG 64-22, 1.2 DR granite (height); (f) PG 64-22, 1.2 DR granite (phase); (g) PG 64-22, 0.6 DR granite (height); (h) PG 64-22, 0.6 DR granite (phase) .....	135
Figure A.4: (a) PG 70-28 SBS (height); (b) PG 70-28 SBS (phase); (c) PG 70-22 (height); (d) PG 70-22 (phase); (e) PG 64-22 (height); (f) PG 64-22 (phase) .....	136

# CHAPTER 1. INTRODUCTION

## 1.1 Industrial Context and Problem Statement

Asphalt researchers have recently expressed interest in the micromechanical characterization of binder and mastic to understand complex mechanical behavior including cracking, healing, moisture susceptibility, adhesive bonding, and durability. Asphalt binder is a weakly polar material whose macroscopic mechanical properties and behavior have typically been modeled using empirical methods, such as the Christensen-Anderson-Marasteanu (CAM) model, that give little insight into the fundamental mechanical behavior of the material. Consequently, it is difficult to generalize these models to gain additional understanding from available data. The existing micromechanical models for asphalt concrete are very complex due to difficulty in determining constituent parameters based on binder, mastic, and aggregate physicochemical, particle interaction, and volume-filling reinforcements [8]. Hence, an overarching goal is to provide physically meaningful input values for multiscale modeling of asphalt concrete. Relevant micromechanical models include the Christensen and Lo model, based on the Generalized Self-Consistent Scheme, and the percolation model [65]. These models use shear modulus, Poisson's ratio, and volumetric concentrations of filler and matrix as inputs to predict fundamental material properties of a composite based on the properties of individual constituent components, with consideration for relative properties and geometric information for the various constituent phases. A multi-scale approach may end up ranging more than 12 orders of magnitude and relies on accurate structure-property relationships derived from careful material characterization and validated material models [49]. Efforts to develop better analytical models are challenged by various aspects of the multiscale nature of asphalt concrete, including small length scales, nonlinear material behavior, high heterogeneity at multiple length scales, high adhesion, and significant complexity in experimental methods to measure properties at smaller length scales.

The research objective of this study is to account for these challenges by developing and verifying nanoscale techniques through nanoindentation (NI) for creep and cohesion-protocol testing of viscoelastic materials, specifically asphalt binder and mastic. To meet this objective, this study will prove the feasibility of using the newest commercial nanoindentation equipment (CSM Instruments' UNHT Ultra-Nanoindentation Tester), adapted for soft materials, to quantify fundamental viscoelastic properties and work of cohesion of binders and mastics with an indenter tip. Viscoelasticity describes the time- and rate-dependencies of material behavior, which are significant factors for asphalt concrete. Work of cohesion is a primary factor controlling the strength and durability of pavements, including susceptibility to water damage. When unmaintained, asphalt exhibits problems such as high-temperature rutting from long-term plastic flow, low-temperature cracking, and intermediate temperature fatigue failure, all of which inflict serious damage on pavements that can be costly to repair.

Viscoelastic properties can be directly measured using a creep test, where material deformation occurs over time under a constant applied load. The response from this test can ultimately be transformed into dynamic shear and tensile moduli, more familiar quantities for researchers modeling asphalt behavior. The current study is undertaken to establish experimental techniques for the analysis of mechanical creep and cohesion behavior through load-controlled spherical indentation. Testing of binder and mastic through nanoindentation is the first step in what will hopefully be a long line of research on nanoindentation testing of asphalt concrete, and in particular reclaimed asphalt pavement (RAP). The primary benefits of nanoindentation stem from the ability to visualize phase distributions, deduce physical phenomena and expected behavior based on the spatial organizations of composite "ingredients", and provide meaningful inputs to micromechanical models for multiscale modeling. Nanoindentation is also a non-invasive technique, which takes on additional importance in viscoelastic materials where there is rate-sensitivity, time memory functions, and memory of loading histories. The ability to nondestructively measure small samples does not disrupt the complex microstructures in these types of heterogeneous materials and allows for preservation of short- and long-range interactions.

All the problems facing the asphalt community in optimizing asphalt pavement performance and maximizing lifespan cannot be solved on the application scale, where averaged, bulk properties are calculated. Multiscale modeling techniques are needed to predict input parameters for macroscale models based on an understanding of microscale, local behavior of a composite material. Asphalt is also heterogeneous on multiple length scales, so the microstructures of each scale are not representative of overall surface characteristics. Micro- and nanoscale experimental characterization supports these modeling efforts by providing a new perspective into the relevant mechanisms to be modeled along with additional insights into viscoelastic properties and cohesive energies for a variety of binders and mastic, both ex-situ and within asphalt concrete mixtures. To date, the micromechanical models of asphalt are insufficient due to difficulties in determining constitutive parameters based on aggregate, filler, and binder properties and interactions, using real, non-synthesized data.

Additional studies will be needed to determine whether and to what extent binder and mastic properties differ in-situ, within a mixture, when compared to the ex-situ results from this research. Interfacial interactions and phenomena take on even greater significance in asphalt composite mixtures, where there is concern of moisture susceptibility. Nanoindentation can address those concerns by determining weaker zones in the mixture that are more prone to adhesive and cohesive failure, which macroscale tests do not have the capability to investigate. While there is less emphasis on a composite response of bulk binder, whose constituent SARA components (saturates, aromatics, resins, and asphaltenes) cannot be “deconvoluted” due to length scale separability issues, methodologies for determining how old and new bulk binders are blended in RAP is a promising topic to pursue in the future, given the finite availability of virgin binder. Similar complications are reflected in polymer modified binders in efforts to optimize polymer compatibility and avoid streakiness, which would adversely affect mechanical properties and responses. Polymer modifier compatibility can only be visualized on the microscale. The hope is to use nanoindentation to improve our understanding of the fundamental properties of binder, mastic, and other highly compliant materials at the nanoscale.

## 1.2 Intellectual Merit

The analytic basis for this work advances the existing principles used in viscoelastic nanoindentation from past literature. No authors have translated or upscaled the micromechanical theories directly to the measures used by the asphalt community, such as shear relaxation and dynamic moduli. Binder and mastic modulus values are determined through nanoindentation data and principles for a first look at the micro-rheological origins of time-dependent behavior for binder and mastic. This research provides a first look at a nanoindentation-based approach to linear viscoelastic (LVE) modeling and analysis. The novelty of this work also lies in bringing forth certain theoretical models from nanoindentation with interconversions from linear viscoelasticity and combining these approaches into a coherent and unified method for response predictions on a representative volume element of non-RTFO and RTFO-aged binder and mastic. This has never been attempted in the nanoindentation community before. Interconversions from the theory of linear viscoelasticity are particularly useful since each unit response function uses a different input. Therefore, interconversions prevent having to change experimental setups, a potentially complicated task due to extensive re-optimization of testing conditions, to accommodate these different inputs. An appropriate testing methodology is crucial when one is faced with the possibility of performing an indentation on a sticky viscoelastic material with time-dependent properties. The results of the newly developed testing protocols, modeling schemes, and analyses also demonstrate the adaptability and flexibility of our techniques to a range of other compliant materials.

Within the dissertation, exploratory nanoindentation techniques for determining the viscoelastic and cohesive properties of asphalt binder and mastic, with mineral and manufactured fillers and varying filler volumetric concentrations, are developed, tested, and verified. New ways to calculate and interpret important viscoelastic and cohesive properties from nanoindentation data through low-load sphero-conical (blunt) nanoindentation are described. Testing of binder and mastic, in isolation, through nanoindentation is an important step toward in-situ testing of components in asphalt concrete, which cannot be

accomplished using conventional experimental methods. The results of this dissertation suggest the potential to expand nanoindentation testing to in-situ forensic investigations involving testing of preserved constituent components within distressed field cores.

The work of cohesion values over a range of filler volume concentrations, the observed percolation thresholds, and the discussion of filler reinforcement mechanisms in mastic are also significant contributions. To the author's knowledge, work of cohesion values of mastic have not yet been reported in literature.

While phenomenological results have their place, post-processing must also include a firm understanding of fundamental mechanical behavior for complex heterogeneous systems. This can only be achieved by starting from nanoindentation principles and upscaling.

### **1.3 Outline of Dissertation**

The structure of this dissertation consists of ten main chapters as follows:

Chapter 1: A general introduction is outlined regarding complexities in modeling the behavior of asphalt concrete. To emphasize the importance of this research, the problem statement and industrial context are defined, the intellectual merit is described, and the scientific benefits are clarified.

Chapter 2: The constituents of asphalt concrete are described, and the relevant literature on viscoelastic indentation, nanoindentation, and adhesion and cohesion experiments with atomic force microscopy (AFM) is reported.

Chapter 3: The nanoindentation approach is introduced, and an overview of models characterizing creep compliance and cohesion is reported.

Chapter 4: The materials and methods are described, including sample preparation techniques, the primary instrumentation used for conducting experiments, loading procedures, and experimental challenges.

Chapter 5: The analysis procedure for creep compliance is described by introducing the governing equation for creep, the model representing creep compliance, the numerical

modeling scheme, and formulations for interconversions from creep compliance to both shear relaxation modulus and dynamic modulus. The analysis procedure for cohesion is also introduced by describing the analytic formulation framing the basis for cohesion results.

Chapter 6: Results are presented for viscoelastic properties of both initial trials and RTFO-aged materials. The results of interconversions are presented and viscoelastic linearity is verified.

Chapter 7: Results are presented for work of cohesion of RTFO-aged materials, various trends in work of cohesion are evaluated, and binder work of cohesion values are compared to literature standards.

Chapter 8: Results of AFM imaging are presented. A length scale distinction is made between experiments with nanoindentation and AFM, and the implications of this distinction on probed volumes are discussed.

Chapter 9: Bulk binder and mastic viscoelasticity and cohesion results from nanoindentation are linked to microstructural changes resulting from filler and binder interaction identified by AFM. Possible reinforcement mechanisms are chronicled, and the influence of these factors on the degree of stiffening is speculated within the framework of combined observations from the results of linear viscoelastic properties, cohesion, and AFM.

Chapter 10: A summary of the main findings is provided, closing thoughts are offered, and future perspectives and research beyond the dissertation are suggested.

## **CHAPTER 2. LITERATURE REVIEW**

### **2.1 Asphalt Binder and Mastic Material Composition and Behavior**

Multi-scale modeling with asphalt concrete encompasses many issues, and these issues can be clarified by first understanding the exact composition of asphalt concrete at various scales. Asphalt binder is a black cementitious material in which the predominant constituents are bitumens that occur in nature or are obtained from petroleum processing and refinement. These materials are composed primarily of hydrocarbons but may contain oxygen, nitrogen, sulfur, and trace amounts of various metals. The chemistry of asphalt binder is highly complex, which has led to broad characterization based largely on functional groups defined according to solubility, namely saturates, aromatics, resins, and asphaltenes, in order of decreasing solubility. Asphaltenes are the precipitate of asphalt binder and are insoluble in n-heptane. Asphaltenes give asphalt binder its viscosity and are the most polar constituents of binder. Polar resins are the peptizing agents for asphaltenes. Aromatics are one of the dominant mediums through which the resins and asphaltenes are dispersed. They are light, oily, soluble, and mostly nonpolar. The non-polar, aliphatic, light, and oily saturates have the lowest viscosities, lowest glass transition temperature, and highest solubility. These individual components are not amenable to nanoindentation out of length scale considerations, as nanoindentation is probing bulk binder. In this context, asphalt binder can be treated as a homogenized material. A scale above binder is asphalt mastic, which is a combination of asphalt binder and filler particulate matter no greater than 0.075 mm in characteristic length. The filler particles are the portion of a combined aggregate blend passing the #200 sieve (0.075 mm sieve size). Due partly to the relatively high specific surface area of mineral fillers compared to other particulates in asphalt concrete, filler is considered to be non-inert and chemically interactive with asphalt binder. Microstructurally, all larger aggregates in asphalt concrete are coated with a thin layer of mastic [77]. The binder and mastic dominate viscoelastic and cohesive behavior of asphalt concrete and pose the most challenging constituent phases to characterize and model.

Fillers can be mineral fillers, derived from mineral aggregate, or manufactured fillers from waste or other industrial byproducts (e.g. fly ash, hydrated lime, bio-char, etc). Mineral fillers are produced by crushing large aggregate, so mineral filler and mineral aggregates have the same chemical compositions. The exact ratio of asphalt binder to aggregate particles is material-dependent.

For mastics, the Superpave specification for fillers is stipulated as a dust-to-binder proportion as:

$$DR = \frac{P_{0.075mm}}{P_{be}} \quad (1)$$

where  $P_{0.075mm}$  is the max percentage of particles passing the #200 sieve by the total mass of mix, and  $P_{be}$  is the mass percentage of effective binder content by the total mass of mix. The dust-to-binder proportion is the mass ratio of filler to binder and is colloquially known as the dust ratio, which is abbreviated “DR” in all tables and figures of this report.

Hydrated lime filler is often added to asphalt concrete to improve moisture susceptibility of pavements. Review articles related to hydrated lime particle interactions have been compiled by Lesueur et al. [39] and Little and Petersen [41]. Both reviews suggest that hydrated lime improves performance-related properties such as fracture resistance within an asphalt concrete mixture compared to a conventional mixture with normal mineral filler. Hydrated lime, of relatively low molecular weight, modifies the surface properties of the aggregate, allowing for the development of surface composition and roughness more favorable to binder adhesion. Lime is also highly reactive chemically with the binder acids, slowing down the oxidative age hardening kinetics by irreversibly adsorbing reactive components from the binder onto its surface. The higher porosity of lime leads to high fractional voids, giving rise to significant stiffening in mastics above room temperature [39]. Lastly, lime increases binder’s ability to heal during repeated cyclic loading, thus increasing its resistance to fatigue damage.

At another scale above mastic, fine aggregate particles larger than filler particles but smaller than 1-2 mm (coarse aggregate particles) are combined with mastic to form a Fine

Aggregate Matrix / Mortar (FAM). More specifically, FAM includes binder, air, filler, and fine aggregate particles with a specific gradation. Air voids introduced into the mix are typically observed at the scale of FAM. A complication in asphalt research is determining the cutoff between fine and coarse aggregate. The cutoff is mixture dependent but often happens at the 2.36 mm (#8) sieve or smaller sizes [77]. More specifically, the Bailey method can be used for gradation selection and for the separation of coarse and fine aggregations. The functionally relevant FAM for a given mixture is called the Real FAM [77].

The asphalt concrete mixture is the largest scale and the most heterogeneous system. It is a combination of the FAM and graded coarse aggregates up to 1.5 inches [77]. The Dominant Aggregate Size Range (DASR) will form the range of particle sizes that generates the dominant structural network of aggregates. These scales are represented graphically in Figure 1.

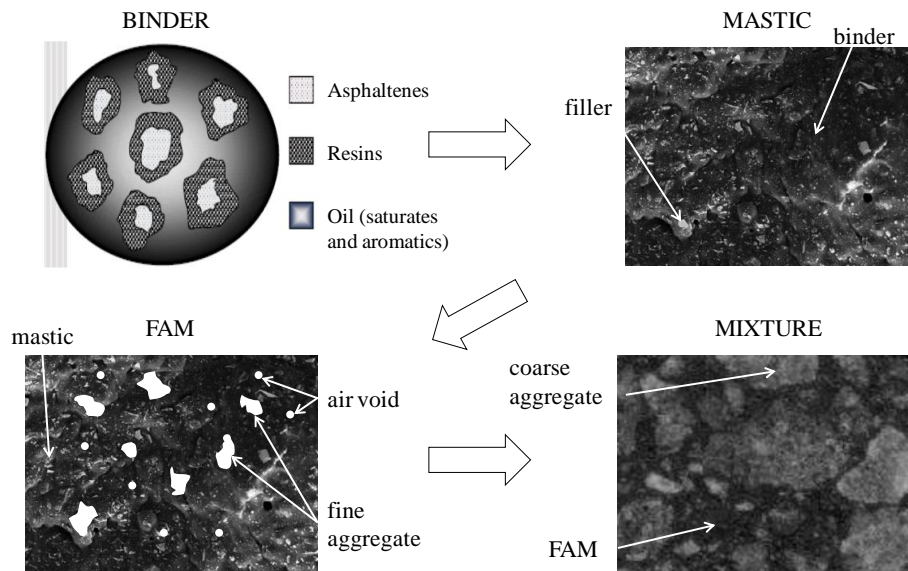


Figure 1: Multi-scale representation of the constituents of asphalt concrete

Although asphalt concrete is a bulk heterogeneous viscoelastic material, binder and mastic are the two phases governing viscoelastic behavior, as thermorheologically simple materials. As the weakest phases in asphalt concrete that are most prone to damage, they are the focus of this research to characterize viscoelastic behavior. These two phases have some of the most significant influences on stress versus strain-rate behavior of asphalt concrete.

## **2.2 Viscoelastic Indentation and Nanoindentation on Asphalt**

The challenges facing nanoindentation of asphalt concrete and its constituents can be better understood within the context of existing literature and, more specifically, its limitations. The current literature on nanoindentation of asphalt concrete and its constituents has a predominant focus on the hardness and elastic response of binder derived from the Oliver-Pharr (OP) method [51].

Some approaches for viscoelastic indentation have striven to remove the time-dependent effects altogether [71], [72], [74], but these approaches do not emphasize direct measurement of viscoelasticity. Tarfeder et al. [71] developed a range of nanoindentation-derived elastic modulus and hardness values of aged asphalt. Tarefder and Faisal [72] studied the effects of creep hold time and loading rate on the mechanical properties of aged asphalt binder through nanoindentation testing. They determined loading rates and hold times for binder that produced nanoindentation data which they analyzed with the Oliver-Pharr method to obtain elastic modulus and hardness. Tarefder and Faisal [74] also used nanoindentation to study aging behavior of mastic and aggregate. Tarefder's approach, however, has not yet been feasible with softer, unaged materials. Moreover, the analysis approaches based on the Oliver-Pharr method explicitly neglect the time-dependency that is a hallmark of viscoelastic behavior and is so critical for asphalt concrete characterization in engineering practice.

Viscoelastic behavior affects the nanoindentation response such that Young's modulus calculated from the Oliver-Pharr method can become unreasonable [56]. To analyze viscoelastic responses in nanoindentation tests, Oyen used the elastic-viscoelastic

correspondence principle to generate spherical indenter solutions for a number of indentation testing protocols, including creep following a constant loading rate and a multiple ramp-and-hold protocol, to measure the creep response at several loads (and depths) within the same test [56]. Based on the elastic solution of the indentation problem, Jäger et al. [26] determined the corresponding viscoelastic solution by the application of the method of functional equations. This general solution, which accounts for the real geometric properties of the indenter tip, is specialized for the case of a trapezoidal load history. Jäger et al. [26] were one of the first groups to use the nanoindentation grid technique to demonstrate a distribution of mechanical properties on the surface of asphalt binders. They also provided the first study of thermal effects on the mechanical properties of binder using nanoindentation. Qiang et al. [62] proposed a two-step viscoelastic spherical indentation method to account for material relaxation. The proposed model takes into account the sample thickness, which is important for applications in which the thickness is less than ten times the indenter radius. Tarefder and Faisal [73] proposed a very simple spring-dashpot-rigid element model for characterizing viscous effects, but this approach has not been validated. Veytskin et al. developed loading programs and analyses to account for both linear viscoelastic [80] and cohesive [81] behavior, which were then validated by comparisons to macroscale results. The cohesion results indicate a unique plateau in work of cohesion for each filler-binder combination beyond which additional filler does not have an appreciable influence on work of cohesion. To the authors' knowledge, this is the first determination of work of cohesion for mastics.

Large scale instrumented indentation experiments were first considered for obtaining viscoelastic properties on asphalt materials. Anderson et al. [4] considered macroscopic spherical indentation tests on asphalt binders, using displacement controlled tests and linear viscoelastic analysis for small penetration depths. Ossa et al. [53] and Ossa & Collop [52] used a power law creeping solid model with a macroscopic indenter at 0 °C to characterize asphalt binder and mixtures with aggregate less than 10 mm in characteristic size. Researchers using flat punches with 100 to 450 μm diameters tested LVE properties of asphalt binders at temperatures below 0 °C [45], [87]. At smaller scales, Allen et al. used

AFM to perform indentation experiments to characterize viscoelastic behavior of individual phases within binder, but their validation suggests that this approach gives values much smaller than expected from macroscopic tests [1], [2]. Inherent limitations in using AFM as a tool to measure quantitative mechanical properties may be responsible for this observation.

Overall, the literature for nanoindentation of asphalt concrete is still in the stages of infancy, with literature only recently emerging on the viscoelastic responses of asphalt binder through microscale techniques. No research has focused on deriving fundamental responses of binder and mastic through viscoelastic and cohesion testing in nanoindentation and extending these results to a discussion of filler reinforcement mechanisms. To the authors' knowledge, this study is the first to link bulk binder and mastics viscoelasticity and cohesion results from nanoindentation to microstructural changes resulting from filler and binder interaction identified by AFM.

### **2.3 Atomic Force Microscopy for Adhesion and Cohesion Properties**

Past research on work of adhesion, cohesion, and surface energy at the microscale has focused on AFM experiments. A variety of attempts have been made to characterize interaction and interfacial properties of binder (but not mastic) through AFM test procedures. Little and Bhasin [40] and Pauli et al. [59] characterized adhesion in terms of the work required to detach a 5  $\mu\text{m}$  cantilever-mounted glass bead from an asphalt thin-film surface after the application of various levels of rate-dependent external loading. Little and Bhasin [40] reported Lifshitz-van der Waals (LW) components of binder surface energy values ranging from 0.04 to 0.05  $\text{J}/\text{m}^2$ , compared to their reported values of 0.0136 to 0.045  $\text{J}/\text{m}^2$  obtained using both the Wilhelmy plate and sessile drop methods on companion samples. With their method, the work of adhesion is determined using the cantilever spring constant, the vertical distance of retraction during pull-off, and the radius of the glass bead. This technique allows for subsequent calculation of surface energy. Pauli et al. [59] reported binder surface energy values ranging from 0.03 to 0.06  $\text{J}/\text{m}^2$ . With the AFM methods, there is still ambiguity as to precisely whether adhesion or cohesion is being measured as the

failure type, because during the pull-off test failure can either occur at the interface between the tip and binder or within the binder.

With a stock, non-functionalized AFM probe tip, only the nonpolar, dispersive Lifshitz-van der Waals (LW) component of surface energy can be calculated [40]. Further research is required to be able to derive all three surface energy components using the methodology of active polar mono-layer modification. Experiments have shown that the LW component of asphalt is the most significant contributor to the surface energy of asphalt binder [40]. Al-Rawashdeh [3] used AFM to investigate the effects of water on the adhesive and cohesive forces in three asphalt binders (one hot mix asphalt and two warm mix asphalts). Four different cantilever tip material coatings were used to measure the cohesive forces within asphalt binder through a carboxylic acid ( $-\text{COOH}$ ) functional group probe coating, along with the adhesive forces between binder and aggregate through a  $\text{CaCO}_3$  coating (representing Calcite in limestone) and between binder and sand through a  $\text{SiO}_2$  probe coating (representing sandstone). The LW surface energy component for wet and dry conditions was calculated in all cases. Al-Rawashdeh's study demonstrated that AFM is a useful advanced characterization tool to evaluate the strength of bonding between three types of asphalt binder on four types of functionalized surfaces in the presence and absence of water.

Research conducted by De Moraes et al. [14] and Pauli et al. [58] investigated the morphology of asphalt binders using AFM. They focused on studying the potential interactions between crystallizing paraffin waxes and the remaining asphalt components for thermally conditioned samples. Crystallized paraffin waxes form the largest microstructure within asphalt binder's microstructure, commonly referred to as the "bee" structure. Typical bee sizes range from 2 – 8  $\mu\text{m}$ , but can be significantly larger [58]. Not all binder microstructures, however, exhibit bee structures. De Moraes et al. [14] and Pauli et al. [58] demonstrated that the bee structure changes as a function of temperature. Pauli et al. [58] hypothesized that the interaction between crystallizing paraffin waxes and the remaining asphalt components is responsible for much of the morphological structuring of asphalt binder, including the bee structures.

Pauli et al. [60] also recently developed an “adherence energy” test for force-displacement AFM curves on binder through pull-off tests with glass beads, based on fracture energy and crack propagation methods. Their technique involves creating and fracturing a standardized adhesive contact between asphalt and glass by application of a direct tensile force to the contact at various rates. It has been found that the rupture during pull-off always occurs within the thin film of binder that acts as the glue between the probe and substrate. The asphalt cohesive strength is the weak link during the unloading phase, and asphalt-glass bond strengths are much higher than binder cohesive bond strengths. Hence, although the test is called an “adhesive test,” the method is determining bonds that are cohesive and dispersive in nature, and thus a property of the binder. Pauli et al.’s deflections are averaged over all rate and temperature data to calculate equilibrium work of adhesion, rather than calculating rate-dependent works of adhesion. Pauli et al.’s method also evaluates “work-to-break” contacts by numerically integrating a rate-dependent set of force curves, which is not the analysis method chosen for this research. Pauli et al. reported their equilibrium work of adhesion for SHRP binder AAD-1 at 2.0 °C and at a specific rupture rate to be 0.054 J/m<sup>2</sup> [60]. In Pauli et al.’s research, the rate-dependence on stage velocities may also be a limitation that precludes a true determination of an intrinsic material property such as surface energy. Lastly, Tan and Guo (2014) used AFM to describe the surface morphology and surface adhesion force of asphalt mastic. Fourier transform infrared spectroscopy was used to analyze the physicochemical interaction between binder and filler.

Although the determination of surface tension components requires contact angle measurements between test solvents of known surface tension components and an unknown solid surface (e.g. a Sessile drop test using a goniometer to measure static contact angles of probe liquids with various substrates), this applies in determining the surface tension components for asphalt binder. Together, the dispersive and non-dispersive components of surface tension (i.e. the LW and Lewis acid-base components, respectively) comprise the interfacial surface free energy.

There has also been work on the modes of fracture associated with cohesive failure using a variety of beam geometries. Authors such as Xu and Needleman [83] have run

numerical simulations of fast crack growth in viscoelastic solids across a specific set of cohesive surfaces, and Song et al. [70] have investigated fracture behavior in asphalt concrete by using a bilinear cohesive zone model and the single-edge notched beam test to permit more degrees of freedom for mixed-mode crack propagation. In the former case, the focus is on fast crack growth in brittle solids, including crack branching, there is an elastic characterization of the cohesive surfaces, and time-dependency of the separation process is neglected. In the latter case, bulk asphalt concrete, rather than its dominant viscoelastic constituent components, is investigated, which alludes to fast crack nucleation and propagation. Also, Ji et al. investigated the effects of various typical adhesive thicknesses on global and local interfacial fracture of bonded joints, where the adherents are assumed to be linearly elastic during the fracture process [27], [28].

Adhesive pull-off forces and force map images obtained from AFM with sharp tips have also been reported in the literature [18], [43], [85], but these forces have not been extended to discussions of adhesive or cohesive energy. In Lyne et al. [43], there are differences in adhesion results within the samples that are unaccounted for. Yu et al. [85] discuss the relative trends of adhesion force under different operational parameters. The differences in trends are attributed to differences in tip radius and tip geometry, neither of which is reported. Yu et al. [85] mention that many AFM operational parameters (surface roughness, tip radius, force, and scanner speed) can significantly influence experimental results, but these effects have not been explicitly addressed in literature.

The need to develop consensus measurement techniques for characterization of viscoelastic and cohesive behavior on a representative volume element of binder and mastic can be fulfilled with the newly developed creep- and cohesion-protocol testing methods described in this research.

## CHAPTER 3. NANOINDENTATION APPROACH

### 3.1 Nanoindentation Overview

When investigating materials that have a viscoelastic nature and are prone to damage, the surface of a material is the most important part determining its compatibility with the environment. For several decades, nanoindentation has been used for the determination of material properties such as elastic modulus and hardness. The primary reason for the popularity of these measurements was that with a spherical indenter and sufficiently low loads, essentially elastic deformations could be obtained. The contact problem could be solved relatively simply by solving the well-known Hertzian equations, which assume no surface forces acting at a contact interface [30], and the elastic constants of the material can be easily calculated.

This process does not work well for the determination of time-dependent viscoelastic properties, and, although we use stiff materials as calibration standards, there has recently been a significant rally to investigate viscoelastic and polymeric materials. In theory, low deformations would lead to the suppression of irreversible plastic flow of a material, and the LVE properties of the polymer can then be determined [29]. For nanoindentation, LVE can be interpreted as the regime of small microstrains whereby creep compliance is independent of the applied load. Load-dependence of the creep compliance function will indicate material nonlinearity [87]. In practice, materials can still experience the effects of nonlinear viscoelasticity and viscoplasticity, which can manifest themselves in similar ways in tests and can be difficult to discern. These concepts often get confused, especially because deformation that looks plastic compared to the initial viscoelastic time constants from a Prony series can still sometimes fully heal [54]. The geometric nonlinearity of asphalt gives rise to a power-law load-penetration depth response. The challenges of viscoelastic indentation result from three factors: the fundamental equation relating indentation force and

depth is derived for infinitesimal deformation, its counterpart for large deformation has no explicit analytical expression, and the strain state under the tip is non-uniform [55].

One solution to avoid nonlinear effects is to use a spherical indenter tip, since with a Berkovich indenter, the limits of plastic flow are immediately reached and the deformation quickly becomes irreversible. With a spherical tip, the creep stress amplitudes are the lowest, the contact depths are minimized, and the viscoelastic deformations have a greater tendency to fully heal after the unloading cycle has been completed. The larger the tip radius, the longer a test will be maintained within the LVE limit.

Commercial nanoindenters ship with Oliver-Pharr (OP) analysis for determining modulus and hardness distributions and frequencies across all phases, but this type of analysis is irrelevant for viscoelastic materials due to a continuing time- and rate-dependent deformation during unloading that precludes a prediction of elastic recovery from an elastic contact mechanics model. Many existing asphalt nanoindentation studies mistakenly use OP analysis even though it is clear that viscoelastic material constitutive behavior is inconsistent with the Hertzian assumptions for which the OP method is used [71], [73], [74]. The primary assumptions of the Hertzian theory are that the surfaces are continuous, non-conforming, and frictionless, the strains are small, and each solid can be considered as an elastic half-space. The use of the OP method for extracting material property measurements from viscoelastic materials and can lead to significant errors since this extraction is done from an unloading curve that assumes a purely elastic recovery.

## **3.2 Creep Compliance and Nanoindentation**

A primary hindrance of using the OP method is the need for a long hold time to truly characterize the viscoelastic nature of binder and mastic. The purpose of a hold time in creep testing is to allow the material to “creep out”, i.e. to deform sufficiently during the hold time for creep deformation to be insignificant during unloading. For viscoelastic nanoindentation, two significant issues arise in the study of experimental data: the fitting of data with an appropriate function, and the conversion of that function to other related material functions.

The data in question is typically obtained by time-domain testing (e.g. creep and relaxation tests) or frequency-domain testing (e.g. dynamic mechanical tests), though nearly all nanoindentation methods focus on time-domain testing for practicality.

For fitting time-domain experimental data, some numerical techniques have been successfully implemented, most notably the collocation method and multidata method of approximate Laplace transform inversion [11]. For fitting frequency-domain data, some researchers have improved upon least squares approaches with alternative methods. These have included Tikhonov regularization techniques and linear regression with additional constraints [86].

Once a material function is obtained, it is useful to find its counterpart function. Unlike linear elasticity, in which functions are related algebraically, the relationships between material functions in linear viscoelasticity are time-dependent involving either integral or differential equations. There are numerous techniques that can be used to perform interconversions, including convolution integral equations, Fourier transformations, and Laplace transformations. Each technique has an associated method of solution. The difficulty of the interconversion lies in first extracting the unknown creep compliance from the convolution integral. Some papers use Bradshaw's method, which solves the integral in the time domain and gives a solution for interconverting the coefficients [7]. This is a sign control method that uses a least squares approach with an additional constraint forcing the model coefficients to remain positive, which is important for Prony series models. This results in an iterative solution, accomplished via the Levenberg-Marquardt method, to quickly locate coefficients that minimize the error between the data and function. Some quadrature-type methods involving recursive relationships have been proposed for interconversion. It was demonstrated that, for some of the higher order quadrature-type methods, stability and convergence problems arise during the conversion from compliance to modulus [17]. There are additional interconversion relationships that can be applied through convolution integrals to determine the time-dependent bulk modulus of an LVE material from its tensile and shear relaxation modulus, along with a representative elastic modulus [48], [78].

The identification of viscoelastic properties from nanoindentation test data, taking the real tip geometry into account, is one of the primary goals of viscoelastic nanoindentation on any rheological material. Based on the elastic Hertzian solution of the indentation problem, the corresponding viscoelastic stress and strain distributions can be obtained through Laplace transforms of the associated viscoelastic integral operators [36]. A variety of different mechanical analog (spring and dashpot) models can be considered to simulate viscoelastic behavior, including deviatoric creep, single dashpot, Maxwell, Voigt, standard linear solid, Kelvin, Weichert, Burger's, fractional rheological models, and Prony series (summed exponential function) models that are a linear summation of a combination of the previous components [54]. Non-mechanical analogs include the pure power law (PPL), generalized power law (GPL), modified power law (MPL), and sigmoidal functions and are typically used less commonly than Prony series models, now that a Prony series can be expanded to many terms and fitting software minimizes computational time. For instance, a carefully selected a priori generalized expression allows us to determine viscoelastic model parameters from a measured load-penetration history.

In asphalt research, the elastic modulus is mostly irrelevant, acting predominantly as an instantaneous modulus and corresponding only to a single frequency and temperature [56]. Since in elastic problems, the stress-strain relationship is independent of applied loading conditions, the general solution of the contact problem for isotropic elasticity includes a pair of time-independent constants such as elastic modulus and Poisson's ratio [54]. The elastic-viscoelastic correspondence principle can be used within the context of depth-sensing indentation testing to solve the analytic contact mechanics problem in a viscoelastic half-space by substituting viscoelastic integral and differential operators, from the viscoelastic stress-strain relations, for the elastic Hertzian constants [36]. This method was formulated by Lee and Radok to determine an expression for the time-dependent indentation depth under a prescribed arbitrary indentation loading history in an LVE material [36]. This method is not restricted to fixed boundary conditions and remains valid as long as the contact area increases monotonically with time. The restriction of increasing contact area was fully removed by Ting, however this solution is challenging to employ in the analysis

due to its implicit formulation [75]. The elastic indentation problem is thus extended to LVE by replacing the elastic constants in the solution of the equivalent elastic boundary value problem by the Laplace transforms of the associated viscoelastic operators.

The Boltzmann hereditary integral operator can also be used to find the stresses and deformations based on the corresponding solution for a linear elastic material, and it provides the capability to solve the viscoelastic problem for moving boundary value problems [36]. For the solution of the elastic indentation problem, the Sneddon solution is employed. The Sneddon solution is advantageous because it generalizes the problem for any axisymmetric indenter, uniting multiple solutions for different indenter geometries into one formulation [69].

The rigid indentations onto a half-space composed of an LVE material can be assumed to be a quasi-static boundary value problem as an approximation of the LVE convolution integral [31]. In this approach, creep compliance can be calculated from the following relation:

$$D(t) = \frac{\varepsilon(t)}{\sigma(t)} \quad (2)$$

Time-dependence is described by empirical viscoelastic approaches and is typically characterized by the assignment of an empirical Prony series to describe a material's constitutive response. For example,

$$J(t) = C_0 + \sum C_k e^{-t/\tau_k} \quad (3)$$

for creep  $J(t)$  in load controlled tests, and

$$G(t) = D_0 + \sum D_k e^{-t/\tau_k} \quad (4)$$

for shear relaxation  $G(t)$  in displacement controlled tests, where  $\tau_k$  is a time constant,  $D_k$  and  $C_k$  are single-component parameters, and  $C_0$  and  $D_0$  are regression coefficients. Reported

parameters in literature have included instantaneous and equilibrium modulus values [46], [56]. The shift factor in time-temperature superposition, for thermorheologically simple materials such as asphalt binder and mastic, is most commonly described by either the Williams-Landel-Ferry (WLF) equation or the Arrhenius formula [61]. Tarefder et al. determined that, in the transient stages of an NI test, the creep behavior of asphalt binder is influenced by the loading rate used during the test, with creep increasing as the loading rate increases. However, the creep rate eventually reaches an asymptotic value regardless of the loading rate [72].

A linear viscoelastic analysis relies on the deformation being restricted to elastic and viscous components (no plasticity or nonlinear viscoelasticity). Experimentally, a blunt spherical tip would be the most appropriate tip geometry to avoid plasticity and accompanying overestimations of stiffness. However, one way to accommodate plastic deformation if the indenter tip is too sharp is through viscous-elastic-plastic (VEP) models [50]. If a more complicated constitutive response, such as nonlinear viscoelasticity, is unavoidable, there may be no closed-form analytic expression for the indentation problem, especially if the deformations are large. In such cases, numerical approaches such as finite element analysis may be required.

### **3.3 Cohesion and Nanoindentation**

The formulations and principles in Section 3.2 only apply when the contact area is continuously increasing. Since one of the objectives is to characterize a full viscoelastic response, the entire loading cycle must be considered. As a result, cohesion analysis requires an alternative method to that of Lee and Radok.

A new theoretical nanoindentation approach is needed for cohesion analysis because Lee and Radok's approach is based on monotonically increasing contact areas. If the radius of contact increases to a maximum and then decreases to zero, the normal deflection of the entire surface reduces to zero, which is contrary to what would be expected for a viscoelastic material in which the delayed elastic and viscous components of strain would be expected to

leave a residual indentation just after contact has ended [35], [36]. Such materials can be looked upon as having hereditary properties, and one would expect a residual deformation to be left as a memory of the contact process. The reason for this paradoxical result is that if the radius of contact passes through a maximum and begins decreasing, a residual tensile surface traction is left in the viscoelastic case at points formerly in the contact region, which violates the contact condition that outside the current region of contact, the surface traction should be zero. This difficulty does not arise with a non-decreasing contact radius since the zero initial conditions, including zero initial pressure distribution for the earliest times, guarantees zero traction outside the region of contact. Thus, although the solution correctly describes a viscoelastic stress and deflection combination, for a decreasing contact radius this solution would require an applied surface traction outside the region of contact, and this is not the solution which represents the actual contact situation [35], [36].

The cohesion testing program is essentially a direct tension pull-off test, as the contact area between indenter tip and sample continues to monotonically decrease. Cohesion in nanoindentation is very poorly represented in literature, with few relevant articles. In traditional surface energy tests such as the Sessile drop test, contact angles are commonly measured with a goniometer, and the three surface free energy components are calculated [21]. It was proposed to measure contact angles for several liquids and to use the Young-Dupre and Dupre equations [21]. In nanoindentation, an entirely new approach must be taken since the experimental setup does not accommodate liquids or similar types of contact angles.

Intrinsically, when two dissimilar materials form an interface by being in contact with one another, a tensile force can be artificially applied to split the materials into two separate parts [40]. The work of adhesion is defined as the energy per unit surface area expended to split two dissimilar bodies that are in intimate contact with this artificial tensile force. The adhesive force is measured as the external pulling force required to detach the indenter from the sample at their interface in a vacuum. The value of the adhesive force will depend on the indenter geometry and loading parameters [40].

Atomic force microscopy (AFM) and nanoindentation are only able to calculate the nonpolar Lifshitz-van der Waals (LW) component of surface energy [40]. The unique modes of measurement with nanoindentation and AFM preclude a direct comparison with more traditional “gold standard” methods of surface energy measurements. Without a functionalized coating of the tip with active monolayers of polar materials, the Lewis acid and Lewis base components cannot be determined. However, experiments have shown that the LW component of asphalt is the most significant contributor to the surface energy of asphalt binder, which is a low-energy material [40]. Literature results from the Sessile drop method, Wilhelmy plate method, and inverse gas chromatography indicate that the LW component of asphalt binder varies from 14 to 50 ergs/cm<sup>2</sup>. The acid and base components from these test methods vary from 0 to 3.9 ergs/cm<sup>2</sup> [40].

Little et al. characterized adhesion in terms of the work required to detach a 5 μm glass bead cantilever tip from an asphalt thin-film surface after the application of various levels of rate-dependent external loading [40]. The work of adhesion is determined using the cantilever spring constant, the vertical distance of retraction during pull-off, and the radius of the cantilever tip. The LW surface energy component  $\gamma$  is determined from contact mechanics principles as:

$$\gamma = \frac{1}{2}W_{adhesion} \quad (5)$$

and the best-fit curve for the surface energy versus contact load graph is extrapolated to zero to determine the equilibrium thermodynamic surface energy [40], [59]. The fracture energy release rate is equivalent to the work of adhesion determined at the point of interface separation, or cracking [47]. Thus, the work of adhesion is twice the surface energy determined for a given material, as represented in Equation (5). A caveat is that the expression above and its associated derivations are based on the assumption of a bond failure occurring entirely within the thin asphalt film that was tested. In that sense, it is representing cohesive rather than adhesive failure. In [59], reported adhesion energies are purely cohesive in nature and are a property of the binder. Since asphalt-aggregate, asphalt-glass, and

asphalt-diamond bond strengths are higher than asphalt cohesive and dispersive bonding [40], the asphalt cohesive strength is the weak link and of most importance to Pauli et al. in [59].

Viscoelasticity will have significant impacts on contact area. The Johnson-Kandall-Roberts (JKR) or Derjagin-Muller-Toropov (DMT) contact adhesion models are considered to effectively interpret the actual work of adhesion [25], [32]. The JKR model, for example, corresponds to contact between compliant surfaces where weak adhesive forces and a high radius of curvature exist [47], [66].

Adhesion testing in nanoindentation can be used to determine binder-indenter work of adhesion, where the contact area is continuously decreasing. One theoretical indentation model has been proposed by Sirghi et al. [68], for which it was determined that for conical indentation:

$$F_a = -\frac{\gamma 8 \tan \alpha}{\pi \cos \alpha} (h - h_f) \quad (6)$$

where  $\gamma$  is the work of adhesion,  $F_a$  is the maximum tensile pull-of force,  $\alpha$  is the cone angle of the indenter,  $h$  is the indenter displacement,  $h_f$  is the residual displacement, and the adhesive force is the derivative of adhesion energy. Adhesive contact models for work of adhesion are provided by both the JKR and DMT models. These models can be applied to mechanical contacts of soft spherical bodies that interact by short-range adhesive forces, for a contact radius that is much smaller than the indenter tip radius. The theoretical model proposed by Sirghi et al. applies for a larger contact radius and provides a more realistic interpretation of force-displacement curves for adhesive materials [68]. Fitting force-displacement curves from NI with the force-displacement dependence predicted by the theoretical model would indicate the model efficacy as it relates to work of adhesion predictions. The entire formulation, originally developed for adhesion, applies to cohesion testing when the tip is coated with a thin layer of the sample after a nanoindentation test.

The model by Sirghi et al. starts by considering the elastic deformation of a sample half-space by a rigid axisymmetric indenter through Sneddon's solution [67], [68], [69].

There are numerous assumptions in the model formulation of Equation (6). Sneddon's solution for the deformation of the sample surface outside the contact area is not considered to be affected by adhesion. Currently, there are no published works on how adhesion affects solutions of pressure distributions and deformations outside of the contact area region. Both the tip and sample surfaces are assumed to have high smoothness. The adhesion energy and contact area are considered to be continuously varying during the indentation. Any realistic model could take into account discontinuous functions for the contact area, although physically and practically, discontinuous forces are unrealistic. This is more applicable for complex indenter geometries such as a cone with a flat tip, or for the moment of jumping into contact when adhesion forces quickly act to increase the contact area due to van der Waals intermolecular dispersive forces. Although the adhesive force affects both the loading and unloading parts of the indentation process, only the unloading segment allows for a direct measurement of the adhesive force due to the required condition of a decreasing contact area. The reason for this requirement is explained in [35] and brought forth in Section 3.2 by considering traction boundary conditions.

Pauli et al.'s recently developed "adhesion" energy test for force-displacement AFM is based on fracture energy and crack propagation methods [60]. Although the testing protocol is named an adhesion test, it is measuring the cohesive strength of binder through dispersive interactions. The group reported on the development of a test procedure to investigate adhesion energy of asphalt thin-films using a glass micro-bead colloidal tip cantilever as the test probe. The study quantified surface energy properties of asphalt binder as they relate to fatigue, self-healing, and moisture intrusion. Adhesion energy is defined in terms of a reversible or equilibrium work of adhesion and energy loss due to dissipative processes, including plastic flow. The group's technique involves creating and fracturing a standardized adhesive contact between asphalt and glass by application of a direct tensile force to the contact, at various rates. The work required to fracture the standard contact is measured and recorded as a function of temperature and separation rate. The results of this study show that asphalt fracture energy is rate-dependent [60].

To include rate and temperature dependence, the defined adhesion energy includes a viscoelastic loss function for the dissipative processes, which is written for a characteristic crack speed and a rate-temperature dependent shift factor. The experiments involve forming a specific adhesive contact between an AFM tip and a glass substrate surface using a thin-filmed asphalt binder sample as the ‘glue’ and subsequently measuring the work required to rupture this contact as a function of temperature and separation rate.

Theoretically, the total potential energy involved in a contact-rupture AFM cantilever–substrate system may be expressed as the sum of potentials [60]. Each energy potential is defined in terms of a force acting over a specific displacement related to the cantilever-substrate system. The sum of three distances (based on the cantilever, sample, and cantilever-substrate interface) defines the total displacement of the cantilever-piezo scanner system. “Action-at-a-distance” attraction / repulsion forces exist during approach between the cantilever tip and substrate surface. The total potential energy for the contact-rupture system is defined as [60]

$$U_{tot} = \int (F_c + F_s) dZ \quad (7)$$

where  $F_c$  is the Hookian force exerted on or by the cantilever and  $F_s$  is the Hookian force describing the sample’s tensile deformation. “Work to break contact” versus reduced rate (i.e. stage velocity or critical crack speed) data is then fit to an energy dissipation function. The potential energy associated with the “work to break contact” for the contact-rupture system is evaluated by numerically integrating a rate-dependent set of force-displacement curves through a trapezoidal integration technique over the distance of the adhesive contact (assumed as the vertical distance of unloading), and these values are then plotted for a given temperature as a function of reduced rate. Adhesion energies are reported in a plot as a function of reduced rate, and equilibrium thermodynamic work of adhesion values are calculated from the pull-off force. The adhesion energies determined at a give temperature are derived as functions of rupture rate. The authors determine that adhesion energy increases with increasing temperature. It is assumed that with increasing temperature, the

asphalt should exhibit more plastic flow and hence stretch more prior to rupture of the adhesive contact [60].

Adhesion energy is defined by Pauli et al. as the equilibrium work of adhesion including energy lost due to dissipative processes. Sirghi et al. defined contact adhesion energy without dissipative or plastic contributions, and it is based on the cone angle of the indenter, the pull-off force, and the penetration depth.

For the thin films of asphalt that are used by Pauli et al., the thin-film criteria used in nanoindentation, that penetration depth should be no more than 10% of the sample thickness [6], is suspect. There is also some ambiguity as to the physical difference between “work to break contact”, a measure of the potential energy associated with integrating the force-displacement curves, and “equilibrium work of adhesion”. The authors claimed to have determined surface energy properties of asphalt binder as they relate to fatigue and self-healing, but there are no direct extensions provided to fatigue and self-healing mechanisms. In the Sessile drop or Wilhelmy plate methods, the two standardized procedures in macroscale testing to determine equilibrium surface energy of binders, there is no rate associated with surface energy because there is no tip approach or separation rate. The Wilhelmy plate method is used to measure the contact angles of various probe liquids with asphalt binders. The contact angle is measured indirectly by immersing a plate coated with binder into the probe liquid and deriving the angle from the measured force. The Sessile drop method is used to measure static contact angles of probe liquids with any solid surface but is best suited for low-energy surfaces such as asphalt binders. Contact angles are measured directly by dispensing a drop of the probe liquid on the solid surface and capturing an image of the drop. The captured image can be analyzed using image processing software to obtain the contact angle of the liquid at the edge of the drop. The contact angles measured by the Sessile drop method (a static method) are slightly different from the contact angles measured by the Wilhelmy plate method (a quasi-static method). However, the analytical tools to interpret the contact angles and compute surface energy components that were developed for the Wilhelmy plate method are also applicable for the Sessile drop method. In

contrast, in [60], the rate-dependence from stage velocities precludes a true determination of an intrinsic material property such as surface energy.

The long-term practical goal of adhesion testing in asphalt nanoindentation is to determine work of adhesion between binder and aggregate, which would require active monolayers of polar molecular groups attached to the indenter tip. Binder-aggregate interfacial failure is of primary concern in practical pavement conditions and environments. This interfacial energy will provide indications of the adhesive bond between aggregate and binder along with the level of debonding and stripping that can be caused by moisture damage.

## CHAPTER 4. MATERIALS & METHODS

### 4.1 Materials

The binders and mastics selected, shown in Table 1, are representative of a range of mechanical differences at room temperature. Two neat binders and one modified binder were considered in this study: a Performance Grade (PG) 64-22 North Carolina binder (source: Citgo Wilmington), a PG 70-22 North Carolina binder (source: Associated Greensboro), and a linear-grafted PG 70-28 SBS (styrene-butadiene-styrene) binder from the Federal Highway Administration's Accelerated Loading Facility (ALF).

For initial trials, two neat binders and one mastic (granite) were used for creep testing. The RTFO-aged tests demonstrate an improved experimental procedure with the additional of PG 70-28 SBS and a more structured, rigorous range of tested filler volume fractions. For cohesion testing, the thirty types of mastic used in this study were prepared using hydrated lime and granite filler (both non-inert), as manufactured and mineral fillers, in combination with PG 64-22, PG 70-22 and PG 70-28 SBS with varying filler dust-to-binder mass ratios (dust ratios) ranging from 0.3 to 1.29. These dust ratios correspond to filler volume fractions ( $\phi$ 's) in the range of 0.116 to 0.465 for granite and 0.111 to 0.477 for lime. At higher filler volume fractions, particle interactions dominate and mastic micromechanical theories become increasingly complex due to particle structuralization within mastics. For creep testing of RTFO-aged materials, a total of 24 mastics are prepared with the same three binders as in the cohesion testing, with dust ratios ranging from 0.6 to 1.29.

Table 1: All materials used in creep and cohesion testing

<b>Initial Trials</b>	<b>RTFO Aged</b>	
Creep Testing	Creep Testing	Cohesion Testing
	PG 70-28 SBS	PG 70-28 SBS
PG 70-22	PG 70-22	PG 70-22
PG 64-22	PG 64-22	PG 64-22
<b>granite filler</b>	<b>lime filler</b>	<b>lime filler</b>
	PG 70-28 SBS (0.6, 0.8, 1.0, 1.29 DR)	PG 70-28 SBS (0.3, 0.6, 0.8, 1.0, 1.29 DR)
PG 70-22 (0.67 DR)	PG 70-22 (0.6, 0.8, 1.0, 1.26 DR)	PG 70-22 (0.3, 0.6, 0.8, 1.0, 1.26 DR)
	PG 64-22 (0.6, 0.8, 1.0, 1.2 DR)	PG 64-22 (0.3, 0.6, 0.8, 1.0, 1.2 DR)
	<b>granite filler</b>	<b>granite filler</b>
	PG 70-28 SBS (0.6, 0.8, 1.0, 1.2 DR)	PG 70-28 SBS (0.3, 0.6, 0.8, 1.0, 1.2 DR)
	PG 70-22 (0.6, 0.8, 1.0, 1.2 DR)	PG 70-22 (0.3, 0.6, 0.8, 1.0, 1.2 DR)
	PG 64-22 (0.6, 0.8, 1.0, 1.2 DR)	PG 64-22 (0.3, 0.6, 0.8, 1.0, 1.2 DR)

## 4.2 Superpave Grading

A brief commentary is worth mentioning how the nomenclature of the binders relates to their strength properties. In the Superpave grading system, the grading is performed at elevated temperatures. A material becomes a PG 64-22 because it has a  $|G^*|$  above a certain threshold at 64 °C and a corresponding frequency, but below that threshold at 70 °C and the same frequency. Therefore, it is reasonable to conclude that a PG 70-22 binder will be stiffer at higher temperatures compared to a PG 64-22. However, there is no physical law stating that just because a material has a higher  $|G^*|$  at one temperature, it must also have a higher  $|G^*|$  at a different temperature and frequency. This statement is expected to be true over a relatively narrow range, within the range of the grading. The tested binders can be considered non-aging for the purposes of response predictions since little to no aging occurs over the time scales of the experiments.

### 4.3 Micrographs

A primary advantage of nanoindentation and other probe-based methods is the ability to optically visualize microstructures and infer conclusions regarding physical phenomena based on the combined knowledge of data and microstructural configurations. Binder is a colloidal dispersion of asphaltene micelles in maltenes, with the resins (polar components of the maltenes) stabilizing the asphaltene micelles [58].

Figure 2 shows pre-indentation micrographs of (a) PG 70-28 SBS binder, (b) PG 70-22 binder, and (c) PG 64-22 binder before indentation. Post-indentation micrographs show full recovery of (d) PG 70-28 SBS and (e) PG 64-22, along with micrographs of (f) baghouse fine granite dust and (g) hydrated lime filler. The colloidal structures of the binders can be deduced from each micrograph. A clearer comparison between PG 70-22 and PG 64-22 is shown in Figure 3. The networked association of asphaltenes, known as the bee-hive structure that has been reported in past literature [58], [60], is shown most clearly in Figure 3. Asphaltene is the component of asphalt binder that is insoluble in aliphatic solvents but soluble in aromatic solvents [58]. It has a highly polar molecular structure. The waxy molecules contained in asphaltene crystallize upon cooling to the testing temperature, resulting in highly insoluble organic compounds that form a phase-separated microstructure commonly known as the bee-hive structure [58]. These micrographs reinforce the molecular structure hypothesis of asphalt binder.

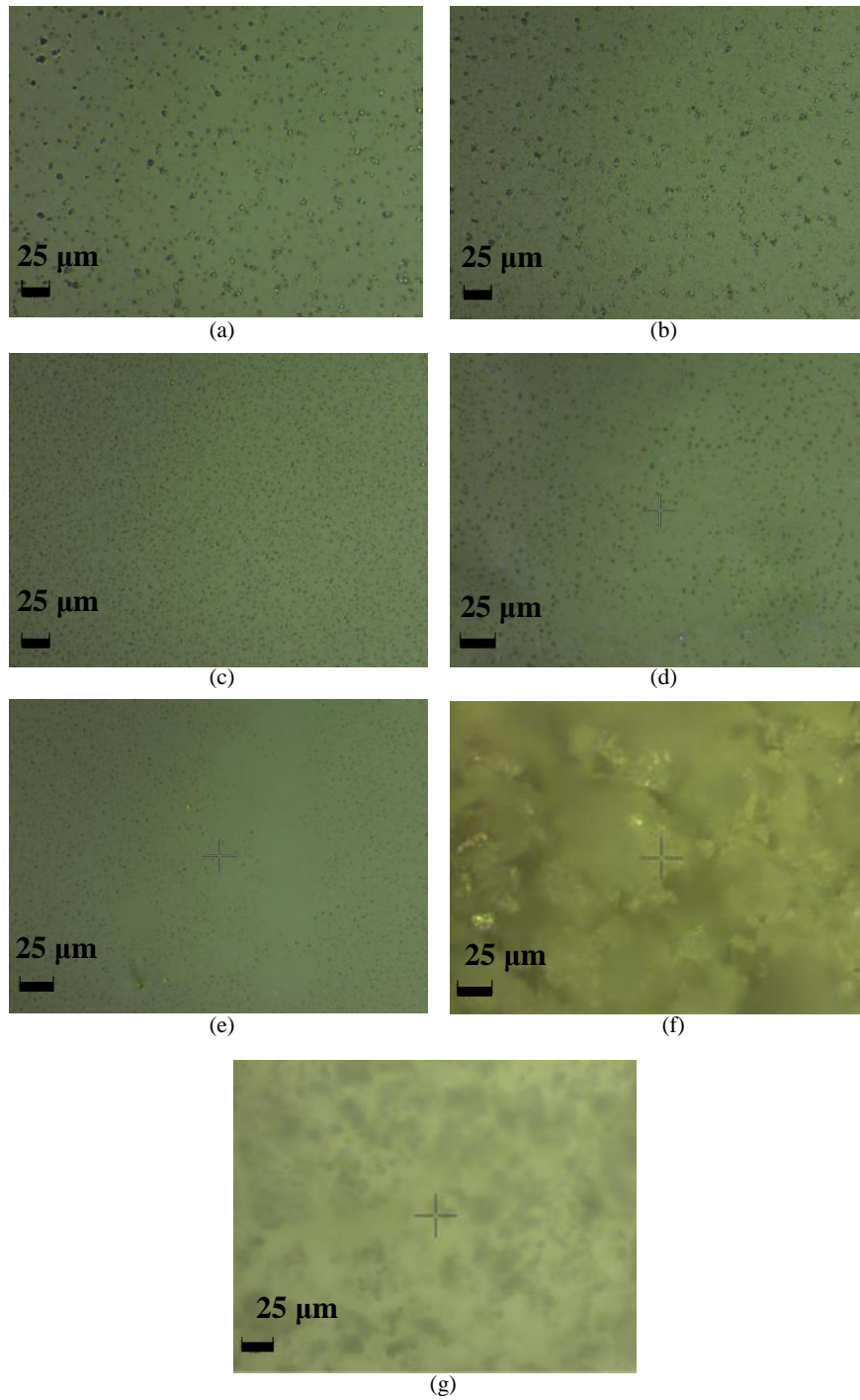


Figure 2: Asphalt binder and filler micrographs (316  $\mu\text{m}$  by 242  $\mu\text{m}$ ): (a) PG 70-28 SBS binder; (b) PG 70-22 binder; (c) PG 64-22 binder; (d) PG 70-28 SBS binder after full recovery; (e) PG 64-22 binder after full recovery; (f) Baghouse fine granite dust (mineral); (g) Hydrated lime filler (manufactured)

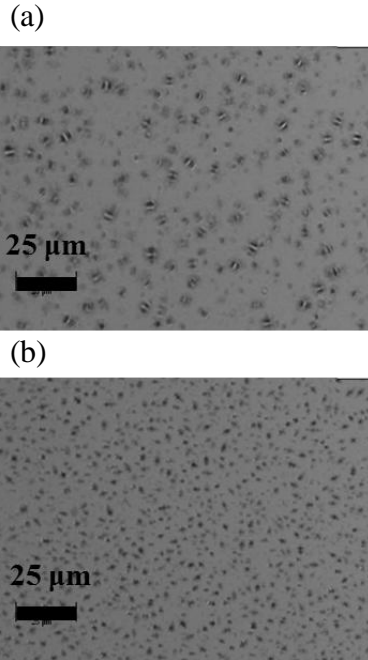


Figure 3: (a) PG 70-22 pre-indentation; (b) PG 64-22 pre-indentation

## 4.4 Methods

The methods used herein were specifically developed for and tailored to these materials, requiring years for complete experimental optimization. Nanoindentation tests at room temperature were conducted on these samples. Although tests were at room temperature, the viscous behavior of binder still plays a significant role in test results, and this behavior has the most significant contributions to rheological characterization.

### 4.4.1 Sample Preparation

Binder samples were prepared by heating in an oven at 120 °C for 30 minutes, and mastic samples were prepared by conditioning for the same time interval at 130 °C. Since filler will settle during mastic storage, mastics were agitated after heating and prior to pouring to

achieve a consistent filler distribution on the sample surface. The filler-binder mixing procedure consisted of a heating stage at 130 °C, uniform manual mixing for approximately 25 minutes for a dust ratio of 0.3, and electric mixing for all samples at and above a dust ratio of 0.6 for approximately 15 minutes. An electric mixer was used to improve material workability and uniformity during sample preparation.

Binder and mastic samples were poured into a small thimble of 0.635 cm height and 1.5875 cm radius. One of the benefits of using thimbles over thin films is not having concerns about substrate effects, which play a role in samples deposited on thin-filmed glass slides. The additional constraint in nanoindentation that the indentation depth should be less than 10% of the sample thickness is also avoided with the use of thimbles. Binder and mastic samples were slightly over-poured into the thimble in anticipation of volume shrinkage, and flat surfaces for testing are found near the middle of the sample.

#### **4.4.2 CSM Instruments Ultra-Nanoindenter (UNHT)**

The UNHT module is an independent two-tip system. Figure 4(a) shows a schematic of the construction of the nanoindenter. The reference ball, labeled “R” in Figure 4(a), needs to first land on a rigid surface. This challenge was solved by dropping an ultra-thin (0.00508 cm) stainless steel shim on the sample surface and landing the reference ball on this stainless steel shim. Once the reference ball lands, the indenter tip, labeled “I” in Figure 4(a) descends until contact is made. A typical filled thimble is shown in Figure 4(b). CSM’s Ultra-Nanoindentation Hardness Tester is pictured in Figure 4(c). This test-setup includes the optical microscope. CSM’s proprietary data acquisition software and module are used to monitor sensors for the stage position, feedback loops, and voltage signals over time. A voltage is converted into an applied tip load for acquiring force-displacement curves.

A sphero-conical diamond indenter tip is used, with a 1 μm radius sphere at the end of the tip transitioning to a cone with a 45° angle between the cone and sample surface. Room temperature was checked periodically during testing and was found to range from 21 °C to 23 °C.

The load on the reference ball was set to 500  $\mu\text{N}$ , the lowest recommended reference load for this machine. Reference sink-in is not an important concern for the stiffer mastics. For binder, one way to test for reference sink-in is by performing a pull-off test. Any potential reference sink-in would lead to a continuously decreasing pull-off tensile force. It will be shown that these trends in forces are not observed in any of the data; hence, sink-in is assumed to have a negligible influence on the measurement results.

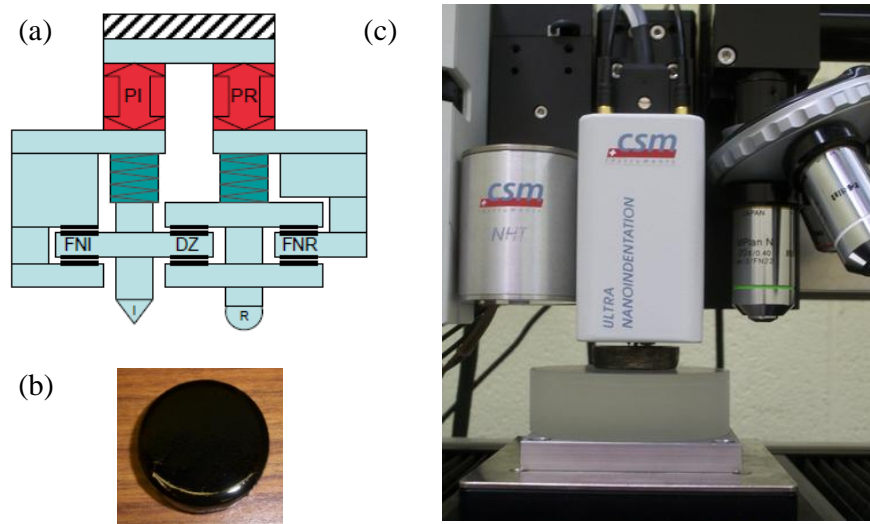


Figure 4: Nanoindentation test set-up: (a) Schematic of indenter construction; (b) 0.635 cm height and 1.5875 cm radius sample holder (thimble) with binder; (c) UNHT module in operation

With the exception of lower temperature tests reported in Section 6.4.4, all experiments were otherwise conducted at room temperature due to a lack of a cooling stage. The viscous behavior of binder still plays a significant role in room-temperature test results. Temperature is a critical factor driving asphalt's mechanical behavior. Thus, future research efforts will strive to incorporate temperature effects with a cooling stage to investigate glassy regions of binder and mastic mastercurves. Testing at higher temperatures with the nanoindenter would cause higher strains that may lead to nonlinear viscoelasticity.

#### 4.4.3 Experimental Methods for AFM

In addition to nanoindentation, AFM is conducted on the samples. AFM is a scanning probe microscopy technique allowing for study of the microstructure of materials through surface imaging. To collect AFM images, a Bruker Dimension 3000 AFM was used with a sharp silicon nitride probing tip in tapping mode. The tip has a diameter on the order of 10 nm (at the end of a cantilever), a laser diode set to reflect off of the back of the cantilever, and a position-sensitive photo detector. In tapping mode, a piezoelectric element is used to vertically oscillate the cantilever at certain amplitudes and intermittently make low force contact with the surface. This is the preferred mode for soft, adhesive, or fragile substances.

The cantilever tip is moved across the region of interest in a raster pattern, within a square area of 25 x 25  $\mu\text{m}$  in size for this research. The deflection response is captured as the instrument responds to surface features by varying vertical displacement to maintain constant damping of the oscillating cantilever spring on which the probe tip is mounted [58]. Due to the low forces used in AFM, the ability to operate under ambient temperatures, and the use of a physical probe (as opposed to the electron probe alternative of the SEM), the AFM is suited for studying material microstructure, particularly in opaque materials which are difficult to investigate with optical microscopy techniques.

Tapping mode can generate both height (topography) and phase contrast images. Height images provide information with respect to topography of various as the probing tip is raster scanned across the sample surface. Phase contrast images are generated relative to the time delay between the cantilever driving and response oscillations as the probing tip encounters various features on the sample surface [58]. The phase contrast image of tapping mode is dependent on tip-sample interaction and its effect on response lag of the cantilever's oscillations. Whether a phase lead or lag is experienced, the phase angle would increase proportionally to the phase shift. Phase contrast images are useful in identifying regions of varying cohesive, adhesive, and viscoelastic properties. For this research, images were collected for all aged binder types as well as mastics at dust ratios of 0.6 and the highest dust ratios, for both filler types.

#### 4.4.4 Experimental Challenges

The experimental challenges faced on this research were vast and wide-varying; experimentally, creep and cohesion curves of binder and mastic are extremely difficult to acquire. The primary experimental challenges were related to both sample preparation and software optimization. Once the sample is poured into the thimble at the height of the thimble rim, a concave meniscus of binder would form around the inner circumference of the thimble. One approach is to over-pour the sample, since it is known that asphalt shrinks as it cools. Once cooled at room temperature, the sample would need to be at least at rim level. Having the sample above rim level is also acceptable since another concern from under-pouring is the bottom of the UNHT module colliding with the rim before the indenter is able to reach the sample surface. This is not an issue with an over-poured sample.

A perfectly flat surface of uniform height is needed for nanoindentation testing. The middle of the sample is ideal for testing since the sample is flattest in this region. With the dual-tip UNHT system from CSM Instruments, the reference tip lands on a steel shim to avoid the sink-in effect from landing on pure binder or mastic, and the indenter tip will then descend with coarse (quick) and fine (slower) approaches once the reference tip has made contact.

Another experimental challenge was the issue of zero-point errors, where it becomes difficult for the software to detect precisely when the indenter comes into contact with the sample. This is a common issue for highly viscous materials where ultra-low testing loads are used. This was solved by setting the contact load to the noise floor of the instrument (3  $\mu\text{N}$ ). The contact load would then rise until the maximum load is reached. Since commonly used spherical tips in nanoindentation are around 50-200 nm in radius [54], the smaller tip that was selected has greater sensitivity in detection capabilities.

Setting up a grid in viscoelastic nanoindentation is highly complex because each indent creates a “volcano”-type necking effect upon linear retraction, and consequently the surface may not be perfectly flat throughout the entire lateral distance of the grid. The volcano shape is a property of both tip retraction and high material cohesion, with the end

result being a temporary residual surface topography above the original, undeformed sample surface. It is important to move the tip a sufficient distance away from this effect after each indent to avoid residual stress concentrations, uneven surface profiles, and surface detection errors, which will either distort results or terminate the test. A sufficiently large grid spacing (70  $\mu\text{m}$ ) between successive indents was used to avoid stress fields and topographical interferences from previous indents, and a high approach distance (distance above the sample surface at which data collection begins) was set to account for surface phenomena.

Feedback control loop oscillations were another complicating factor. The load and displacement signals would frequently oscillate due to large creeping deformations for excessively long hold times, relative to more traditional deformations experienced in nanoindentation testing on the order of a few hundred nanometers. Because the reference and indenter tips move independently, the approach conditions can be very challenging, and any surface roughness on the soft materials can exacerbate the problem. The contact points of indenter-asphalt detection are sometimes not easily observable when attempting contact point corrections. Since only a limited amount of information can be acquired directly from a force-displacement nanoindentation curve, post-processing must be used for a majority of the analysis.

## **4.5 Loading Procedures**

### **4.5.1 Creep Loading Procedures and Commentary**

Choosing the proper loading conditions and procedures is the most important step in nanoindentation experiments on viscoelastic materials. Significant trial and error determined an optimal set of input loading conditions for accurate extraction of the relevant outputs. The primary criteria for this trial and error were repeatability in the grid indentation technique.

In this study, the indentation results for a 1  $\mu\text{m}$  diamond tip radius are presented. A 100  $\mu\text{m}$  was also briefly used to explore effects of changing parameters on larger tip radii, but only 1  $\mu\text{m}$  results are provided in this dissertation since the gathered data is

comprehensive. However, with a 100  $\mu\text{m}$  tip, one is able to achieve higher contact loads (hundreds of  $\mu\text{N}$ ) at lower penetration depths than with a 1  $\mu\text{m}$  tip. The tradeoffs, however, are a greater activated sample volume probed, larger residual stress/strain fields, and scale and phase separability issues.

The initial magnitudes of the maximum loads were selected through exhaustive enumeration followed by selective refinement. The range was refined with a lower limit to avoid instrumental sensitivities and drifts in detection capabilities for a smaller tip as the loads approach the noise floor. The range was refined with an upper limit to satisfy the length scale separability condition for the penetration depths reached, given the characteristic sizes of the filler particles.

Scale separability for continuum analysis requires the characteristic size of the largest microstructural heterogeneity (i.e., the filler particle in mastic) to be much smaller than the maximum indentation depth to extract composite properties that are representative of a homogenized response. As the maximum indentation depth decreases for a sphero-conical indenter with larger sphere radius (due to higher bluntness), this depth begins approaching the characteristic filler size. A smaller tip size activates a smaller probed volume and more easily satisfies the scale separability condition. For this reason, the choice of a smaller 1  $\mu\text{m}$  radius sphero-conical tip was reasonable. A flat-ended punch indenter tip would have had a similar scale separability issue as a sphero-conical indenter with larger sphere radius, while presenting other experimental difficulties, including alignment of the flat punch. Flat punches are analytically convenient but are generally much larger than contact areas from sharper tips and therefore probe larger length scales. Flat punches are also sharp at the corners, which could disrupt contact stress and strain field continuity by causing excessive stress concentrations that lead to micro-damage and a nonlinear response of asphalt binder [87]. A sharp tip touches less surface area, but penetrates deeper and can generate high stress concentrations compared to an internal area of a blunter tip. A 1  $\mu\text{m}$  radius sphero-conical tip minimizes plastic deformation and accompanying overestimations of stiffness while achieving interaction volumes at the scale of asphalt binder and improved stress uniformity from the tip-sample contact interface.

Creep and cohesion are accounted for in separate types of nanoindentation curves, each having a unique loading program with unique loading conditions. Attempting to account for creep and cohesion in a single curve would lead to inaccuracies since the time-delayed creeping will affect adhesion measurements during unloading. For creep measurements, a ramp-and-hold loading with minimal rise time is used as the closest experimental alternative to the ideal Heaviside step loading. The preloading period, before the peak load is reached, is inversely proportional to the preloading rate. The 15 creep loading programs used per material are listed in Table 2.

Table 2: The set of 15 creep loading programs used per sample

	(a) Max Load ( $\mu\text{N}$ )	(b) Loading Rate ( $\mu\text{N/s}$ )	(c) Hold Time (s)
1)	15	5000	70
2)	20	5000	70
3)	25	5000	70
4)	30	5000	70
5)	35	5000	70
6)	15	5500	70
7)	15	6000	70
8)	15	6500	70
9)	15	7000	70
10)	15	7500	70
11)	15	5000	50
12)	15	5000	55
13)	15	5000	60
14)	15	5000	65
15)	15	5000	70

The fitted parameters for the assumed creep model are averaged for each loading program of the appropriate curves. While the nominal maximum contact loads for nanoindentation creep testing fell within the range of 15-35  $\mu\text{N}$ , the actual maximum contact loads experienced by the sample deviated slightly from this range, due to limitations of

instrument sensitivity. Practically, the creep phase of a nanoindentation creep test is limited to 70 seconds partly because, relative to sample displacement rates, displacement piezo signal drift rates become amplified over longer data acquisition durations. While 10 seconds is insufficiently low to characterize any meaningful creep, hold times around 70 seconds still maintain LVE and are within the displacement piezo ranges of the data acquisition system. Also, since the hold times are sufficiently large, we can expect to see creep rate independence from the loading rate [72], and the optimal parameters are determined to be loading-condition independent. Similar parameters were output for each material-specific loading case regardless of the input parameters used.

A fast loading ramp (short rise time) strengthens the expectation for a full creep response and allows less emphasis to be placed on the actual hold time for the creep load. Faster ramps help overcome initial transient responses more quickly. For slow ramps, the creep is largely exhausted during the ramping, which is considered a transient behavior, and there is a minimal degree of creep response during the actual creep phase.

These issues should all be considered in the decision of an optimal hold time. A practical lower limit was selected that minimizes the adverse effects of all these competing factors. Longer hold times beyond 70 seconds were also considered for investigating the long-term creep behavior. However, experimental conditions preclude setting the hold time for creep testing to longer than approximately 70 seconds due to issues such as tip depth saturation (the maximum indenter piezo depth range for our module is 50  $\mu\text{m}$ ), introduction of nonlinear viscoelasticity at high strains, non-convergence of the selected creep compliance model to experimental data, incompatibility of feedback loop parameters with the loading programs, and instrument instability.

To avoid data cluttering, only representative curves are shown throughout this dissertation. After significant adjustments to software feedback loop parameters and experimental setup modifications, such curves are the most representative of appropriate creep and cohesion curves that can be achieved at this time with CSM Instruments' UNHT Ultra Nanoindentation tester. Figure 5 shows a typical nanoindentation curve on fused silica, the most commonly used calibration standard. This can be compared to representative

nanindentation curves for Figure 5(b) cohesion and Figure 5(c) monotonic compressive creep loading behaviors. We notice significant penetration into the binder in Figure 5(c) compared to that of stiff materials, such as fused silica in Figure 5(a).

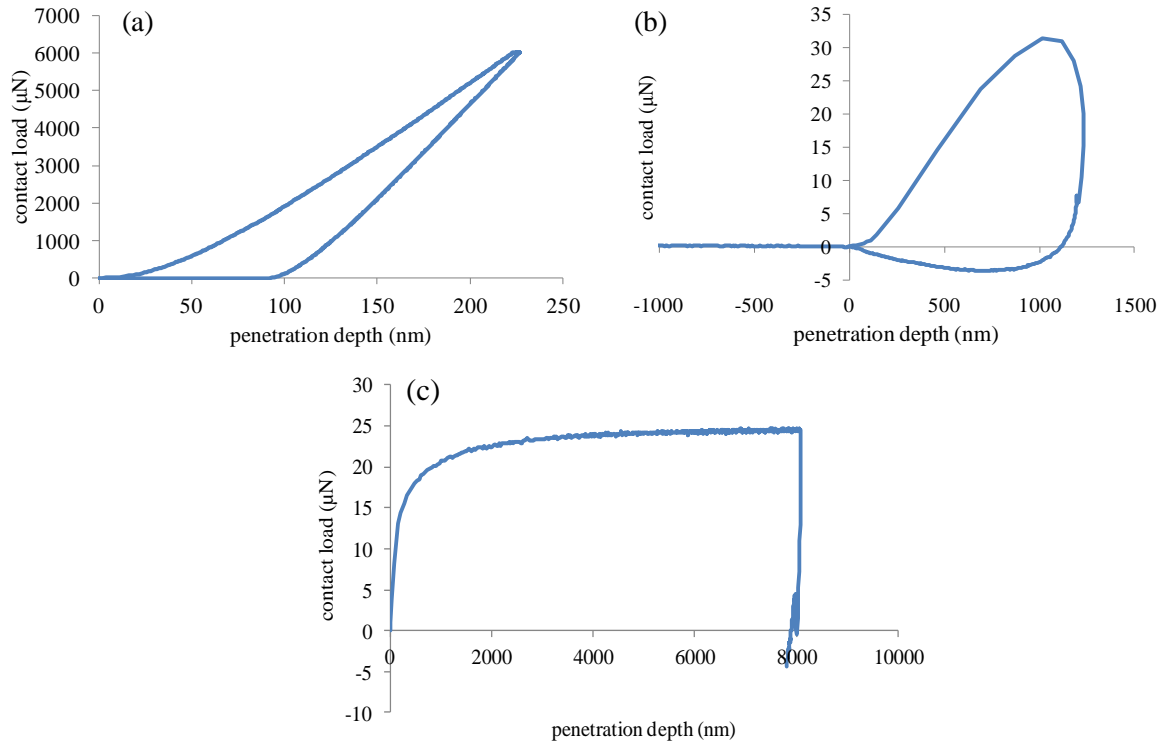


Figure 5: (a) typical rigid material curve; (b) binder cohesion curve; (c) binder creep curve

Oliver-Pharr analysis cannot be used since for time-dependent materials, the assumption of elastic unloading is invalidated by the continuing time-dependent creep deformation and by cohesion, both of which oppose the retraction. Although the unloading curve of binder or mastic may show a steep positive slope, which would traditionally indicate a high stiffness value, this slope is misleading in this situation because time-dependency and cohesive effects interfere with a reasonable application of the Oliver-Pharr method.

The fast unloading rate and high cohesion develop the high tensile force which contributes to a steeply-sloped unload, a near-vertical slope (Figure 5(c)), or even a negative

slope for a creeping material when an unloading “nose” or “bulge” appears. Shear viscosity impacts the degree of bulging that occurs at the onset of unloading. The negative, tensile forces observed in Figure 5(b) demonstrate the viscous nature of the sample. Even though elastic modulus and hardness are not of concern in this research, an apparent elastic modulus calculated by the Oliver-Pharr method, based on the unloading slope, would be artificially high.

The forward-going displacement due to creep, operating under a time delayed action, overwhelms the elastic recovery. For this reason, a number of experimental and numerical tricks have been introduced to attempt to “correct” the unloading slope and force the possibility of using the OP method onto creeping materials. These tricks including exhausting the creep prior to unloading with a long hold time at peak load, or attempting to outpace the creep with a fast unload [54]. These treatments are aimed at minimizing the effect of creep in order to obtain quantitative measurements of Young’s modulus and hardness, but these methods that use OP analysis avoid the goal of understanding exactly what a creeping material is. Since our primary goal is to characterize full mechanical response, OP analysis is ruled out. Providing just elastic modulus and hardness values for asphalt is a meaningless endeavor as they should be accompanied by a corresponding frequency and temperature for a realistic time-dependent characterization. In this research, data analysis based on elastic-viscoelastic correspondence principle is used.

Most load-controlled indentation studies that use elastic-viscoelastic correspondence have assumed step-loading (Heaviside function) creep conditions. A step loading is analytically convenient but experimentally impossible to implement. Feedback control loop and input parameter modifications, as described in this section, are implemented to get as close as possible to a step loading for creep testing.

#### **4.5.2 Cohesion Loading Procedures and Commentary**

For cohesion testing, similar broad challenges as observed in creep testing were experienced. The primary criterion for data acceptance was a cohesive force that reached a

maximum negative pull-of force before returning to zero contact load. An immediate unload follows the loading cycle to determine an appropriate pull-off force. In the cohesion loading program, the creep hold time is set to the minimum possible in the software (0.1 s) to minimize creep effects from interfering with cohesion data collection. For the generated grids, the loading rate is varied between a relatively high 8000 and 12000  $\mu\text{N}/\text{min}$ , the unload rate is set to 3000  $\mu\text{N}/\text{min}$ , the retract speed is set to 4500  $\text{nm}/\text{min}$ , and the retract time is set to 120 seconds. Higher loading rates are used in cohesion than creep testing for RTFO-aged materials to “ramp up” the tip into the material more quickly, since the tip will be immediately unloaded in cohesion testing. This approach strikes a better balance between higher loading rate and lower hold time to achieve improved cohesion measurements.

The retract speed and time refer to the portion of the indentation test where tensile forces are felt on the tip after loading and unloading. The actual maximum loads experienced by the samples for all collected cohesion tests ranged mostly from 7 to 45  $\mu\text{N}$ , due to limitations in instrument sensitivity. The contact depths become negative during the course of the unloading cycle. This indicates that the material is resisting the unloading of the tip with a tensile force. Negative contact depths imply that the tip is retracting above its original zeroed position.

# CHAPTER 5. ANALYSIS FOR CREEP COMPLIANCE AND COHESION

## 5.1 Governing Equation for Creep

Before deriving the governing equation, we must first select the real tip geometry used for this derivation of the constitutive relationship between penetration depth and creep compliance that will form the mathematical basis for the modeling scheme.

Nanoindentation can be considered as a process of indenting a half-space with a rigid indenter. For a 1  $\mu\text{m}$  tip, since the tip radius is so small, the spherical indenter can be modeled as an axisymmetric conical indenter with an effective cone angle of 45°. The selection of a conical tip implies that the conical area dominates binder-surface interactions. For the spherical part, the radius of the contact area is given by [84]

$$r^2 = R^2 - (R - h_c)^2 \quad (8)$$

where  $r$  is the radius of the projected contact circle at the contact depth  $h_c$ . A schematic is shown in Figure 6 [84].

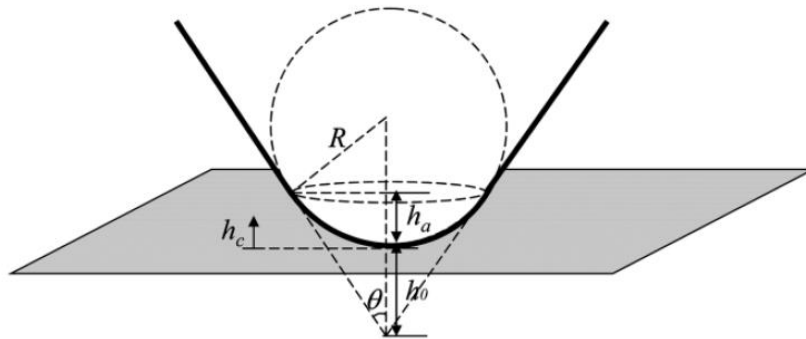


Figure 6: Sphero-conical indenter

For the conical part, the radius of the contact area is given by

$$r = (h_c + h_0) \tan \theta \quad (9)$$

where  $h_0$  is the distance between the apex of the indenter tip and the apex point of the equivalent conical indenter, as shown in Figure 6. The distance  $h_0$  is calculated as

$$h_0 = \frac{R}{\sin \theta} - R \quad (10)$$

The area functions for the spherical and conical parts are given by

$$A_{\text{spherical}} = \pi h_c (2R - h_c) \text{ for } h_c \leq h_a \quad (11)$$

and

$$A_{\text{conical}} = \pi \tan^2 \theta (h_c + h_0)^2 \text{ for } h_c > h_a \quad (12)$$

where the change from  $A_{\text{spherical}}$  to  $A_{\text{conical}}$  occurs at

$$h_a = R - R \sin \theta \quad (13)$$

With the nominal, stock values of  $R = 1.03 \mu\text{m}$  and  $\theta = 45.1^\circ$ , it is determined that  $h_a = 104 \mu\text{m}$  and thus, based on the penetration depths of our actual indents,  $h_c > h_a$  in all cases by a significant margin. Thus, only the conical part of the indenter is considered for both creep and cohesion analysis in this “sphero-conical” tip.

The derivation is now presented for the governing constitutive relationship between indentation depth and creep compliance for a conical indenter, which will form the basis for the creep data analysis. To extract LVE material properties of a representative volume element from the time-dependent load-displacement response, a moving boundary value problem must be solved. Lee and Radok’s hereditary integral operator method solves for the

stresses and deformations based on the associated solution for a linear elastic material. This method determines the viscoelastic counterpart of the associated Hertzian solution.

For the indentation of a rigid axisymmetric indenter into a half-space composed of a homogeneous, linear elastic, and isotropic material, Sneddon has derived the indentation load-displacement relation. The indentation depth  $h$  of the tip of a punch of arbitrary profile, for an axisymmetric indenter tip, is represented in terms of the indenter geometry by [69]

$$h = \int_0^1 \frac{f'(x)dx}{\sqrt{1-x^2}} \quad (14)$$

where  $z = f(x)$  is the shape function for an axisymmetric indenter. This expression is determined for a Boussinesq problem of arbitrary indenter punch profile. The indentation load on an axisymmetric indenter is then determined as [42], [69]

$$P = \frac{4Ga}{1-\nu} \int_0^1 \frac{x^2 f'(x)dx}{\sqrt{1-x^2}} \quad (15)$$

where  $a$  is the radius of the contact circle at depth  $h_c$ ,  $G$  is the shear modulus, and  $\nu$  is Poisson's ratio. For indentation by a conical indenter

$$z = f(x) = ax \tan \alpha \quad (16)$$

where  $\alpha$  is the angle between the cone generator and substrate plane as shown in Figure 7. Figure 7 shows a snapshot of the loading phase for an indentation procedure with a sphero-conical tip, at any point during tip-sample contact.

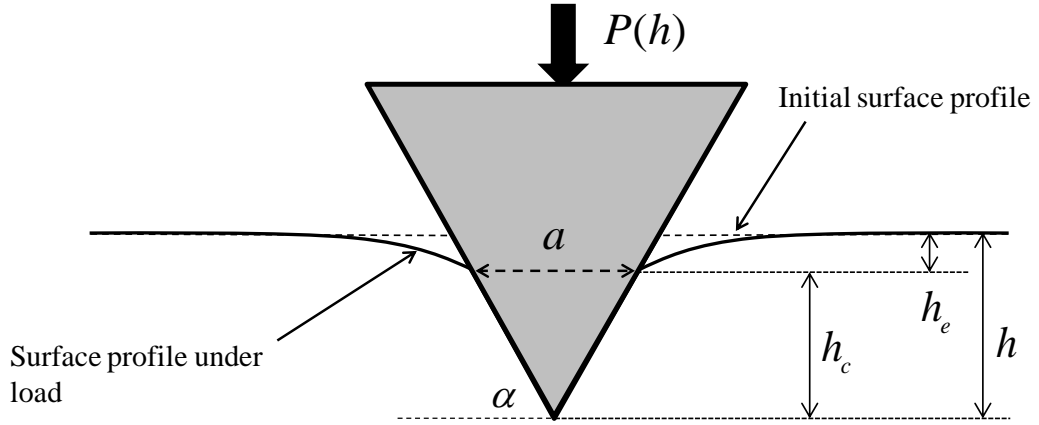


Figure 7: Schematic of conical indenter geometry

With the substitution of the shape function for a conical indenter, the indentation depth in Equation (14) becomes

$$h = \frac{1}{2} \pi a \tan \alpha \quad (17)$$

The indentation load in Equation (15) becomes

$$P = \frac{\pi G a^2}{1-\nu} \tan \alpha \quad (18)$$

Therefore, using the shape function  $z = f(x)$ , the relationship between indentation load and depth for a conical indenter, derived from Equations (17) and (18), becomes

$$P = \frac{4}{\pi(1-\nu) \tan \alpha} G h^2 \quad (19)$$

As a generalized case, in Sneddon's solution the indentation force is proportional to the penetration depth as

$$P \propto h^q \quad (20)$$

where  $q$  is dependent on the indenter shape.

As previously mentioned, indentation of a rigid indenter into a half-space composed of a LVE material is a quasi-static boundary value problem with a moving boundary between the indenter and half-space as the contact area and half-space behavior both change with time. Applying Lee and Radok's technique of using the hereditary integral operator leads to the following time-dependent indentation depth under a prescribed loading history in a linear viscoelastic material [35], [42]

$$h^2(t) = \frac{\pi(1-\nu) \tan \alpha}{4} \int_0^t D(t-\xi) \left[ \frac{dP(\xi)}{d\xi} \right] d\xi \quad (21)$$

where  $D(t)$  is the contact creep compliance function,  $\xi$  represents the time corresponding to the onset of an applied load, and  $\nu$  is Poisson's ratio. This expression is the governing equation for conical indentation of a viscoelastic material and takes into account the change in contact area with penetration depth. With assumed incompressibility (constant  $\nu = 0.5$ ) and  $\alpha = 45^\circ$ , the governing equation becomes

$$h^2(t) = \frac{\pi}{8} \int_0^t D(t-\xi) \left[ \frac{dP(\xi)}{d\xi} \right] d\xi \quad (22)$$

Alternatively, we can approach the derivation through operators [19]. The convolution integral can be expressed as

$$D \otimes \dot{P} = \int_0^t D(t-\xi) \frac{dP(\xi)}{d\xi} d\xi \quad (23)$$

where the mathematical operator  $\otimes$  denotes the convolution and the dot denotes the time derivative. The load function is given by

$$\dot{P} = P_0 \cdot \delta(t_0) \quad (24)$$

where  $P_0$  is the prescribed indentation load for the hold period,  $\delta(t_0)$  is the Dirac delta function and  $t_0 = 0$  is the excitation time. In this case, the convolution integral simplifies to

$$D \otimes \dot{P} = D(t) \cdot P_0 \quad (25)$$

The relationship for conical viscoelastic indentation is [60]

$$h^2(t) = \frac{\pi}{2} \frac{1-\nu^2}{\cot \alpha} P_0 \cdot D(t) \quad (26)$$

which can be expressed as

$$h^2(t) = \frac{\pi}{2} \frac{1-\nu^2}{\cot \alpha} \frac{P_0}{E(t)} \quad (27)$$

The linear elastic expression for shear modulus

$$G = \frac{E}{2(1+\nu)} \quad (28)$$

can be applied over narrow time ranges such that

$$h^2(t) = \frac{\pi}{4} \frac{1}{\cot \alpha} \frac{1-\nu^2}{1+\nu} \frac{P_0}{G(t)} \quad (29)$$

for which we can see that the geometric constant  $\frac{\pi}{4} \frac{1}{\cot \alpha} \frac{1-\nu^2}{1+\nu}$  is equivalent to that of

Equation

(21). Using this operator approach, the expression for  $h^2(t)$  can be re-written as

$$h^2(t) = \frac{\pi}{8} \left[ \frac{P}{2G} \right] \quad (30)$$

This corresponds to a viscoelastic Boltzmann integral equation where the quantity  $\left[ \frac{P}{2G} \right]$  is replaced by the following viscoelastic integral operator for creep:

$$h^2(t) = \frac{\pi}{8} \int_0^t D(t-\xi) \left[ \frac{dP(\xi)}{d\xi} \right] d\xi \quad (31)$$

When the assumption of LVE is valid, this method, based on the elastic-viscoelastic correspondence principle with the Boltzmann integral operator, can also be used for a particular form of creep compliance. In both cases, the same final constitutive expression (Equation (31)) is attained.

## 5.2 Generalized Power Law (GPL)

Once the precise tip geometry and constitutive relations have been established, the next step is selecting the creep compliance functional form to extract physically meaningful optimal parameters. An a priori generalized representation of creep compliance is formed as the unit response function for the constitutive relationship between penetration depth and creep compliance. Due to the nonlinearities in material behavior and viscoelastic contact mechanics, current experimental investigations of creep compliance typically assume particular functions to fit the creep response [76].

Elastic-viscoelastic correspondence analysis for moving boundary values is used to generate solutions for creep at fixed loads, following constant-rate ramp loading to a peak load over an experimentally reasonable timeframe. The Boltzmann superposition principle is then implemented within the context of the viscoelastic correspondence problem. The Boltzmann superposition principle is a mathematical statement of linear viscoelastic behavior. The principle states that creep is a function of the entire loading history, and each loading step makes an independent contribution to the final deformation. The final deformation is a superposition of the individual contributions.

The general representation of the creep compliance function, based on the GPL, is fit to load-displacement curve data using least squares regression to find a set of best-fit parameters for the creep compliance. While a Prony series has the advantage of more accurate predictions for creep compliance trends for broadband data and is more responsive

to local disturbances, the GPL has greater simplicity and can satisfactorily describe the glassy and transition behaviors [57]. With a Prony series, physical understanding of the model in terms of its constituent components is diminished as more elements are added. Huang et al. go so far as to state that the mechanical parameters associated with the two elements of a typical Burgers model have no physical meaning. However, they have analogies to equivalent circuits [23]. Although the GPL does not provide a good representation of rubbery, Newtonian behavior at long times and low frequencies, asphalt binder and mastic only have glassy asymptotes (Figure 8) so the concavities of their mastercurves will not switch.

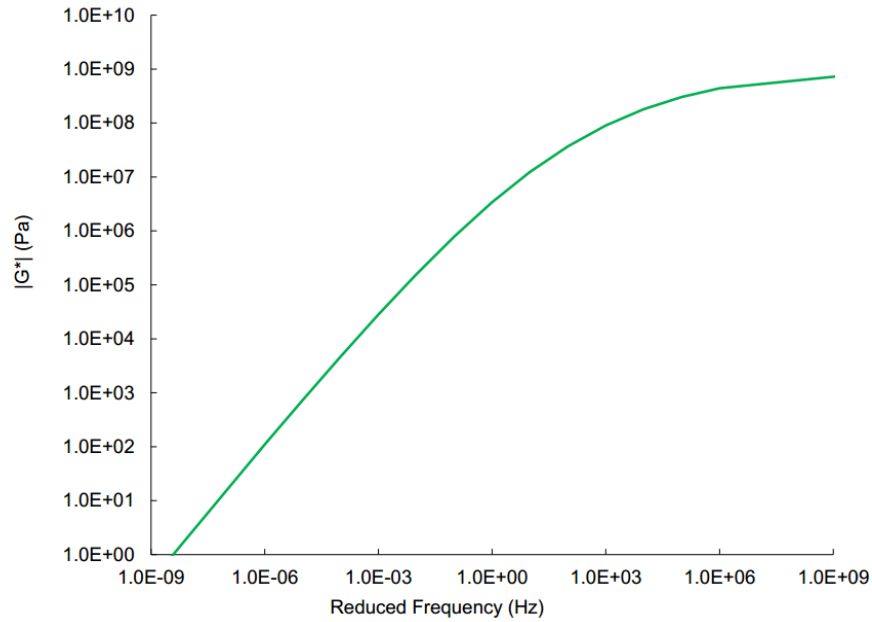


Figure 8: Representative complex modulus mastercurve for binder and mastic

Additionally, it is better to start with the simplest expression available and increase complexity as needed. The GPL has fewer parameters than the various Prony series representations based on Maxwell and Voigt mechanical analogs, making it easier to understand relationships between parameters. Since these creep experiments are over such a

short time scale, using many Prony series elements will not improve the robustness of the fit since broad trends are not currently being captured. Although the GPL is less commonly used today than the Prony series in mixture rheological modeling since it does not have points of inflection, it is acceptable for binder and mastic modeling since binder and mastic do not display typical “S”-shaped mastercurves. Using GPL also provides direct inputs for constructing a mastercurve of  $|E^*|$  vs. frequency [37]. By comparison, one of the most common models used in the asphalt community for mastercurves is the Christensen-Anderson-Marasteanu (CAM) model [44]. The GPL expression takes on the form

$$D(t) = D_0 + D_1 t^n \quad (32)$$

where  $D_0$ ,  $D_1$ , and  $n$  are regression coefficients. There is a boundary condition requirement for a non-decreasing contact area for the hereditary integral operator method, rendering the unloading phase analytically inapplicable [36]. It is also emphasized that load, and not stress, is maintained constant in these creep experiments. The stresses under the tip-sample interface are decreasing as the contact area is increasing, leading to stress relaxation.

### 5.3 Modeling Scheme

With the GPL selection, we can now construct a suitable modeling scheme to accurately and consistently extract the optimal creep response parameters. A fit-and-predict scheme is used whereby the creep functional form is evaluated by using the results from one set of experimental conditions and applying these results against a second set of data obtained using different loading conditions (maximum creep load, loading rate, or hold time) for the same material [54]. A true fit will have loading condition independence from the optimal parameters.

In this analysis, any net load input history for a load-time curve can be approximated by (and decomposed into) the sum of a series of pulse functions which represent pulse increments in load [33]. These pulses correspond to step functions [33] of both penetration

depth and  $h_c(t)^2$ . In essence, the convolution integral is numerically solved as many times as there are time intervals in the software's data acquisition system, and superposition is used to describe the updated model for  $h_c(t)^2$  at the latest time interval by adding all the pulse contributions together. The principle of causality is invoked to include only pulses prior to or up to the present time. Since the time steps from the software are very small (approximately 0.1 seconds), this numerical technique allows for the most accurate predictions.

When any load-time curve net load input history is approximated by the sum of a series of step functions corresponding to load pulse increments, at each jump in load

$$D(t - \xi) = D(t - t_i) \quad (33)$$

where  $t_i$  represents each time point in the data acquisition software. The width of each time step in the load-time data is the difference in consecutive time increments from the software. Within the range of each jump, the unit response function  $D(t)$  is constant.

Since the creep compliance is constant within the “instantaneous” time of the jump  $[t_i^-, t_i^+]$ , the governing expression of Equation (31) reduces to

$$h^2(t) = \frac{\pi}{8} D(t - t_i) \int_0^t dP(\xi) \quad (34)$$

Nanoindentation creep tests include a constant load, after an initial ramp, but the stress constantly changes with increasing penetration depth. Thus, true creep compliance cannot be directly determined even if the assumption of instantaneous loading is used. Therefore, the only way to extract creep compliance is through an assumed model form, which prohibits application of time-temperature superposition as is conventionally done in viscoelastic characterization of materials. The majority of current experimental investigations of creep compliance also assume particular functions to fit the creep response, based on the most suitable functional form (usually Prony series, generalized power law,

modified power law, or sigmoidal function). This approach is selected in this research with confidence.

Once numerical integration has been performed for the loading program with MATLAB and the data is fit to the integration results, a back-calculated creep compliance function is determined from the fitted parameters of the generalized functional form. The modeling scheme is graphically depicted in Figure 9, which represents creep as a function of the entire loading history. The final deformation is a superposition of the individual, independent contributions from each loading step in accordance with the theory behind the Boltzmann superposition principle.

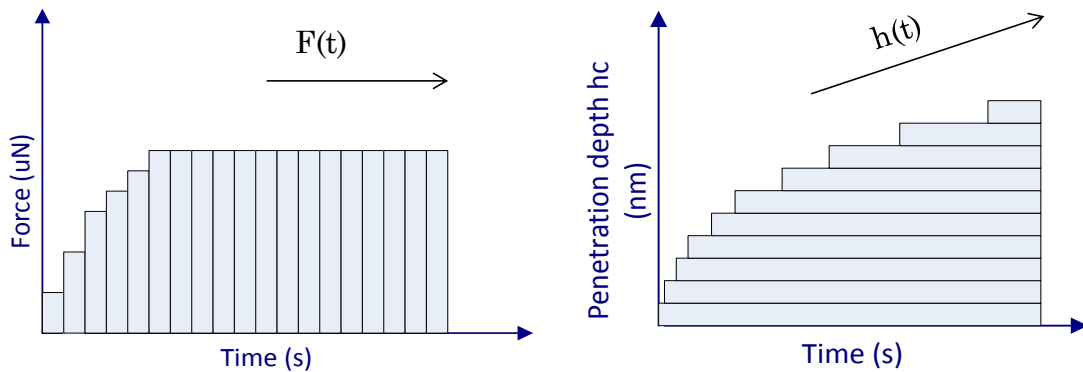


Figure 9: Schematic of numerical modeling approach for constitutive relation

## 5.4 Limitations of the Chosen Model

It is necessary to highlight a caveat of viscoelastic nanoindentation testing, especially when comparing this method to traditional creep testing methods. The stress and strain fields within a sample during indentation are complex, for all indenter shapes, even if it is assumed that the material can be treated as an isotropic continuum. While the measured outputs are dependent on the constitutive load-displacement-time relationships characterizing material behavior, inferring these relations from output data presents significant challenges [15]. There has been recognition of the significance of a full creep response, including all creep

phases, as a complicating factor for the extraction of parameters from a functional form of creep compliance, and universally robust and reliable methodologies have yet to be determined [15].

Most current methodologies tend to focus on steady-state, secondary creep, with the assumption that the influence of primary creep can be neglected due to its transient nature. While this is possible in conventional creep testing where constant stress fields exist, this is a highly complex problem in nanoindentation since regions of the sample undergoing primary creep are continually entering the steady-state creep strain field and influencing the indenter displacement response [15].

In reality, the system may not be conforming to any steady state regime but rather to a “quasi-steady-state,” which can occur relatively quickly. The stress and strain fields under the indenter are continually changing, and local regions are constantly moving along independent creep strain paths [15]. Some of these regions could be in primary creep phase even after an extended period of indentation. There is no requirement that the resultant indenter displacement history should be linear at any stage, although it is certainly possible that it could be at least approximately linear. Stress and strain histories should also be considered for materials with time memories.

If attempts are made to treat an indenter displacement history as if it were a “true” creep strain history, problems may arise with identifying a unique strain, unique strain-rate, and representative stress after a specified time. In essence, there may not necessarily be a justification for representing the actual indentation conditions as if they correspond to a uniformly loaded sample experiencing these “equivalent” stresses and strains. The inclusion of primary creep within the functional form in this research could very well be contributing to higher sensitivities governing the creep behavior, especially since primary creep exhibits higher stresses and strain rates than secondary creep. These are all issues that are manifesting themselves in different ways through a simple GPL representation of creep behavior.

## 5.5 Analytic Formulations for Interconversions

### 5.5.1 Options for Interconversion to Shear Relaxation Modulus

Once the modeling scheme has been implemented in MATLAB, it is necessary to interconvert the resulting creep compliance function to its counterpart relaxation modulus. In this research, only creep responses were determined directly. Through post-processing, well-known interconversion techniques were used to transform the creep compliance into a shear relaxation modulus.

From the principles of linear viscoelasticity, uniaxial stress and strain are related through the following convolution integral:

$$\sigma = \int_0^t E(t-\tau) \frac{d\varepsilon}{d\tau} d\tau \quad (35)$$

In creep testing, when the stress input is unity (the Heaviside function), the strain response is represented by creep compliance. Equation (35) can be written as [31]

$$1 = \int_0^t E(t-\tau) \frac{dD(\tau)}{d\tau} d\tau \quad (36)$$

Taking the Laplace transformation of both sides yields

$$s^2 \mathcal{L}\{D(t)\} \mathcal{L}\{E(t)\} = 1 \quad (37)$$

where  $\mathcal{L}\{f(t)\}$  is the Laplace transformation of a function  $f(t)$  and  $s$  is a real constant. An LVE material can be approximately represented by a pure power law for small ranges in its transition zone, where

$$\begin{aligned} E(t) &= E_1 t^{-n} \\ D(t) &= D_1 t^n \end{aligned} \quad (38)$$

When the case of pure power law applies,  $D(t) = D_1 t^n$  can be reduced through the Gamma function and its properties to Equation (35), a form which was proposed by Leaderman in 1958 for pure power law (PPL) [34]:

$$D(t)E(t) = \frac{\sin(n\pi)}{n\pi} \quad (39)$$

This form was derived from the principle that

$$\tilde{E} = \frac{1}{\tilde{D}} \quad (40)$$

for non-aging, LVE materials, where  $\tilde{E}$  and  $\tilde{D}$  are Carson-transformed modulus and compliance, respectively. When PPL is assumed, we use the Gamma function and the property that

$$\Gamma(n)\Gamma(1-n) = \frac{\pi}{\sin(n\pi)} \quad (41)$$

to arrive at the expression in Equation (39). Given the limited scale of fitting accuracy for PPL, this is not selected as an interconversion. There are various other forms available for interconversion. Denby presented the following interrelationship:

$$D(t)E(t) = \frac{1}{1 + \frac{n^2 \pi^2}{6}} \quad (42)$$

which holds true as long as both functions  $E(t)$  and  $D(t)$  exhibit broadband, smooth variation on log-log scales [16].

Christensen developed an interconversion using approximate relationships between the real and imaginary parts of a complex material function, and between the transient function and the real part of the complex material function [9]. This is determined as

$$D(t) \cong \frac{E(t)}{E^2(t) + \frac{\pi^2 t^2}{4} \left\{ \frac{dE(t)}{dt} \right\}^2} \quad (43)$$

In terms of  $n$ , this can be expressed as

$$D(t)E(t) = \frac{1}{1 + \frac{n^2 \pi^2}{4}} \quad (44)$$

We choose Denby's model, Equation (42), for smooth broadband model variation on a log-log scale. Using the GPL, the tensile relaxation modulus becomes

$$E(t) = \left( \frac{1}{D_0 + D_1 t^n} \right) \left( \frac{1}{1 + \frac{n^2 \pi^2}{6}} \right) \quad (45)$$

At this point, with  $E(t)$  known, the relationship between uniaxial relaxation modulus and shear relaxation modulus can be used to determine  $G(t)$ . Although Poisson's ratio  $\nu$  is known to be somewhat time and temperature-dependent, it complicates the analysis and experiments too much for its own worth, and a constant  $\nu$  has been proven to be a reliable assumption.

The shear relaxation modulus from macroscopic oscillatory-mode dynamic shear rheometer (DSR) data is plotted and compared, when DSR data is available, to the predicted shear relaxation modulus from GPL results through nanoindentation. DSR testing assumes a constant sample geometry (no cracking) during torque application, one of the basic principles

behind its operation. The assumption in DSR testing is that changes in torque arise only from changes in sample radius and that  $|G^*|$  is an undamaged complex modulus. In DSR testing, a pure shear stress leads to a shear strain.

### 5.5.2 Formulation for Interconversion to $|E^*|$ Mastercurve

The final step in creep analysis is determining the uniaxial  $|E^*|$  dynamic modulus mastercurve, using the fitted GPL parameters as inputs. Time alone cannot be used to judge the stiffness of materials. One must look at more comprehensive rheological data through interconversion between time and frequency. Interconversion is necessary because nanoindentation tests are performed in the time domain, whereas complex modulus mastercurves are generally presented in the frequency domain. Frequency is commonly used as a convenient surrogate for temperature, although greater emphasis is placed on temperature considerations for the intrinsic understanding of material response.

One approximation that can be made to convert between time and frequency is [13]

$$t = \frac{0.08}{f} \quad (46)$$

This relationship is an updated form of the common approximation that originates from the relationship between the relaxation modulus and the real part of the complex modulus as defined by Christensen [9].

The dynamic modulus is predicted from the creep compliance using the GPL parameters of Equation (33) as model inputs [13], [37]. The dynamic modulus can be calculated as

$$|E^*| = \frac{1}{|D^*|} \quad (47)$$

The complex compliance is defined as

$$D^* = D' - iD'' \quad (48)$$

where  $D'$  is the storage (elastic) modulus and  $D''$  is the loss modulus. This can be expressed as

$$|D^*| = \sqrt{((D')^2 + (D'')^2)} \quad (49)$$

It can be shown, through the theory of linear viscoelasticity, that

$$D^* = s\mathcal{L}\{D(t)\}|_{s=i\omega} \quad (50)$$

where  $\mathcal{L}\{D(t)\}$  is the Laplace transformation of  $D(t)$  and  $\omega$  is the angular frequency. Taking the Laplace transformation of the GPL form and substituting into Equation (50) yields the complex compliance as a function of angular frequency  $\omega$ :

$$D^* = D_0 + D_1\Gamma(n+1) \left[ \cos\left(\frac{n\pi}{2}\right) - i \sin\left(\frac{n\pi}{2}\right) \omega^{-n} \right] \quad (51)$$

Hence,

$$D' = D_0 + D_1\Gamma(n+1)(2\pi f)^{-n} \cos\left(\frac{n\pi}{2}\right) \quad (52)$$

$$D'' = D_1\Gamma(n+1)(2\pi f)^{-n} \sin\left(\frac{n\pi}{2}\right) \quad (53)$$

Physically,  $D_1$  represents a uniform shift (translation) of the  $|E^*|$  curve.  $D_0$  only affects the initial, transient portion of the functional form.

## 5.6 Analytic Formulation for Cohesion

While creep responses are important to ensure that adverse phenomena such as rutting are limited, another crucial aspect of asphalt binder and mastic research is surface energy and work of cohesion, which will improve our understanding of reinforcement mechanisms in mastic. Research in cohesion can also help motivate and inform research in adhesion, a more useful quantity for asphalt researchers in determining the propensity of binders and mastics to debond from aggregate surfaces in the presence of water, based on surface energy components.

In a theoretical adhesive indentation model proposed by Sirghi et al., the effects of adhesive and elastic forces are considered and coupled [67], [68]. Over the contact area between the tip and sample surface, adhesive forces depend on attraction and geometry between the tip and sample, while elastic forces depend on the strain fields in the sample imposed by the tip. If a thin film of the adhesive sample remains on the tip after unloading, the model can be used to assess ductile cohesion in the sample rather than brittle adhesion between the tip and the sample. Assessment of elasticity is based on Sneddon's solution for the elastic deformation of a homogenous sample half-space by a rigid axisymmetric indenter [69]. Then, the externally applied contact force for binder and mastic is determined mainly by elastic and adhesive forces. Although the adhesive force can affect both the loading and unloading parts of the indentation process, only the unloading segment, for decreasing contact areas, allows for a direct measurement of the adhesive force. Since the loading rate is set so high and there is practically no hold time, the influence of creep in adhesion testing is assumed to be negligible.

The primary assumptions of the theoretical model are that Sneddon's solution for the deformation of the sample surface outside the contact area is not considerably affected by adhesion, the adhesion energy and contact area are assumed to be continuous functions during the indentation, the tip and sample surfaces have high smoothness, superposition is valid so that the elastic and adhesive forces can be summed into an external loading force applied to the indenter during the unloading process, and that the elastic and adhesive forces

are independent of one another. These assumptions allow the elastic and adhesive forces to be decoupled, which is necessary since only the adhesive force contributes to the analytical formulation for work of cohesion.

The elastic force and elastic stiffness of the indenter-sample contact are only important to determine the modulus of elasticity, which is not a goal of this cohesion protocol. For asphalt materials, it is expected that viscoelastic forces are sensed, rather than purely elastic forces. Whether a pure elastic or viscoelastic force contributes to Sirghi and Rossi's model bears no influence on the relationship between pull-off force and contact depth from which work of adhesion is determined. The elastic or viscoelastic force description simply modifies the net external loading force applied to the indenter during the unloading process. The elastic or viscoelastic force would add a quadratic term to the dependency between external indenter load and indentation depth [68]. The model's initial, non-generalized dependency is for an adhesion-free interface where the net external load equilibrates solely the elastic force. When indenter-sample adhesion is not negligible (such as the case in testing asphalt binder or mastic), a term describing the adhesive force variation during the unloading process is added to the external loading force.

When adhesion is generated by short-range interactions of a large number of molecules at the region of contact between the indenter and sample, the most suitable parameter is the work of adhesion. The nonlinear force-displacement dependence has a general form as follows [51]:

$$P(h) = a(h - h_f)^n \quad (54)$$

where  $h_f$  is the depth of the residual indenter imprint on the surface,  $h$  is the indentation depth, and  $a$  and  $n$  are curve-fitting parameters related to tip geometry. The parameter  $n = 2$  for a conical geometry. The dependency in Equation (54) is for an adhesion-free interface where the net external load equilibrates solely the elastic force. When indenter-sample adhesion is non-negligible, a term describing the adhesive force variation during the

unloading process is added to the right-hand side of Equation (54). For a conical indenter-sample contact geometry, the contact depth  $h_c$  determines the contact radius as

$$r_c = h_c \tan \alpha \quad (55)$$

for the cone angle  $\alpha$ . The net external loading force  $P(h)$  applied to the indenter during unloading is the sum of the elastic force  $F_e(h)$  and adhesive force  $F_a(h)$ :

$$P(h) = F_e(h) + F_a(h) \quad (56)$$

For our experiments and loading programs, the elastic force does not contribute to the interfacial energy at ductile failure. Ductile failure occurs at the maximum negative tensile pull-off load after an appreciable amount of inelastic necking, when the net external loading force is equilibrated solely by the adhesive force. To determine the adhesive force, the adhesion energy at the indenter-sample interface is

$$W_a = -\gamma_a A_c \quad (57)$$

where  $\gamma_a$  is the thermodynamic work of adhesion and  $A_c$  is the indenter-sample contact area. For a conical geometry,  $A_c$  is determined as

$$A_c = \frac{\pi \tan \alpha}{\cos \alpha} h_c^2 \quad (58)$$

for cone angle  $\alpha$  and contact depth  $h_c$ . The contact adhesion energy is determined as

$$W_a = \frac{-4\gamma_a \tan \alpha}{\pi \cos \alpha} h^2 \quad (59)$$

where the change from contact depth  $h_c$  to total indentation depth  $h$  is based on a conversion related to the conical indenter-sample contact geometry and the assumption that the sample

surface outside the contact area is not considerably affected by adhesion. The relationship between  $h_c$  and  $h$  is

$$h_c = (1 - \varepsilon)h \quad (60)$$

and the geometric constant  $\varepsilon$  is derived as  $\varepsilon = 1 - 2/\pi$  for a conical tip. The adhesive pull-off force (the derivative of adhesion energy) is

$$F_a = -\frac{8\gamma_a \tan \alpha}{\pi \cos \alpha} (h - h_f) \quad (61)$$

when a residual imprint  $h_f$  is included in the expression for the greatest generalization. Since there is no long-term residual imprint or plasticity,  $h_f = 0$  and Equation (61) becomes

$$F_a = -\frac{8\gamma_a \tan \alpha}{\pi \cos \alpha} h \quad (62)$$

Solving Equation (62) for thermodynamic work of adhesion gives

$$\gamma_a = -\frac{\pi F_a \cos \alpha}{8h \tan \alpha} \quad (63)$$

The entire formulation above, originally developed for adhesion, applies to cohesion testing when the tip is coated with a thin film of binder after the test. The tensile pull-off cohesive force and maximum penetration depth can both be obtained directly from indentation data and applied to Equation (63), which is an advantage over AFM-based methods, where cantilever spring constants are required for force-distance curves. The maximum penetration depth corresponds to the maximum area of contact between the indenter tip and sample surface, and it is assumed that because of adhesion between binder and tip, this contact area is maintained during unloading and retraction.

## CHAPTER 6. VISCOELASTIC RESULTS<sup>1</sup>

### 6.1 Sample Creep Data

With the analytic formulations established, we can now present the results of various forms of data relevant to creep testing. Figure 10 shows three types of trends in preliminary testing, with one parameter changed sequentially in each case and all other parameters remaining unchanged. These preliminary tests, confirming intuitive trends, reaffirm confidence in the capabilities of the equipment.

### 6.2 Results of Initial Trials: Creep Compliance Data Analysis

Figure 11 is a comparison of experimental data (initial trials) to GPL model predictions based on Equations (32), (33), and (34) for three representative indentation tests. Plots are shown for  $h_c$  vs.  $t$  and  $h_c^2$  vs.  $t$ . Based on the constitutive relationship between penetration depth and creep compliance for the indenter tip geometry, the a priori creep representation is fit into experimentally measured load-displacement curve data using nonlinear least squares regression in customized MATLAB code.

---

<sup>1</sup> The results of Sections 6.1, 6.2, and 6.3 have been published by the author of this dissertation in: Veytskin, Y., Bobko, C.P., and Castorena, C. (2014). Nanoindentation investigation of asphalt binder and mastic viscoelasticity. *International Journal of Pavement Engineering* ahead-of-print, 1-14.

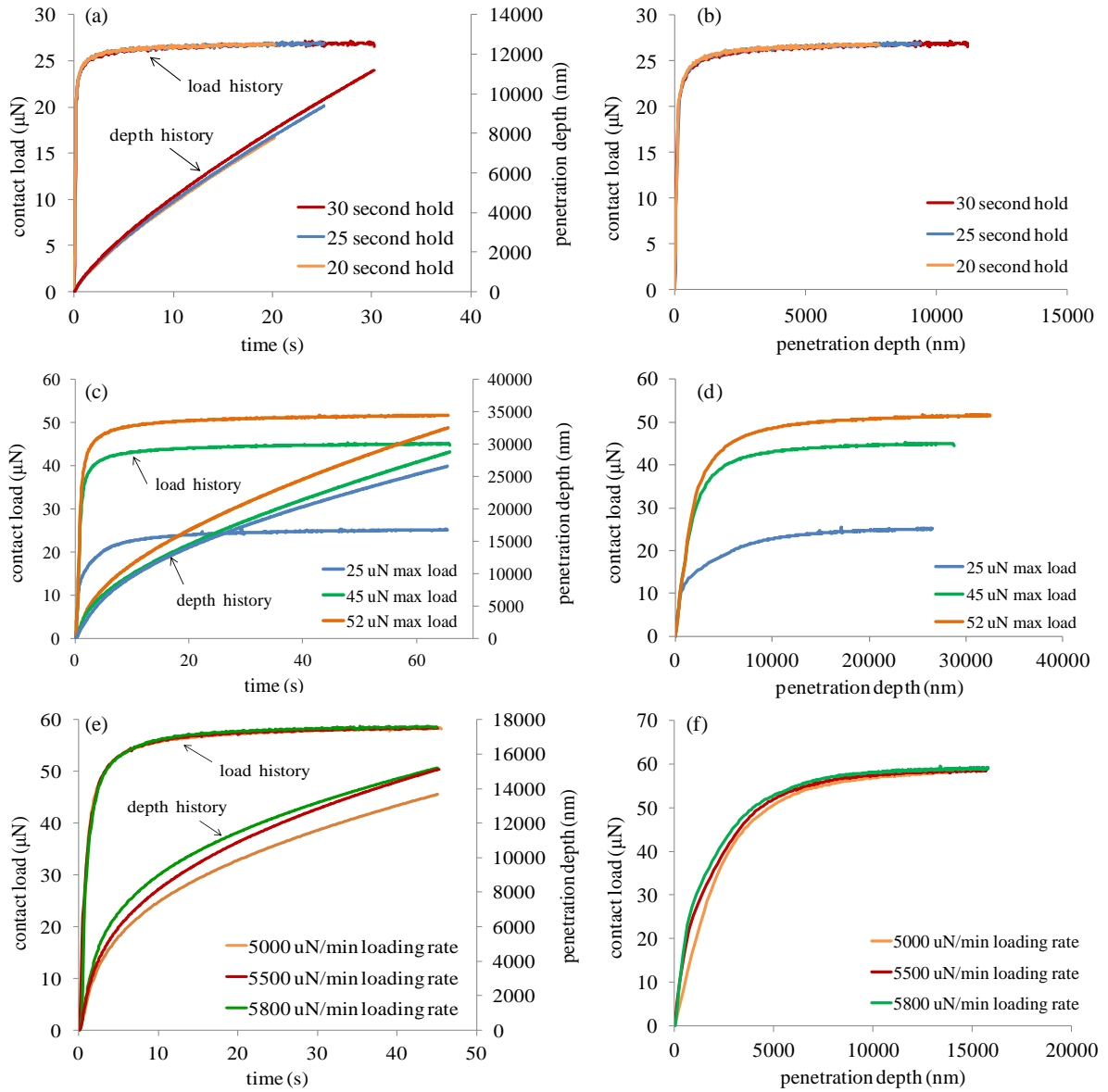


Figure 10: Sample creep data: (a) 17000  $\mu\text{N}/\text{min}$  loading rate, 27  $\mu\text{N}$  max load; (b) Ramp-and-hold curve for (a); (c) 5000  $\mu\text{N}/\text{min}$  loading rate, 65 s hold time; (d) Ramp-and-hold curve for (c); (e) 59  $\mu\text{N}$  max load, 45 s hold time; (f) Ramp-and-hold curve for (e)

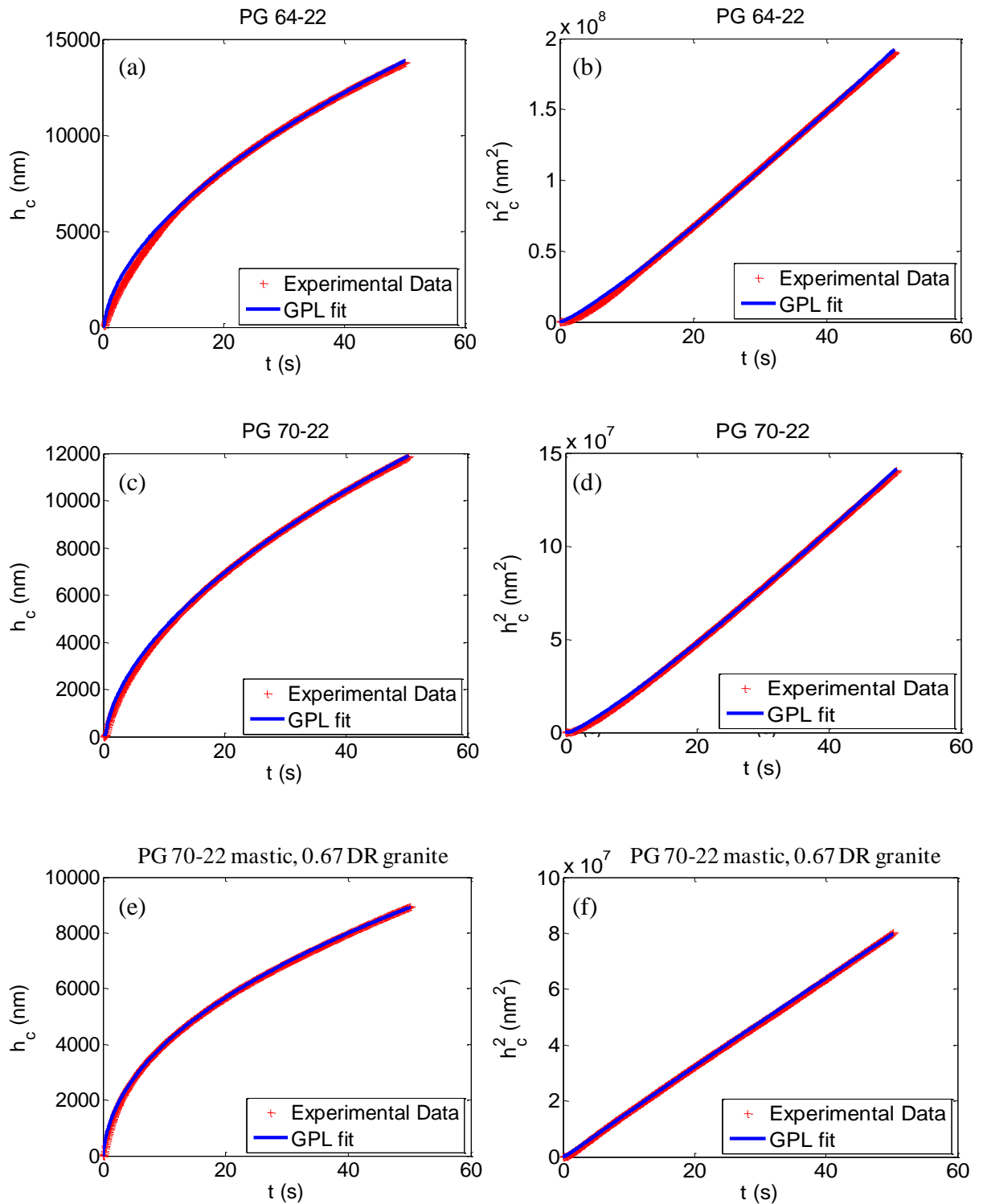


Figure 11:  $h_c$  vs.  $t$  and  $h_c(t)^2$  vs.  $t$  for PG 64-22 binder (a and b), PG 70-22 binder (b and c), and PG 70-22 mastic, 0.67 DR (e and f) for initial trials

For the creep tests, either the loading rate, hold time, or maximum load was changed. In accordance with the fit-and-predict scheme, when one input parameter was changed, the others were kept constant, *ceteris paribus*, to rule out the possibility of other factors overriding trends. Figure 11 uses the same loading program for each test. Based on Figure 11, one can see the “long-term” steady-state strain rate behavior. Because the governing constitutive equation (Equation (31)) for conical viscoelastic indentation relates  $h_c(t)^2$  to  $J(t)$ ,  $h_c(t)^2$  is plotted over time.

From Figure 11, one can see that the GPL fits the strain rate behavior extremely well, with  $R^2$  values calculated around 0.98. Since there is equal time spacing for data collection in the software throughout the entire experiment, there is no weighing of data in any specific time interval, and the results are reliable and replicable. In general, the GPL may not be able to account for sudden changes in strain response, rendering the Prony series more suitable locally. However, that situation is not a concern here due to broadband data smoothness.

Physically, the “stress exponent”  $n$  from the GPL represents the time-dependency of the unit response function, or the sensitivity of the unit response function to changes in frequency or temperature [23]. It can be defined as

$$n = \left| \frac{d \log R_H(t)}{d \log t} \right| \quad (64)$$

where  $R_H(t)$  is the unit response function. An alternative definition is

$$n = \frac{\log G'(\omega_i) - \log G'(\omega_{i-1})}{\log \omega_i - \log \omega_{i-1}} \quad (65)$$

where  $G'(\omega) = |G^*(\omega)| \times \cos \delta$ , where  $\delta$  is the phase angle,  $\omega$  is an angular frequency, and  $G'$  is a storage modulus in shear. Since  $n$  represents time-dependency of the unit response

function, the extreme case of  $n = 0$  corresponds to a time-independent material idealized as perfectly linear elastic with no creeping.

The long-term steady-state “equilibrium” strain-rate behavior of binder and mastic can be expected since, initially, it has been shown that transient creep can be attributed mainly to viscous flow [23]. Huang et al. simulated the transient creep with a Burgers model. The primary, transient creep is dominated by viscoelastic deformation, and the steady-state, secondary creep is dominated by power-law creep deformation [23]. Although the stress in the sample below the indenter tip in the transient stage is large, the power-law creep deformation is initially small because power-law creep needs time to build up. The transient creep also accounts for the effects of any tip residue from previous indents and for ambiguities in the contact point. Once contact has been made, the indenter tip initially has a fast strain rate that gradually decreases as the tip encounters an increasing volume of viscoelastic material along the conical surface area of the diamond tip. It was determined that even with significantly longer hold times, the strain rate stabilizes to a constant relatively early on in the creep experiment. The stresses within the contact zone are expected to be initially large and decrease monotonically over time. As previously mentioned, data for longer hold times is not analyzed due to numerous complications, including less propensity to remain within the LVE regime.

It has been shown that the steady-state strain rate of conventional tensile creep satisfies the power law [20]. Huang et al. showed that the viscoelastic deformation at steady-state creep is much smaller than the power-law creep deformation. Since we are only interested in steady-state creep, this provides another argument for using the GPL.

## **6.3 Results of Interconversions of Creep Compliance**

### **6.3.1 Interconversion to Shear Relaxation Modulus**

With creep compliance successfully modeled with the GPL, we can use Denby’s form of interconversion from Section 5.5.1 (Equation (42)) to plot shear relaxation modulus values.

The values are not considered a full mastercurve due to the limited time range of testing, but the nanoindentation values can still be compared with a true mastercurve from the DSR method.

With the DSR data converted to shear relaxation modulus, the predicted  $G(t)$  values from the GPL results are plotted and compared to the DSR data in Figure 12 [80]. The DSR data uses the collocation method to fit a Prony series model (the Wiechert model, as a generalized Maxwell model) in the relaxation domain to the frequency sweep results. With the uniaxial relaxation modulus  $E(t)$  results from the collocation method, this is translated to  $G(t)$  by assuming a Poisson's ratio of  $\nu = 0.5$  for incompressibility. The GPL results are only valid for a very narrow time range, between 0.1 and 100 seconds as shown in Figure 12, corresponding to 20-23 °C and encompassing the average creep hold times of 70 seconds. A single, unique GPL modeling result must be applied to all times of the shear relaxation modulus, so even with access to additional temperatures, an alternative model such as a Prony series should eventually be considered for higher accuracy across a wider temperature range.

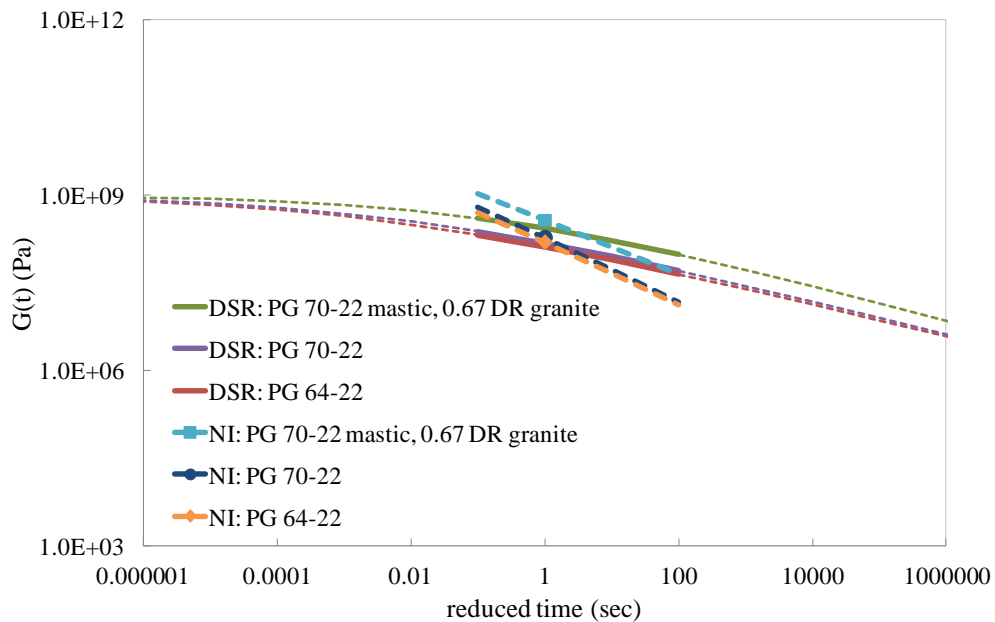


Figure 12: Shear relaxation modulus (initial trials)

Each method's results are mechanically consistent with one another in terms of rank ordering of shear modulus. Within the range of interest, PG 70-22 mastic has the highest shear relaxation modulus and PG 64-22 has the lowest, for both methods. Farther to the right on the relaxation mastercurve, the loading frequencies decrease for longer times as the binder and mastic approach more viscous, Newtonian regions. Around room temperature, the nanoindentation results accurately predict the DSR results for relaxation modulus.

### 6.3.2 Interconversion to $|E^*|$ Mastercurve

The procedure from Section 5.5.2 can now be implemented to determine the uniaxial  $|E^*|$  dynamic modulus mastercurve, using the fitted GPL parameters as inputs. For the prescribed time range of the shear relaxation modulus data of Figure 12,  $0.1 < t < 100$  seconds, this would correspond to a frequency range of  $0.0008 < f < 0.8$  Hz based on Equation (46). In Figure 13, the dynamic modulus is predicted from the creep compliance using the GPL parameters of Equation (33) as model inputs [13], [37]. In Figure 13 of these initial tests, only the dynamic modulus values corresponding to the calculated frequency range are shown.

Based on Figure 13, fundamental internal trends and  $|E^*|$  values are as expected within the prescribed frequency range, with PG 70-22 mastic having the highest  $|E^*|$  and PG 64-22 binder having the lowest  $|E^*|$ . Trends and values are also consistent with expectations and predictions from Figure 14, which shows  $|E^*|$  for the binders and mastics from DSR testing. The initial trials show a close correspondence between nanoindentation and DSR results.

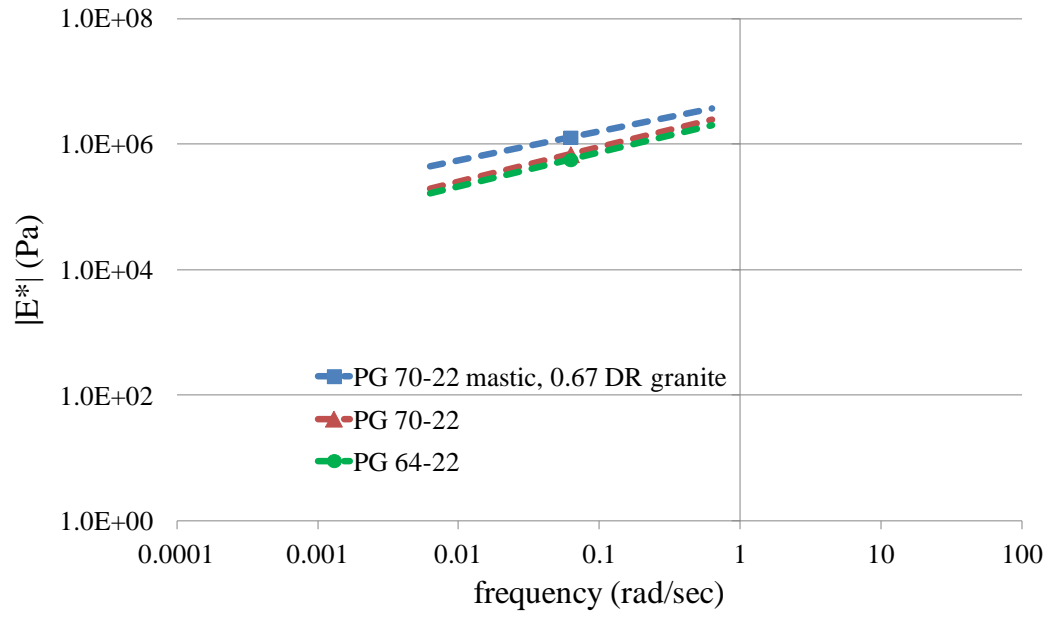


Figure 13:  $|E^*|$  / mastercurve from nanoindentation (initial trials)

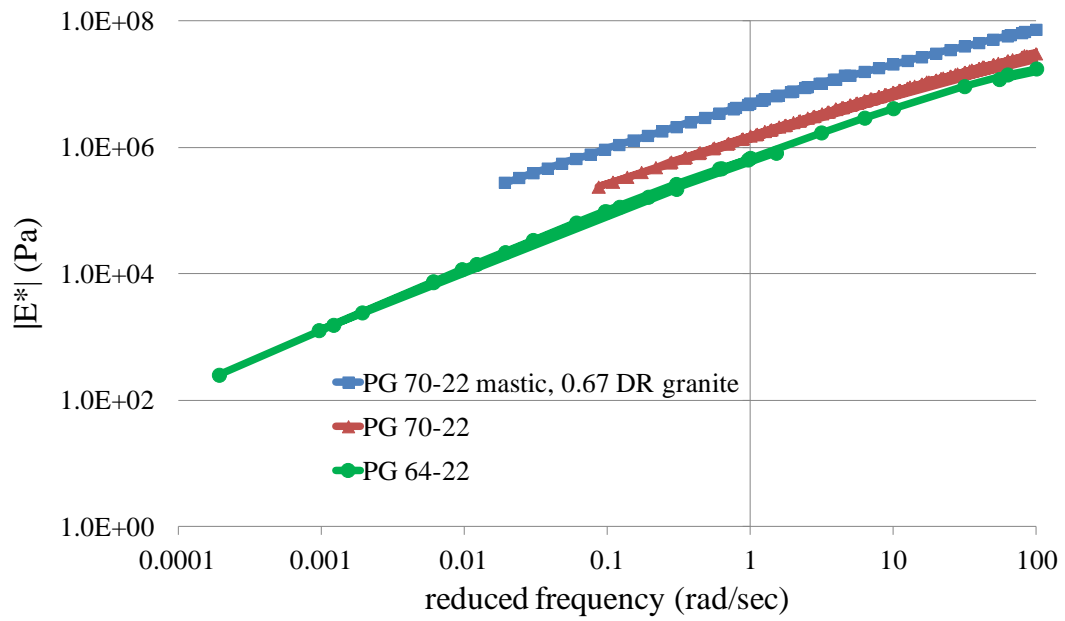


Figure 14:  $|E^*|$  / mastercurve from DSR (initial trials)

### 6.3.3 Potential Sources of Error

With the results of Sections 6.3.1 and 6.3.2, the foundation of nanoindentation as a promising proof of concept has been established; however, there are still a few sources of error worth mentioning. Typically, the initial portion of a creep test is not very reliable for time-temperature superposition. The fast ramping of these creep tests, to reach the hold time more quickly, helps address that concern. Higher hold times with an indenter tip can also cause introduction of nonlinear viscoelasticity, instrumental drift, and instrumental stability issues. Given the experimental limitations and creep hold times chosen in nanoindentation literature, the creep hold times chosen for this research are the best compromise to be able to still investigate steady-state effects.

The experimental and analytical aspects may not conform to the assumptions of traditional creep test analysis for constant stress states. The simplicity of the GPL compared to the actual contact situation and assumptions regarding stress and strain-rate could be leading to various manifestations through the GPL. Regardless, these results provide the proof of concept for using nanoindentation to supplement traditional macroscale DSR testing. While it is possible to test over a wide temperature range with a nanoindenter, it is first necessary to confirm expected trends in a narrower, more accessible temperature range before adding further complexity and experimental complications to the research. These preliminary results are sensible given that time snapshots of materials with time memories are being captured.

## 6.4 Results of RTFO-Aged Materials: Creep Compliance Data Analysis<sup>2</sup>

### 6.4.1 Extraction of Fitted Parameters

With initial trials completed, the final stage of the creep research was a comprehensive analysis of RTFO-aged materials, which are more representative of the types of materials encountered in the field. Aging is the single most important factor influencing field performance. The analysis routine developed by Veytskin et al. [80], from the initial tests, is applied to extract fitted parameters of the creep compliance model, based on the GPL, for each material from Table 1 [79]. These routines are used for ultimately determining the shear relaxation and dynamic modulus values at a specific frequency. Representative fitting results from the routines are shown in Figure 15 on the three types of binders. The fitted parameter results are listed in Table 3.

---

<sup>2</sup> The results of Section 6.4, Chapter 8, and Chapter 9 have been published by the author of this dissertation in: Veytskin, Y., Bobko, C.P., and Castorena, C. (2015, under review). Nanoindentation and atomic force microscopy investigations of asphalt binder and mastic cohesion. *Journal of Materials in Civil Engineering (ASCE)*.

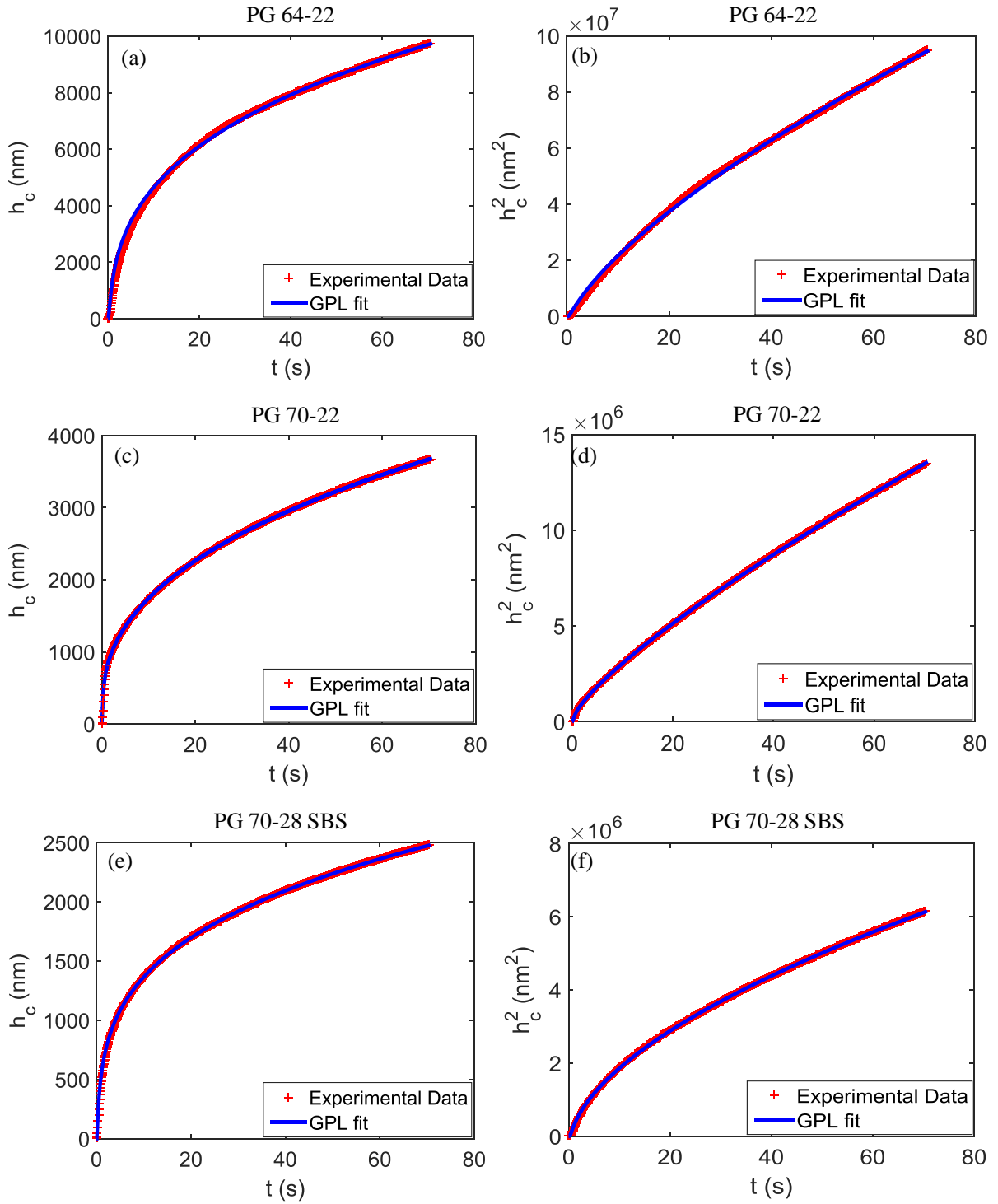


Figure 15:  $h_c$  vs.  $t$  and  $h_c(t)^2$  vs.  $t$  for PG 64-22 (a and b), PG 70-22 (b and c), and PG 70-28 SBS (e and f)

Table 3: Fitted creep compliance parameters for RTFO-aged materials

<b>Material</b>	Number of creep tests (room temperature)	$D_0$ (GPa) <sup>-1</sup>	$D_1$ (GPa) <sup>-1</sup>	$n$
PG 70-28 SBS	19	0	5.03	0.89
PG 70-22	25	0	7.12	0.84
PG 64-22	21	0	14.04	0.85
<b>lime filler</b>				
PG 70-28 SBS, 0.6 DR	25	0	1.75	0.72
PG 70-28 SBS, 0.8 DR	25	0	1.37	0.66
PG 70-28 SBS, 1.0 DR	23	0	1.05	0.63
PG 70-28 SBS, 1.29 DR	17	0	0.51	0.55
PG 70-22, 0.6 DR	25	0	2.87	0.7
PG 70-22, 0.8 DR	24	0	1.64	0.67
PG 70-22, 1.0 DR	24	0	1.44	0.62
PG 70-22, 1.26 DR	16	0	0.63	0.61
PG 64-22, 0.6 DR	25	0	4.03	0.76
PG 64-22, 0.8 DR	25	0	2.92	0.7
PG 64-22, 1.0 DR	23	0	2.26	0.67
PG 64-22, 1.2 DR	22	0	1.11	0.65
<b>granite filler</b>				
	Number of creep tests (room temperature)			
PG 70-28 SBS, 0.6 DR	23	0	2.48	0.7
PG 70-28 SBS, 0.8 DR	25	0	1.66	0.63
PG 70-28 SBS, 1.0 DR	20	0	1.14	0.58
PG 70-28 SBS, 1.2 DR	15	0	0.51	0.55
PG 70-22, 0.6 DR	17	0	3.14	0.77
PG 70-22, 0.8 DR	19	0	2.41	0.69
PG 70-22, 1.0 DR	18	0	1.89	0.63
PG 70-22, 1.2 DR	21	0	0.75	0.57
PG 64-22, 0.6 DR	25	0	4.56	0.75
PG 64-22, 0.8 DR	25	0	3.04	0.65
PG 64-22, 1.0 DR	22	0	2.50	0.62
PG 64-22, 1.2 DR	18	0	1.02	0.61

## 6.4.2 Linearity Check

To confirm that the creep compliance is determined within the range of linear viscoelasticity, we can plot creep compliance over the range of loads used to indicate load-independence of creep compliance [79]. Figure 16(a) plots the creep compliance values for PG 70-22 at  $t = 70$  sec. for the five maximum load variations from the creep loading programs, and Figure 16(b) plots the creep compliance function (using the fitted GPL parameters) to 100 sec., showing a near overlap for the five maximum loads. The same procedure was conducted for PG 70-28 SBS in (c) and (d).

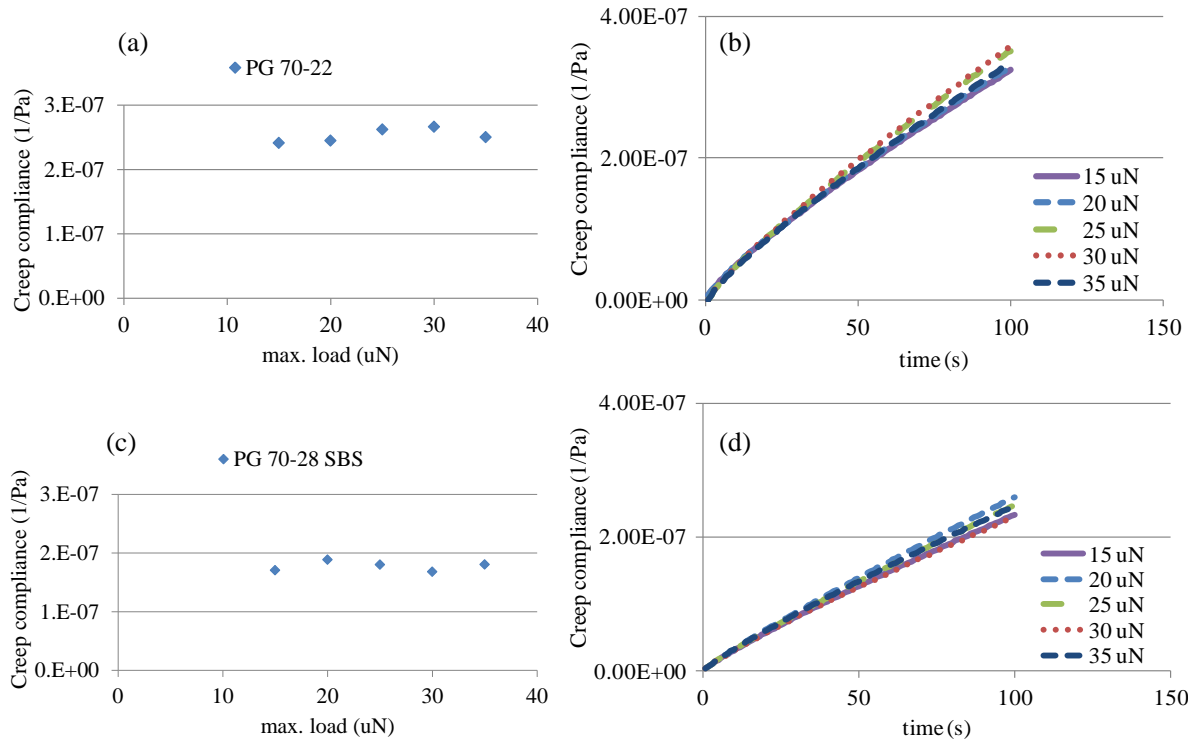


Figure 16: Creep compliance vs. maximum load (5000  $\mu\text{N/s}$  loading rate, 70 sec. hold time) for (a) PG 70-22 and (c) PG 70-28 SBS; (b) Creep compliance function vs. time for (a) to 100 sec. using fitted GPL parameters; (d) Creep compliance function vs. time for (c) to 100 sec. using fitted GPL parameters

Figure 17 uses the same procedure to verify linearity for two more representative materials: PG 70-22 mastic at 1.26 DR (lime) and PG 70-28 SBS mastic at 1.29 DR (lime). Figure 18 repeats the procedure for PG 70-22 mastic at 1.2 DR (granite) and PG 70-28 SBS mastic at 1.2 DR (granite).

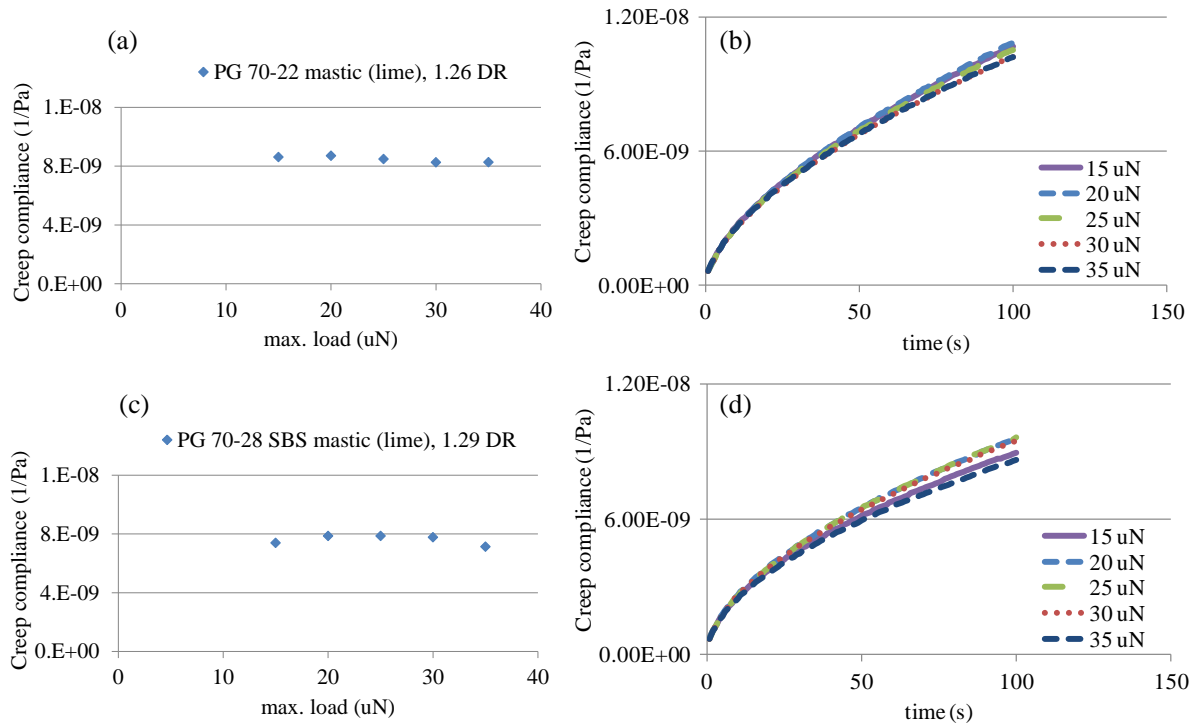


Figure 17: Creep compliance vs. maximum load (5000  $\mu\text{N/s}$  loading rate, 70 sec. hold time) for (a) PG 70-22 mastic, 1.26 DR (lime) and (c) PG 70-28 SBS mastic, 1.29 DR (lime); (b) Creep compliance function vs. time for (a) to 100 sec. using fitted GPL parameters; (d) Creep compliance function vs. time for (c) to 100 sec. using fitted GPL parameters

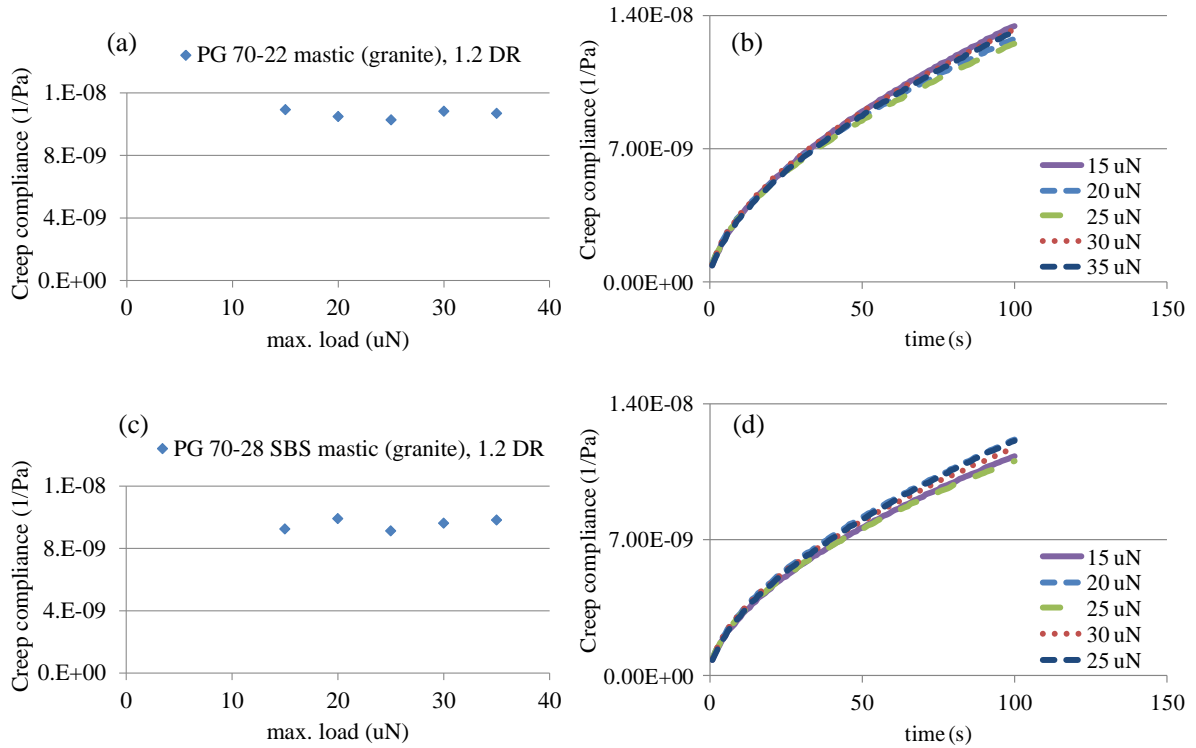


Figure 18: Creep compliance vs. maximum load (5000  $\mu\text{N/s}$  loading rate, 70 sec. hold time) for (a) PG 70-22 mastic, 1.20 DR (granite) and (c) PG 70-28 SBS mastic, 1.20 DR (granite); (b) Creep compliance function vs. time for (a) to 100 sec. using fitted GPL parameters; (d) Creep compliance function vs. time for (c) to 100 sec. using fitted GPL parameters

### 6.4.3 Comparisons of Creep Compliance and Dynamic Modulus Results

In addition to verifying linear viscoelasticity, the creep compliance curves can be used comparatively to confirm expected trends. In Figure 16, PG 70-22 creep compliance values are significantly higher than those of PG 70-28 SBS, as expected mechanically since SBS is known to stiffen asphalt. In Figure 17, PG 70-22 lime mastic creeps marginally higher than PG 70-28 SBS lime mastic. The same trend is observed in Figure 18 for granite mastics, and the creep compliance values for granite mastics are higher than those of the lime mastics in Figure 17, as expected. In all cases, the binders creep significantly higher than the mastics, an expected trend, by over an order of magnitude.

Figure 19 validates nanoindentation results by comparing interconverted data points from nanoindentation to oscillatory DSR results for dynamic modulus  $|E^*|$  for binders as well as lime mastics with the highest dust ratio. The hope in future research is to position these data points on a true dynamic modulus mastercurve. While values are shown in Figure 19 for nanoindentation results, ranges for these values are shown in Figure 20 to differentiate between trends in magnitudes and facilitate ease of comparison between lime and granite mastics. Figure 20 compares  $|E^*|$  results for lime and granite mastics using nanoindentation at intermediate dust ratios and for granite mastics at the highest dust ratio, showing an increase in  $|E^*|$  with increased filler volume concentration, as expected. Results for lime mastics at the highest dust ratio are included in Figure 19 when compared to DSR results. In Figure 20, the lime mastics'  $|E^*|$  values consistently exceed granite mastics for each dust ratio, as expected, since lime's increased specific surface area and porosity generally lead to greater stiffening than granite. The lime mastics with PG 70-28 SBS and PG 70-22 binder in Figure 19(a) nearly overlap each another. This is related to the marginal difference in creep compliance trends for lime mastics in Figure 17(b) and (d) with those same binders.

Overall, the trends of Figure 16, Figure 17, and Figure 18 for creep compliance agree mechanically with those of Figure 19 and Figure 20 for dynamic modulus across a range of filler volume concentrations. In addition, these results confirm expectations that nanoindentation tests are conducted with sufficient tip size and indentation depths to probe bulk mastic properties.

Shear relaxation modulus  $G(t)$  results are also reported. Figure 21 compares nanoindentation to DSR results for  $G(t)$  for binders as well as mastics with the highest dust ratio. Figure 22 compares  $G(t)$  results for lime and granite mastics using nanoindentation at intermediate dust ratios and for granite mastics at the highest dust ratio, showing an increase in  $G(t)$  with increased filler volume concentration, as expected. Results for lime mastics at the highest dust ratio are included in Figure 21 when compared to DSR results.

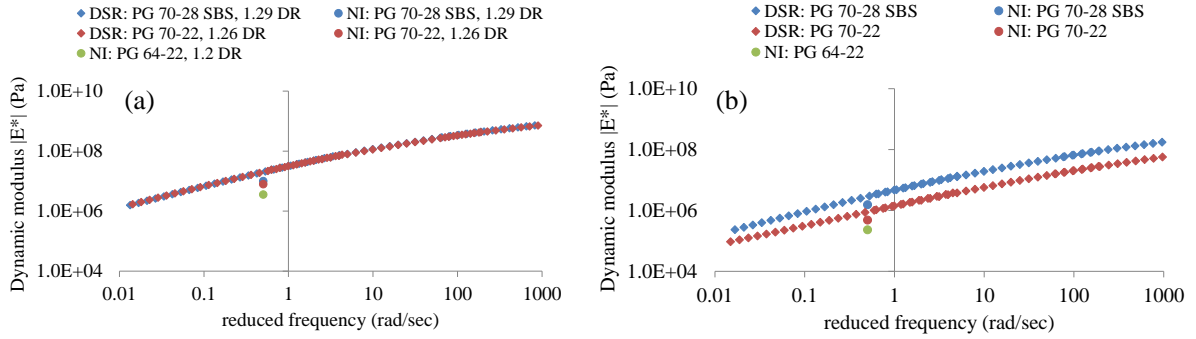


Figure 19: Dynamic modulus comparisons between nanoindentation and DSR for (a) highest dust ratios of PG 70-22 and PG 70-28 SBS mastics and (b) PG 70-22 and PG 70-28 SBS binders

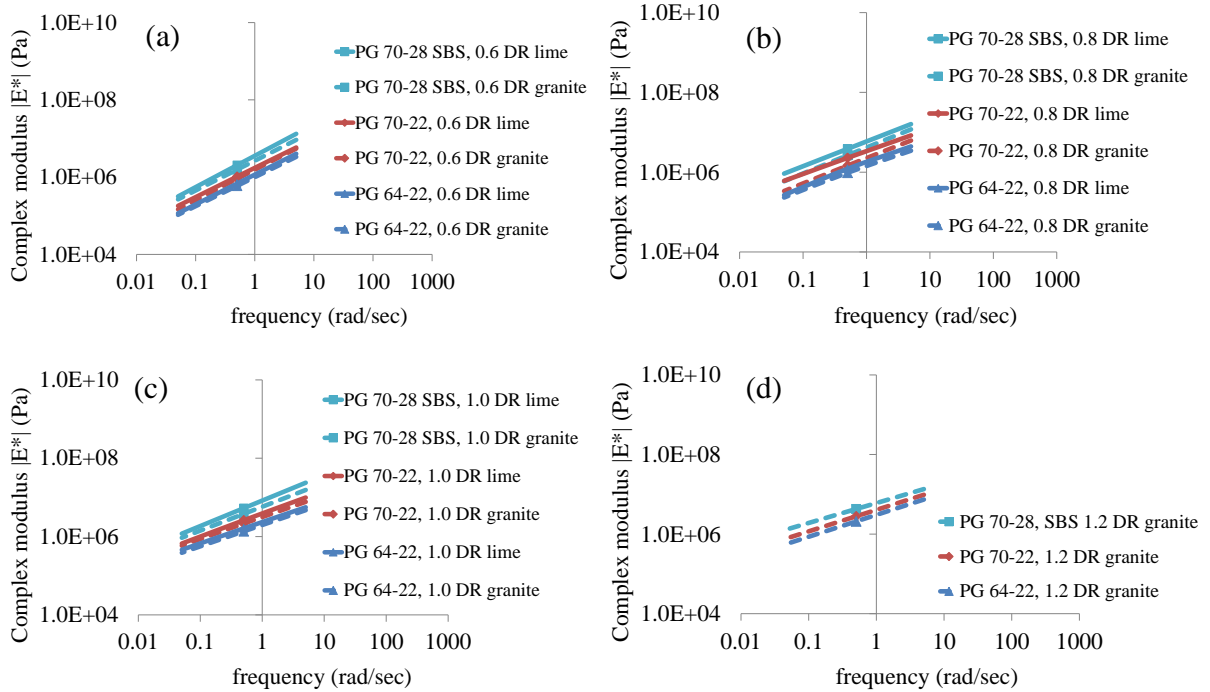


Figure 20: Nanoindentation results for dynamic modulus for PG 70-28 SBS, PG 70-22, and PG 64-22 mastics using lime and granite filler for (a) 0.6 DR; (b) 0.8 DR; and (c) 1.0 DR

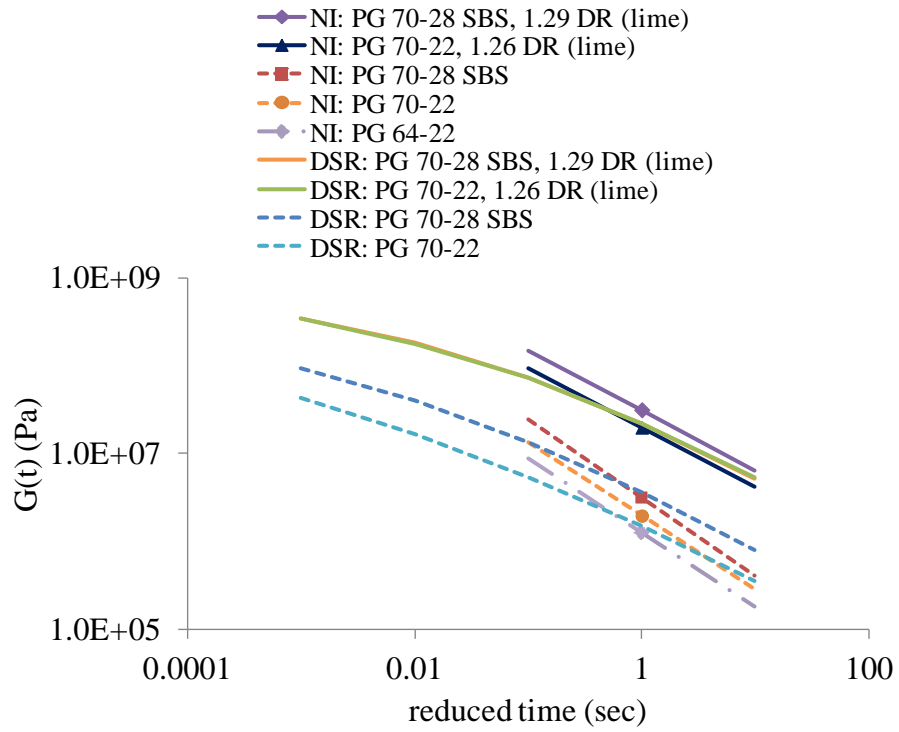


Figure 21: Shear relaxation modulus comparisons between nanoindentation and DSR for highest dust ratios of PG 70-22 and PG 70-28 SBS mastics and PG 70-22 and PG 70-28 SBS binders

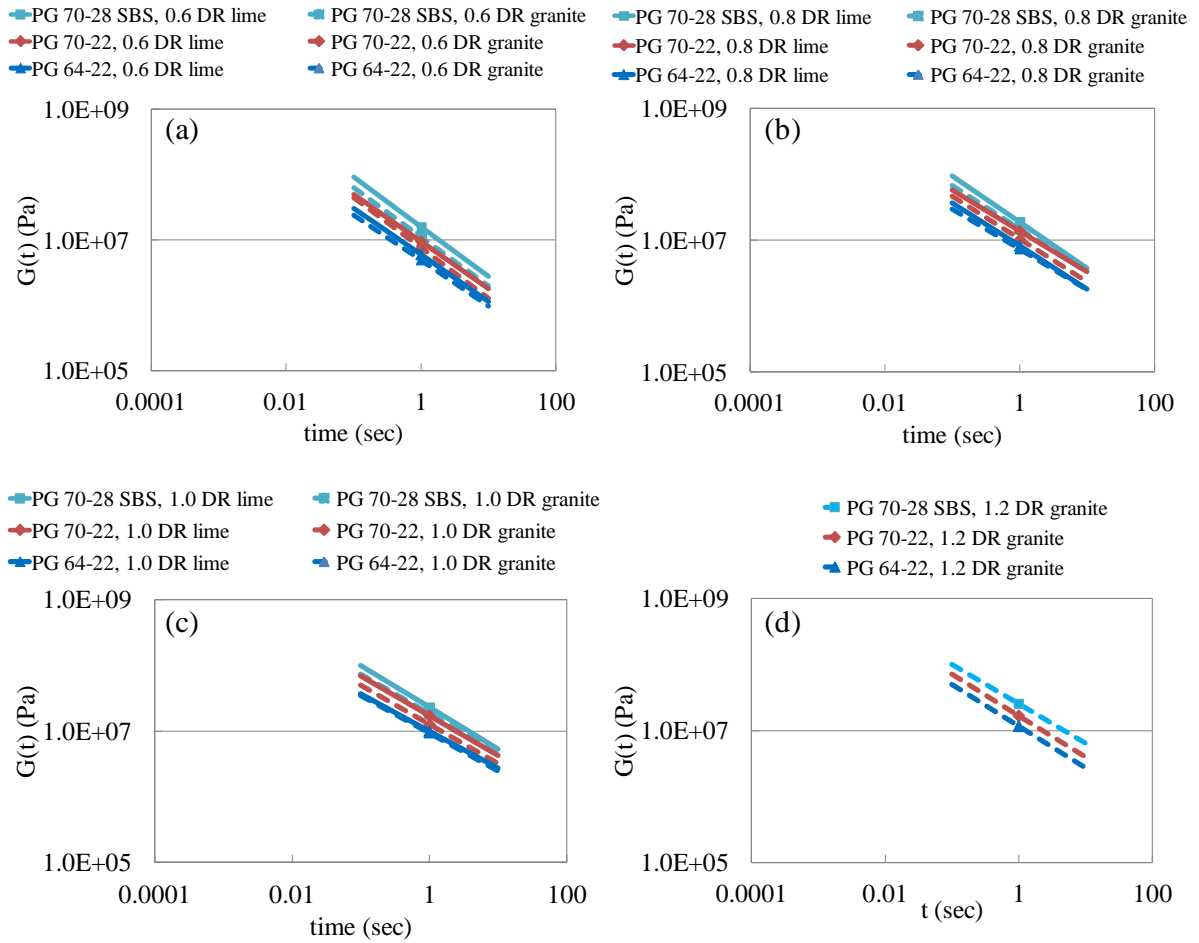


Figure 22: Nanoindentation results for shear relaxation modulus for PG 70-28 SBS, PG 70-22, and PG 64-22 mastics using lime and granite filler for (a) 0.6 DR; (b) 0.8 DR; (c) 1.0 DR; and (d) 1.2 DR

With all of the linear viscoelastic data compiled, it is useful to show snapshots in time and frequency of shear relaxation and dynamic modulus to isolate and more clearly interpret trends. Figure 23 shows trends at  $f = 0.08$  Hz (a and b) for dynamic modulus and at  $t = 1$  sec. (c and d) for relaxation modulus, respectively, showing an increasing trend in modulus with increasing dust ratio in all cases.

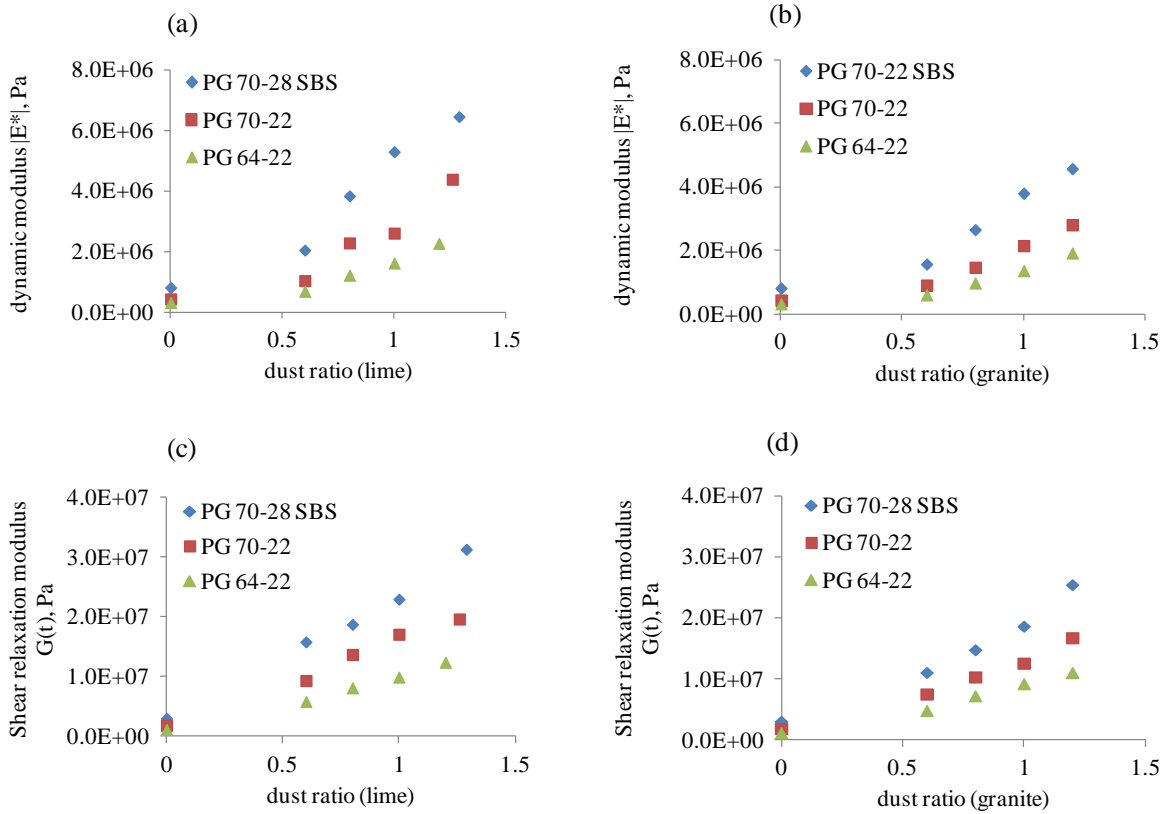


Figure 23: (a) dynamic modulus vs. dust ratio at 0.08 Hz; (b) dynamic modulus vs. dust ratio at 0.08 Hz; (c) relaxation modulus vs. dust ratio at  $t = 1$  sec.; (d) relaxation modulus vs. dust ratio at  $t = 1$  sec.

#### 6.4.4 Time-Scaling for Lower Temperature Tests

As previously mentioned, creep compliance cannot be directly determined because the stress constantly changes with increasing penetration depth in nanoindentation creep tests at constant load. Therefore, the only way to extract creep compliance is through an assumed model form, which prohibits application of time-temperature superposition as is conventionally done in viscoelastic characterization of materials. Given this limitation, as an alternative to assess the applicability of time-temperature superposition, time-temperature shift factors from DSR testing are used to scale time data at 17 °C to a reduced time corresponding to a reference temperature of 22 °C. Then, the GPL model parameters are re-

determined using the reduced time data and the same indentation curves, to verify that the GPL model still reflects the data at 22 °C by showing that the fitted GPL parameters remain approximately unchanged. Physically, since all of the DSR shift factors for a temperature of 17 °C, with 22 °C as the reference, are below 1, this lengthens the timescale of the data and implies that the same amount of creep occurs for two cases, when appropriately scaled: (1) a shorter time scale with a warmer temperature, and (2) a longer time scale with a cooler temperature. Table 4 lists the shift factors used for this analysis, from DSR testing.

Table 4: DSR results for shift factors

shift factors ( $\log a_T$ ) from DSR testing			
binders		mastics (lime)	
PG 70-28 SBS	PG 70-22	PG 70-28 SBS, 1.29 DR	PG 70-22, 1.26 DR
0.597	0.609	0.613	0.615

The expression to determine reduced time is defined as

$$t_R = \frac{t}{a_T} \quad (66)$$

where  $t_R$  is the reduced time,  $t$  is the adjacent time, and  $a_T$  is the shift factor. Table 5 shows the results of applying the established MATLAB routine to extract fitted parameters of creep compliance for the four RTFO-aged materials for which there are shift factors available from DSR testing, with the times scaled by the shift factor based on Equation (66). The results are compared to those of Table 3 for the corresponding materials. The same indentation curves are used in each case. The parameter  $D_I$  is excluded from the comparisons because it remained as practically zero in all cases. The results are a near overlap.

Table 5: Fitted creep compliance parameters for RTFO-aged materials using DSR shift factors (for the materials available from DSR testing)

Material	Number of creep tests (room temperature)	original times		reduced times		% difference ( $D_1$ )
		$D_1$ (GPa) <sup>-1</sup>	$n$	$D_1$ (GPa) <sup>-1</sup>	$n$	
PG 70-28 SBS	19	5.03	0.89	4.89	0.89	2.82
PG 70-22	25	7.12	0.84	7.04	0.84	1.13
<b>lime filler</b>						
PG 70-28 SBS, 1.29 DR	17	0.51	0.55	0.50	0.55	1.98
PG 70-22, 1.26 DR	16	0.63	0.61	0.62	0.61	1.60

Material	R <sup>2</sup> (original times)	R <sup>2</sup> (reduced times)
PG 70-28 SBS	0.97	0.99
PG 70-22	0.98	0.97
<b>lime filler</b>		
PG 70-28 SBS, 1.29 DR	0.98	0.97
PG 70-22, 1.26 DR	0.96	0.98

## CHAPTER 7. COHESION RESULTS<sup>3</sup>

With viscoelastic results presented and analyzed, cohesion results can now be introduced. Experiments, as performed in Veytskin et al. [81], use the newly developed cohesion-loading protocol. In efforts to carefully control experiments, a wide range of consistent dust ratios was selected for cohesion testing, ranging from 0.3 to 1.29. Identical nanoindentation grids were used for all samples, with a sufficiently large grid spacing (70  $\mu\text{m}$ ) to avoid residual stress fields and topographical interferences from previous indents. Carefully controlled experiments allow for experimental replicability and reproducibility, which are especially important given the complex behavior and contact geometry experienced by these materials.

A systematic effort was made to regulate the input parameters used between sample runs by setting up the same, repeatable grid for each sample. Within each grid, the primary loading parameters related to the cohesion experiment (maximum load, loading rate, and unloading rate) are varied to neutralize bias in input conditions. This allows for a more direct comparison of work of cohesion amongst all samples, without interferences from loading condition variations.

### 7.1 Fillers and Representative Cohesion Data

Presented in this section is a microstructural look at the available non-inert mineral and manufactured fillers along with the data collected in cohesion-protocol testing. Micrographs of commonly used mineral and manufactured fillers are shown in Figure 24.

---

<sup>3</sup> The results of Chapter 7 have been published by the author of this dissertation in: Veytskin, Y., Bobko, C.P., Castorena, C., and Kim, Y.R. (2015, under review). Nanoindentation investigation of asphalt binder and mastic cohesion. *Mechanics of Materials*.

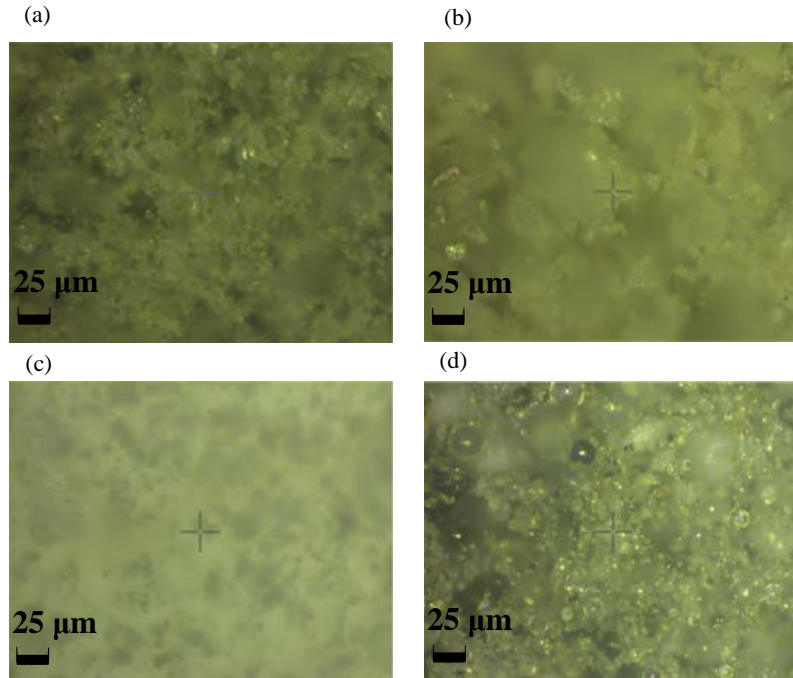


Figure 24: Micrographs of common fillers used in asphalt concrete: (a) cement dust; (b) baghouse fine granite; (c) hydrated lime; and (d) fly ash

Qualitatively, particle shape, size, and morphology can be examined in Figure 24. As shown, there are differences in texture, angularity, size, and shape amongst the four available fillers. Specific surface area (SSA) data was collected using a Quantachrome Monosorb single-point BET surface area analyzer. The results are shown in Table 6. Figure 24 shows that granite has the largest characteristic sizes and smoother surfaces, and accordingly, it has one of the lower SSAs. Hydrated lime is known to have a flaky particle shape with rough surface texture, and accordingly, it has the highest SSA by an order of magnitude. Hydrated lime has a finer filler gradation and more angularity to external surfaces than granite.

Table 6: Specific Surface Area

Filler Type	Specific Surface Area ( $m^2 / g$ )
Cement	2.240
Granite	1.557
Fly ash (Type F)	1.044
Hydrated lime	14.408

Mineral granite (Figure 24(b)) and manufactured hydrated lime (Figure 24(c)) are chosen as the two fillers for the mastics. Two common fillers with an order of magnitude SSA difference are selected to gain insight into variations in the reinforcement mechanism response for stiffening.

Representative nanoindentation curves for cohesion testing are shown in Figure 25. These representative curves are intended to avoid data cluttering by showing a general subset of the collected curves. In total, approximately 1400 successful cohesion-protocol indentation curves were collected. Figure 26 shows the parameters extracted from a cohesion-protocol curve.

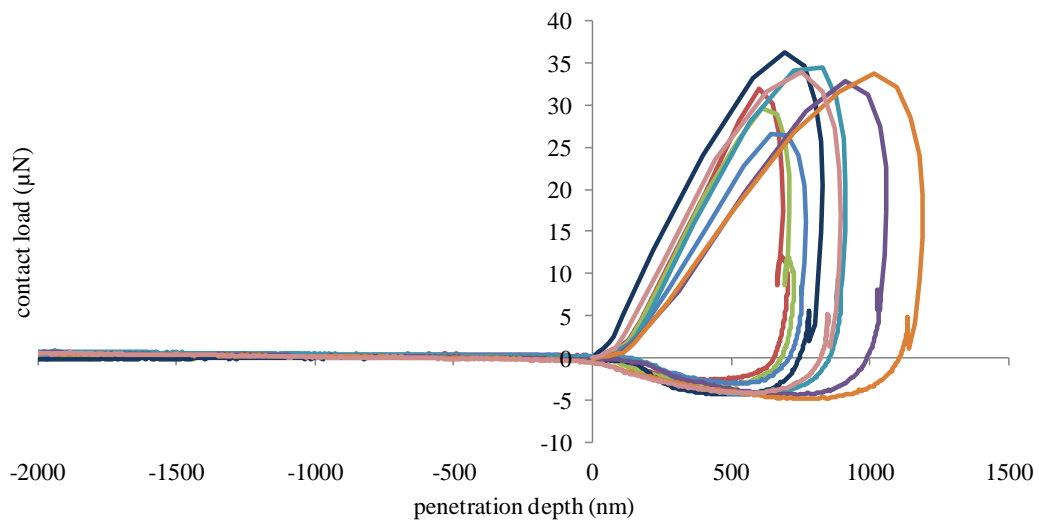


Figure 25: Representative cohesion-protocol nanoindentation curves

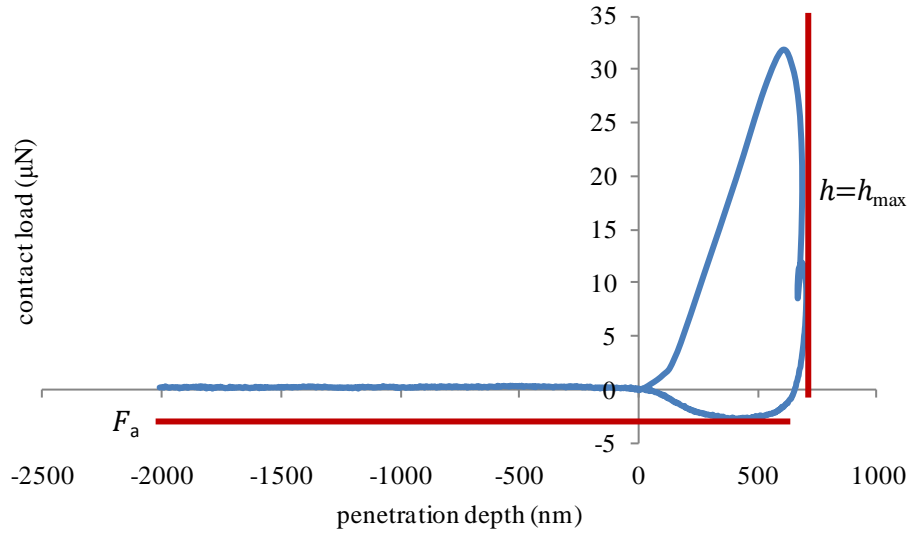


Figure 26: Parameters used in Equation (63) for a sample curve

## 7.2 Cohesion Results and Discussion

Evaluating Figure 25, the penetration depths become negative during the course of the unloading cycle, implying that the tip retracts above its original zeroed position that it held just prior to contact. The binder and mastic retract beyond the initial position held before failure occurs. If adhesive failure were occurring, the curves would “snap” back to zero at a specific displacement value, representing tip detachment from the sample and the disappearance of an interaction force. For the collected curves, there is a smooth, gradual transition back to zero. Although cohesive energy depends on the fracture mode, the exhibited behavior resembles a ductile failure with necking, with no evidence of a brittle jump to zero for which traditional interpretations of failure modes in linear elastic and nonlinear fracture mechanics would be most applicable. Further complicating a fracture-mode interpretation is the unique sphero-conical tip shape, which would tend to suggest a mixed-mode failure under most circumstances in brittle solids. Authors such as Xu and Needleman [83], Song et al. [70], and Ji et al. [27], [28] have all investigated modes of fracture associated with cohesive energies using specific methodologies and assumptions.

For this data, given the ductile behavior, without an apparent “snap” to zero, it can be concluded that failure is occurring cohesively (i.e., within the binder) rather than adhesively.

Binder residue on the indenter tip cannot be directly observed. However, tests on copper calibration samples immediately after asphalt indents showed an initial, transient pre-loading region associated with indentation depths around 20 nm before a true, steady loading phase on the copper. This residue film thickness is assumed to be negligible compared to indentation depths that are mostly in the range of 1 to 6  $\mu\text{m}$  for lime mastics and 1 to 11  $\mu\text{m}$  for granite mastics. Tip contamination within a series of tests, which is otherwise hard to identify from single-test material properties or system parameters, was addressed by plotting the sequence of work of cohesion values for all tests within a sample. No short- or long-term trends were observed in comparing work of cohesion values from the first, residue-free test to those of subsequent tests. Longer retract times well beyond 120 seconds were also implemented at an earlier stage of the research, and either similar trends as in Figure 25 were observed or instrument drift and sensitivity precluded obtaining an analytically meaningful response. The complication of tip residue may become a more noteworthy concern for longer retract times, where greater viscoelastic necking is expected. Table 7 shows means of penetration depth and means and standard deviations of work of cohesion for all 33 sample types used in cohesion testing.

Table 7: Means and standard deviations for work of cohesion and penetration depth

Dust ratio	Binder	Filler type	Work of Cohesion (J/m <sup>2</sup> )	Penetration depth (nm)
0	PG 70-22	n/a	0.036 ± 0.0049	6239
0.3	PG 70-22	Hydrated lime	0.069 ± 0.0118	2853
0.6	PG 70-22	Hydrated lime	0.094 ± 0.0099	1420
0.8	PG 70-22	Hydrated lime	0.092 ± 0.0158	1495
1.0	PG 70-22	Hydrated lime	0.093 ± 0.0074	1334
1.26	PG 70-22	Hydrated lime	0.094 ± 0.0100	1711
0	PG 70-28 SBS	n/a	0.038 ± 0.0050	9622
0.3	PG 70-28 SBS	Hydrated lime	0.048 ± 0.0061	7407
0.6	PG 70-28 SBS	Hydrated lime	0.087 ± 0.0166	4448
0.8	PG 70-28 SBS	Hydrated lime	0.097 ± 0.0138	1956
1.0	PG 70-28 SBS	Hydrated lime	0.100 ± 0.0078	2109
1.29	PG 70-28 SBS	Hydrated lime	0.099 ± 0.0040	2574
0	PG 64-22	n/a	0.036 ± 0.0065	8726
0.3	PG 64-22	Hydrated lime	0.044 ± 0.0068	6750
0.6	PG 64-22	Hydrated lime	0.067 ± 0.0060	4153
0.8	PG 64-22	Hydrated lime	0.077 ± 0.0126	1902
1.0	PG 64-22	Hydrated lime	0.079 ± 0.0087	1686
1.2	PG 64-22	Hydrated lime	0.080 ± 0.0075	1693
0.3	PG 70-22	granite	0.043 ± 0.0040	8165
0.6	PG 70-22	granite	0.058 ± 0.0062	2334
0.8	PG 70-22	granite	0.057 ± 0.0042	5577
1.0	PG 70-22	granite	0.056 ± 0.0046	2878
1.2	PG 70-22	granite	0.057 ± 0.0041	2634
0.3	PG 70-28 SBS	granite	0.039 ± 0.0039	7781
0.6	PG 70-28 SBS	granite	0.051 ± 0.0079	8197
0.8	PG 70-28 SBS	granite	0.063 ± 0.0051	5523
1.0	PG 70-28 SBS	granite	0.062 ± 0.0045	8257
1.2	PG 70-28 SBS	granite	0.063 ± 0.0038	5448
0.3	PG 64-22	granite	0.038 ± 0.0027	10340
0.6	PG 64-22	granite	0.045 ± 0.0056	5458
0.8	PG 64-22	granite	0.055 ± 0.0051	4786
1.0	PG 64-22	granite	0.059 ± 0.0037	3527
1.2	PG 64-22	granite	0.059 ± 0.0049	3314

All work of cohesion values for all indentation curves are plotted against penetration depth in Figure 27 and Figure 28, where each data point represents one indentation test. A distinct clustering of work of cohesion values is shown according to sample type.

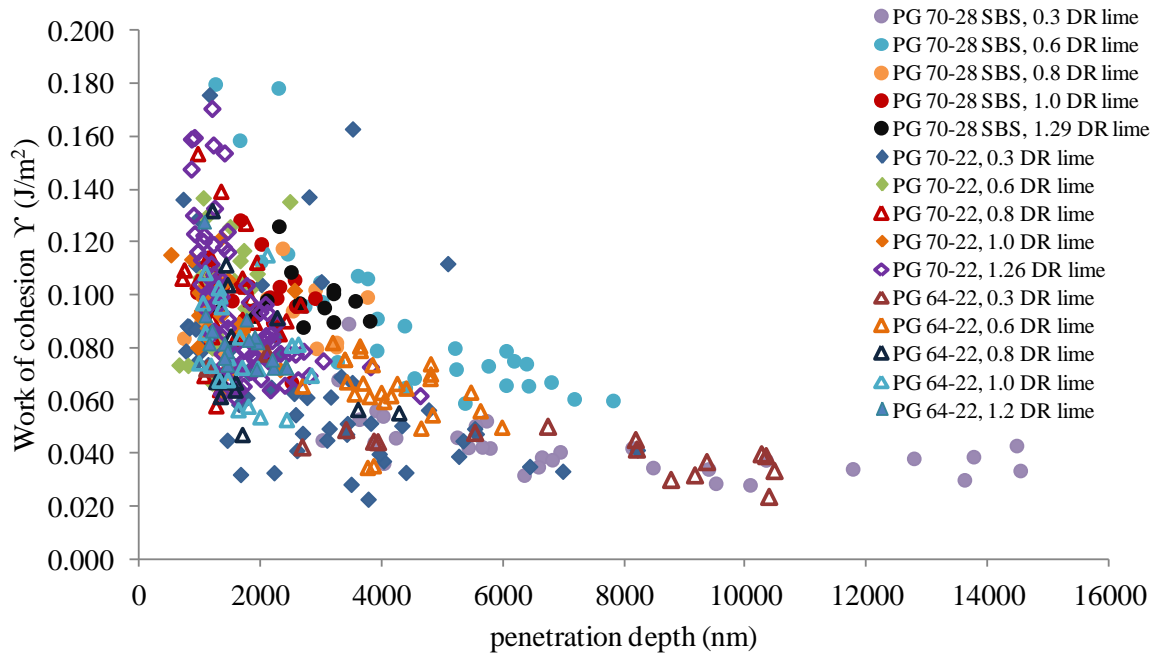


Figure 27: Work of cohesion vs. penetration depth (lime)

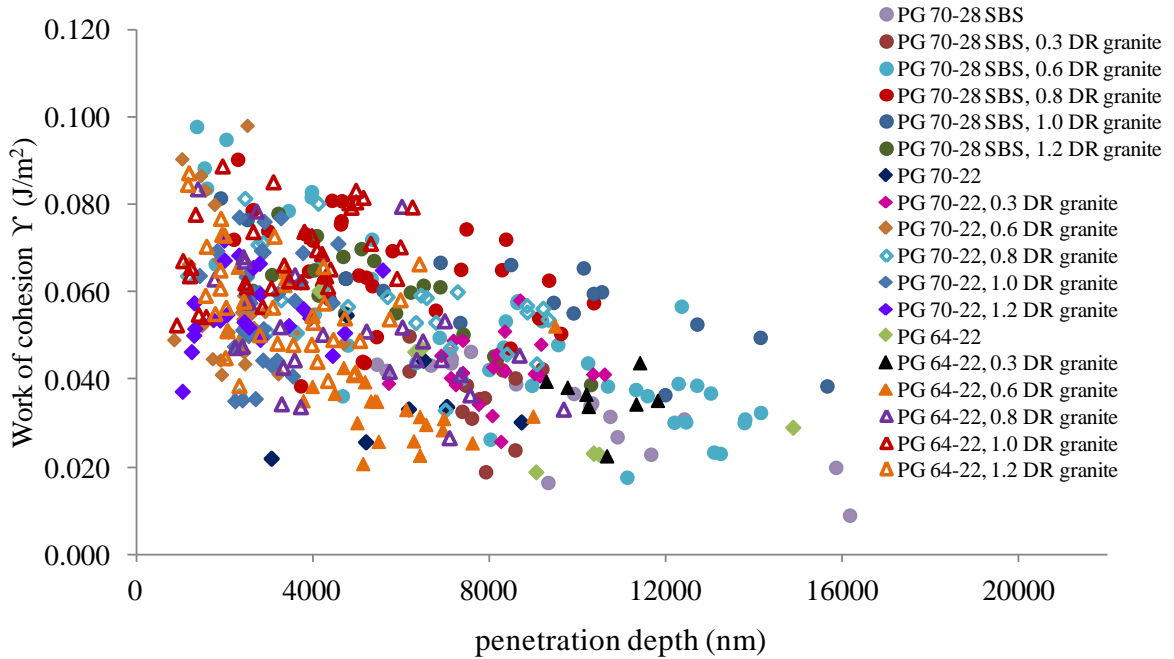


Figure 28: Work of cohesion vs. penetration depth (granite)

The contact areas have radii in the range of the penetration depths, which are mostly below 10  $\mu\text{m}$ . Based on AFM investigations of asphalt binder microstructure [58], this suggests the possibility of testing within individual microstructures rather than testing of the bulk binder, which could explain some of the variability in test results. Typical bee sizes can range from 1  $\mu\text{m}$  up to 35  $\mu\text{m}$  in length [58].

Figure 27 and Figure 28 show a clustering of work of cohesion values according to sample type. The mastics with the highest dust ratio have the highest average work of cohesion, and the binders have the lowest average work of cohesion. Since the experiments are load-controlled, penetration depth cannot be controlled directly, although the two quantities have a direct relationship. In effect, the penetration depth is a “surrogate” variable since the true testing input is the contact load. Since the  $\gamma$  dependence in Equation (63) is only on penetration depth and cohesive force, the measurements of Figure 27 and Figure 28

also reflect differences in stiffness behavior and contact areas, which are functions of the dust ratio.

It is observed that the penetration depths for lime are lower than those of granite. Lime has an order of magnitude increase over granite in SSA and much higher Rigden voids (fractional voids in a compacted filler sample). This is caused by the high dry porosity of lime compared to granite and increases the mechanical stiffening effect in lime [39]. This stiffening effect is being manifested in lower average penetration depths for lime compared to those of granite.

Some groups of indents have a much wider distribution of penetration depths than others. This is partly due to limitations from instrument sensitivity and the nature of viscoelastic materials under the constraint of minimal hold time, whereby samples do not have an opportunity to deform as much as they would with longer hold times. The time-delayed viscoelastic (creep) nature has not yet had a chance to truly be captured during the brief ramp-and-hold phase, which takes no more than 2-3 seconds. This still provides ample time and penetration for the software to register a meaningful and accurate pull-off force, and the unloading phase is set to a long enough duration for the cohesive nature to be fully activated and registered. These factors, coupled with stress and strain-rate complexities for a sphero-conical tip, can account for discrepancies in penetration depth trends.

Figure 29 and Figure 30 plot the maximum tensile pull-off force as a function of penetration depth to show a direct relationship between the two variables.

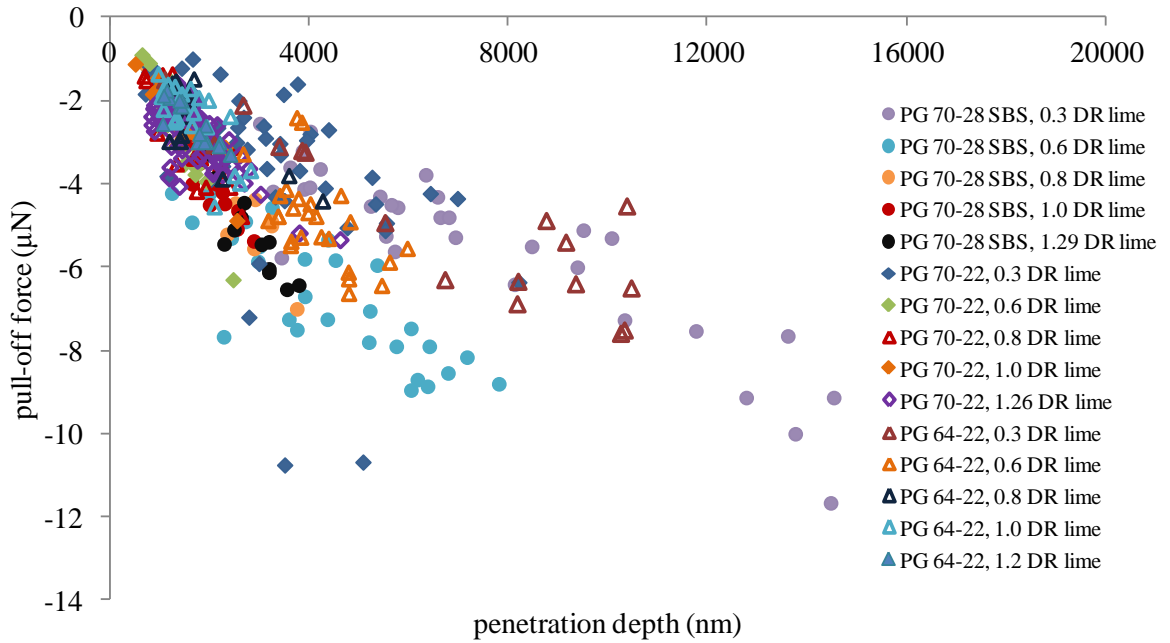


Figure 29: Pull-off force vs. penetration depth (lime)

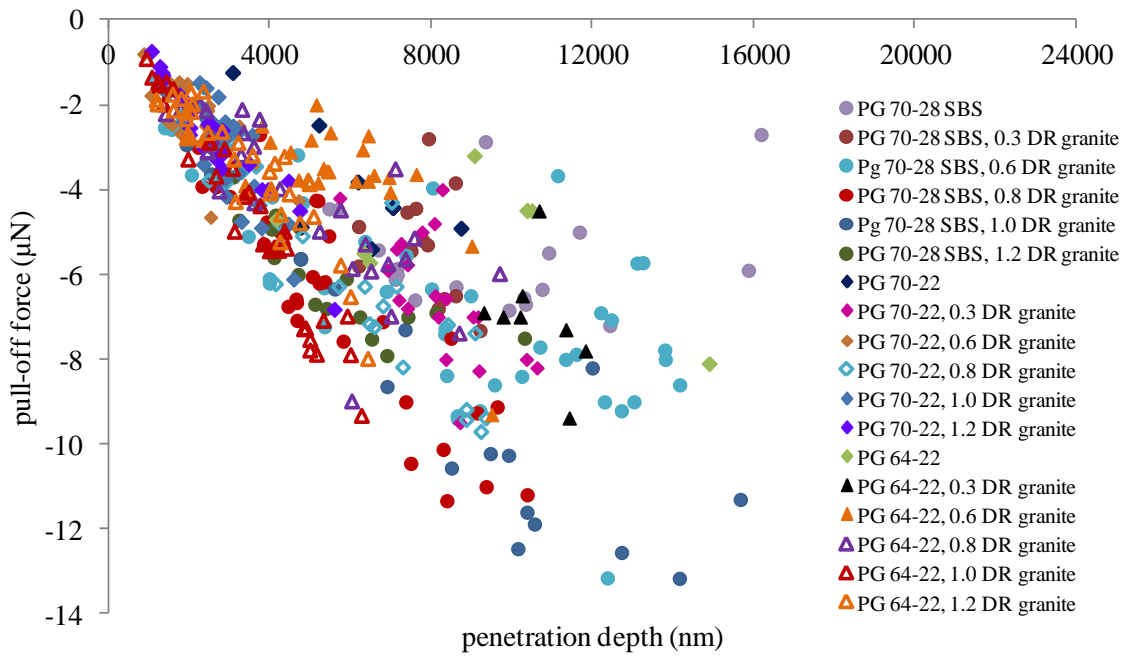


Figure 30: Pull-off force vs. penetration depth (granite)

Work of cohesion values are plotted against contact load in Figure 31 and Figure 32. As expected from Equation (63),  $\gamma$  is shown to be independent of contact load, with no clearly discernable trends or tendencies in Figure 31 and Figure 32.

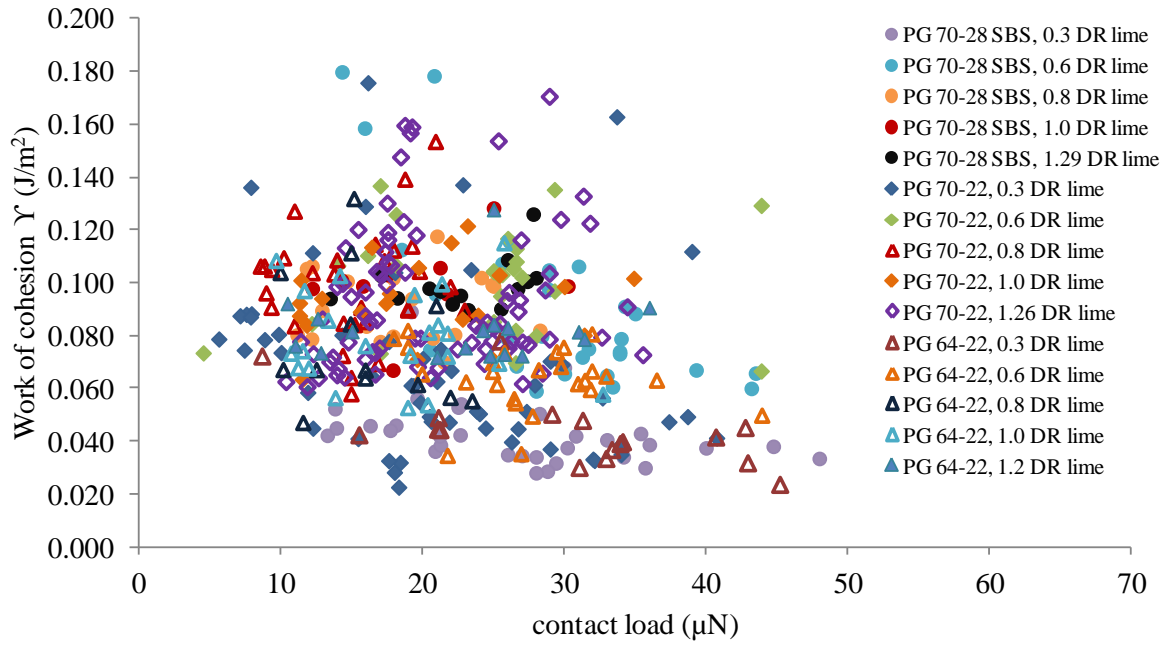


Figure 31: Pull-off force vs. contact load (lime)

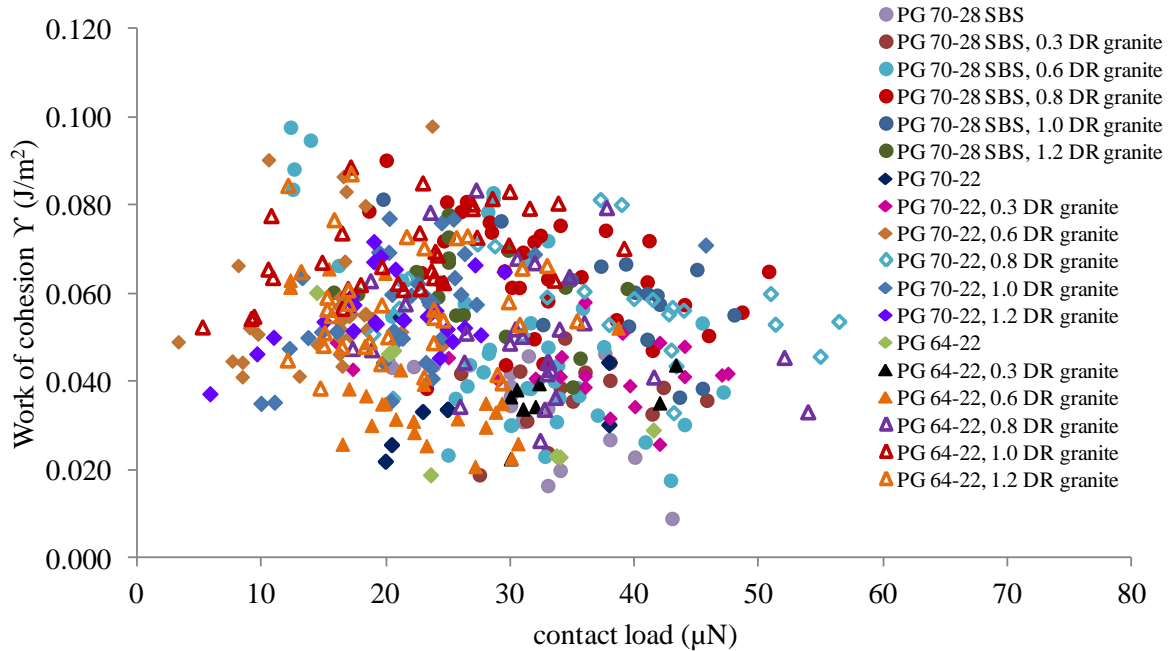


Figure 32: Pull-off force vs. contact load (granite)

Figure 33 is the most interpretive series of graphs for the cohesion research. It displays the average work of cohesion data as a function of dust ratio, binder, and filler (a and b) and as a function of filler volume fraction, binder, and filler (c and d) to clearly isolate and illustrate the trends of Figure 27 and Figure 28. The same scales render an easier comparison when so many materials (33) are involved.

We observe that the work of cohesion for each sample type with lime is higher than that of the associated sample type with granite, which is consistent with asphalt mixture investigations which indicate lime improves cracking resistance, thus providing evidence that the developed nanoindentation approach is able to discriminate the relative fracture resistance of different mastics [39], [41]. As a general trend, the work of cohesion increases as more filler is added in the mastic, for any given set of loading conditions per material, until a critical percolation threshold emerges after which point the work of cohesion is insensitive to filler addition.

Figure 33 shows that the work of cohesion has a nonlinear dependence to dust ratio and that the rate of change of  $\gamma$  with respect to the dust ratio is binder- and filler-dependent (and hence specific surface area-dependent). Points are connected with straight lines in the absence of a true physical model to describe the asymptotic relationship. The mass dust ratio is converted to filler volume fraction  $\phi$  by using the specific gravities of 2.58 and 2.70 for typical granite and hydrated lime fillers, respectively, based on typical values reported in the literature [5]. From Figure 33, a plateau on  $\gamma$  as a function of  $\phi$  is observed at a critical filler volume fraction for each binder-filler combination, indicating convergence of work of cohesion. The plateau work of cohesion values for PG 70-28 SBS, PG 70-22, and PG 64-22 with lime filler are 0.099, 0.094, and 0.08 J/m<sup>2</sup>, respectively. The plateau work of cohesion values for PG 70-28 SBS, PG 64-22, and PG 70-22 with granite dust are 0.063, 0.059, and 0.057 J/m<sup>2</sup>, respectively. The work of cohesion values reported in the current study for PG 70-28 SBS, PG 70-22, and PG 64-22 with no filler are 0.038, 0.035, and 0.037 J/m<sup>2</sup>, respectively. For comparison, the equilibrium work of adhesion value reported in Pauli et al. [60] for SHRP binder AAD-1 at 2.0°C was 0.054 J/m<sup>2</sup>, and the LW components of binder surface energy values reported in Little and Bhasin [40] ranged from 0.04 to 0.05 J/m<sup>2</sup>. Hence, the results for work of cohesion presented in this paper are consistent with one another from sample to sample, with Pauli et al.'s AFM results, and with binder surface energy values from Little and Bhasin [40].

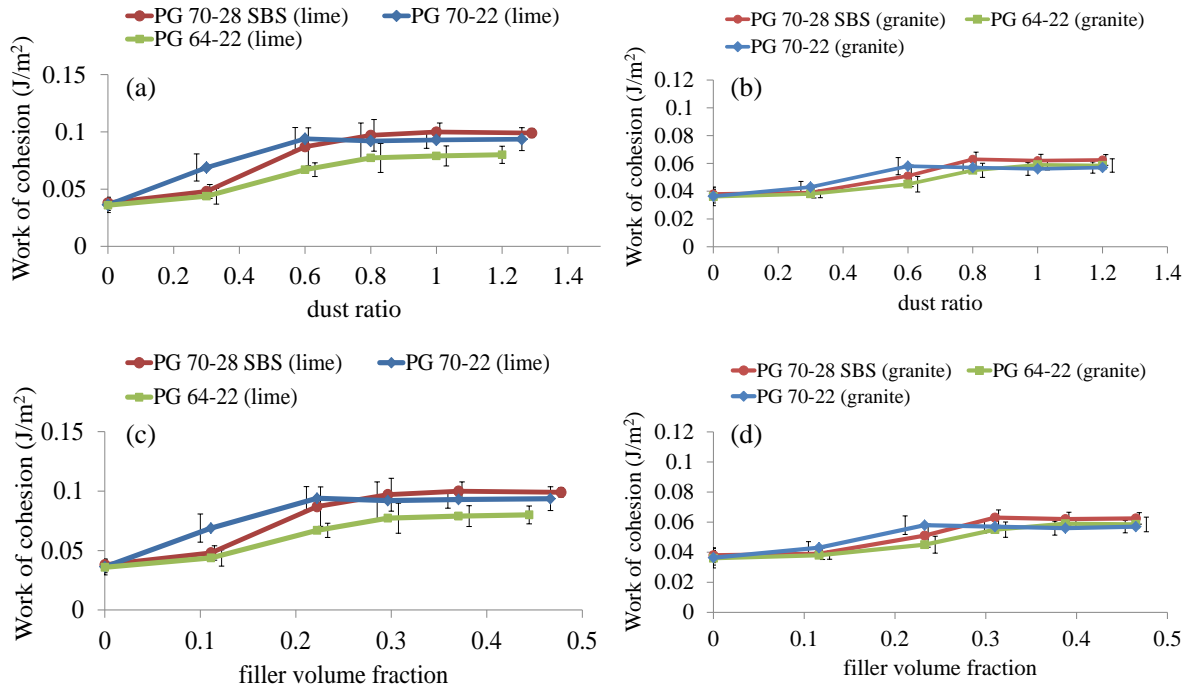


Figure 33: (a) work of cohesion vs. dust ratio for mastics with lime; (b) work of cohesion vs. dust ratio for mastics with granite; (c) work of cohesion vs. filler volume fraction for mastics with lime; and (d) work of cohesion vs. filler volume fraction for mastics with granite

Based on Table 7, PG 70-28 SBS binder has a slightly higher work of cohesion than PG 70-22 and PG 64-22 binder. Based on Figure 33, the work of cohesion values for mastics with PG 70-28 SBS converge to the highest  $\gamma$  for both lime and granite filler. In both cases, SBS modification is known to improve fracture resistance and thus, trends match expectations.

Replacing lime with granite filler leads to significantly lower plateau work of cohesion values. Granite mastics showed less sensitivity to work of cohesion with varying binder type and filler concentration compared to lime mastics. Lime is known to be an “active” filler that affects binder behavior more drastically due to its high specific surface area and porosity compared to granite and thus, trends are consistent with expectations, as it

is well-demonstrated that the addition of hydrated lime improves fracture resistance of asphalt concrete [39], [41].

The results in this research provide a new insight into the cohesive nature of asphalt binder and mastic without introducing limitations from incomplete tip geometries or analysis. However, some uncertainty remains as to precisely what material volume the tip is probing in a nanoindentation cohesion test. Indentation depths in cohesion tests are substantially small than creep tests and thus, it is difficult to ascertain if one is probing both filler and binder. An understanding of the mechanisms governing filler strengthening help support observations from work of cohesion trends, but those arguments do not account for the uncertainty from individual data points. The statistical significance of this uncertainty becomes less important with the large number of tests collected for the structured set of data. It is speculated that the indenter tip is probing either a binder-and-filler composite, which is increasingly likely for higher filler volume fractions, or volumes of binder farther away.

## CHAPTER 8: AFM IMAGING

### 8.1 Microstructures from AFM Imaging

AFM images provide a map of microstructural features on a sample surfaces and hence, provide a means to infer how microstructural phenomena may affect nanoindentation results, including inference of physicochemical interaction between binder and filler. The higher order goal of the AFM images is to link binder and mastic mechanical properties to microstructural observations by accounting for the complexities of the physicochemical interaction, which consist of contributions from both the chemical composition of components and their physical properties. AFM images obtained for the three binders and all mastics considered in this study generally show up to three different microstructures, known as the periphase, paraphase, and catanaphase (bee phase). Figure 34 shows an example image with these features labeled.

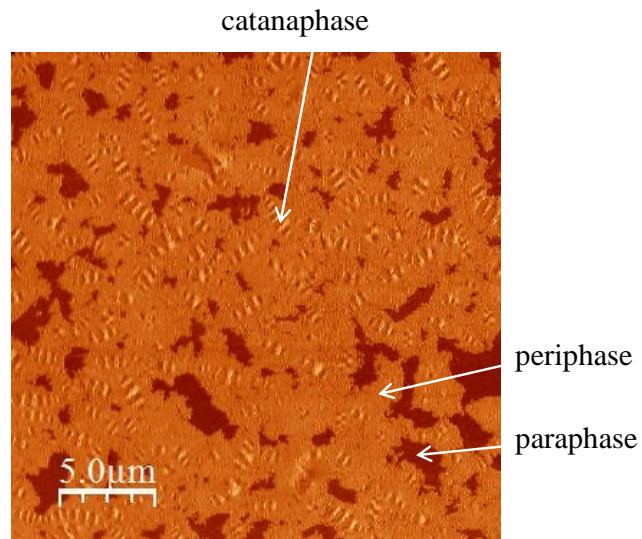


Figure 34: Example AFM image with labeled microstructures

The periphase is the area surrounding the bee structures, and the paraphase is any collection of dark areas of the phase images, most commonly surrounding the periphase, depicting especially soft or sticky regions. These microstructures appear in the phase contrast image rather than the height image because their softness and stickiness affect the time delay between the cantilever driving and response oscillations. A feature with greater adhesive, cohesive, or viscoelastic effects leads to a greater time delay between driving and response oscillations and, in turn, a more pronounced phase angle that is represented through a specific microstructure in a phase contrast image.

In applying AFM to asphalt mastics, it is speculated that one is actually probing the binder within the mastic. Filler particles are coated in asphalt binder and hence, no particles are exposed at the surface of samples which AFM probes. In some instances, filler particles near the surface were detected as bright spots on AFM topographical images. However, these fillers are still embedded in a thin layer of asphalt, based on phase images where filler presence was not detected. Physicochemical interactions between asphalt binder and filler lead to selective adsorption of asphalt components. The resultant viscoelastic matrix contains a lower concentration of polar components. The reduction in polar components is expected to result in a viscosity reduction in the “effective” non-adsorbed binder matrix, and the non-adsorbed binder probed in AFM is expected to display a different microstructure from the bulk binder. Thus, the degree of change in binder microstructure as a result of addition of filler can be used as an indicator of the degree of physicochemical interaction.

All AFM images are shown in Appendix A. The mastics (Figures A.1 – A.3) are organized by binder type followed by dust ratio and filler type, and the binders are shown in Figure A.4 of Appendix A. Height images are shown in the left, and phase images are shown on the right. Phase images are more instructive than height images in soft, viscous materials for seeing all microstructural phases that occur within the frame, based on the underlying operational mechanism of how phase images are generated. It is clear from the images in Appendix A that addition of fillers alters the structuring of the catanaphase (i.e., bee phase). There is no clear indication of SBS polymer modification in AFM images, an observation which is consistent with Wu et al. [82]. Furthermore, it is observed that an increase in filler

concentration generally increases the significance of change in the catanaphase microstructure. Hence, it is hypothesized that the degree of change in bee structures can be used as an indicator of the amount of adsorption of asphalt components onto filler surfaces. In turn, it is speculated that the degree of change in bee structures can be linked to nanoindentation cohesion and viscoelasticity results to better understand the implications of physicochemical interactions on both mastic behavior and microstructural changes for increasing filler volume fractions.

## 8.2 Image Processing Results

The image processing program ImageJ was used to calculate proportions of images occupied by the catanaphase, average bee size, and number of bees within each AFM phase image. Figure 35 plots the percentage components of bees (proportion of the bee microstructure) within each AFM phase image.

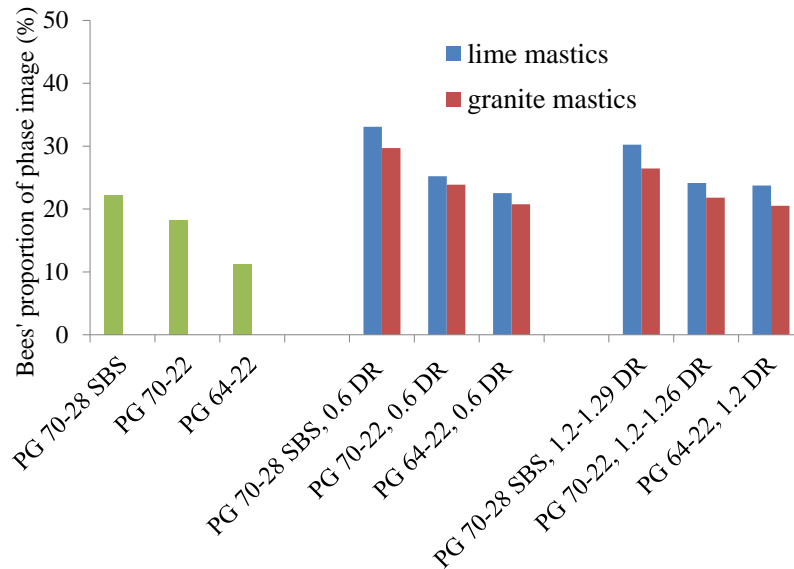


Figure 35: Bees' proportion of phase image for binders and mastics

From Figure 35, the proportion of bees increases from binder to 0.6 dust ratio and stays relatively constant from 0.6 to the highest dust ratios for all binder and filler types. It is also observed that the greatest change in bee proportion is observed in lime mastics, which is expected as lime has a significantly higher specific surface area compared to granite and is thus expected to lead to a greater extent of physicochemical interaction. Since dust ratio is based on mass, constant volume concentrations allow for a better metric of comparison. Lime's low bulk density captures its high porosity and Rigden void value, and this high porosity and Rigden value increase lime's stiffening potential compared to mineral fillers such as granite.

The periphase and paraphase were excluded from Figure 35's analyses because the paraphase was not always clearly visible in each phase image. The most consistent and reliable microstructure in each image was the catanaphase. Each AFM image requires independent, careful optimization of scanning parameters for a proper feedback loop process, and differences in apparent microstructures can occasionally be attributed to the imaging process itself.

Average bee size is necessary to encompass the entire distribution of bees within each phase image. Table 8 lists the number of bees and average bee size for all materials tested in the AFM.

Table 8: Number of bees and average bee size for all materials tested in AFM

binder	dust ratio	filler	Number of bees	Average bee size ( $\mu\text{m}$ )
PG 70-28 SBS	1.29	lime	148	$2.18 \pm 0.31$
PG 70-28 SBS	1.2	granite	123	$2.29 \pm 0.49$
PG 70-22	1.26	lime	151	$2.16 \pm 0.23$
PG 70-22	1.2	granite	109	$1.89 \pm 0.20$
PG 64-22	1.2	lime	167	$1.01 \pm 0.09$
PG 64-22	1.2	granite	118	$1.32 \pm 0.31$
PG 70-28 SBS	0.6	lime	60	$3.92 \pm 1.24$
PG 70-28 SBS	0.6	granite	68	$3.28 \pm 1.05$
PG 70-22	0.6	lime	53	$4.37 \pm 2.01$
PG 70-22	0.6	granite	59	$3.62 \pm 0.83$
PG 64-22	0.6	lime	69	$4.02 \pm 1.09$
PG 64-22	0.6	granite	36	$3.72 \pm 1.46$
PG 70-28 SBS	0	binder	47	$6.68 \pm 1.17$
PG 70-22	0	binder	46	$5.41 \pm 1.02$
PG 64-22	0	binder	27	$4.89 \pm 1.76$

Figure 36 provides a graphical representation of average bee size for all of the materials tested in the AFM.

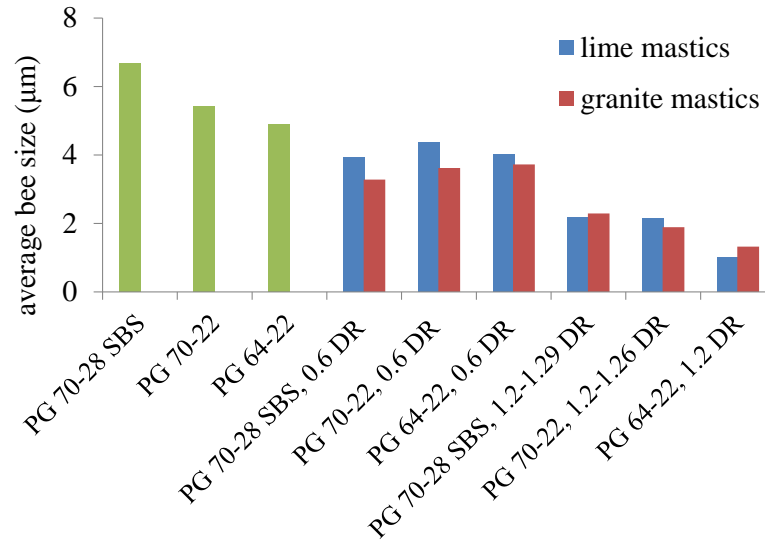


Figure 36: Average bee size for all materials tested in AFM

Figure 36 shows a steady decrease in average bee size with increasing filler volume fraction and generally demonstrates consistent trends with respect to filler type and bee proportion results presented in Figure 35. The differences in average bee size between lime and granite mastics are not dramatic at 0.6 dust ratio and the highest dust ratios, although the differences in average bee size between dust ratios for all binder types are much more significant. There does not appear to be a clearly definable trend when comparing average bee size among different binders, since the rank ordering of binder based on bee size changes between binder and 0.6 dust ratio and when changing filler type. However, microstructural differences among binders can still complement filler results and help explain viscoelasticity and cohesion trends; this will be further investigated in Chapter 10.

Figure 37 plots average bee size vs. number of bees for the data from Table 8 to more clearly isolate and interpret the direct relationship of decreasing average bee size for increasing number of bees.

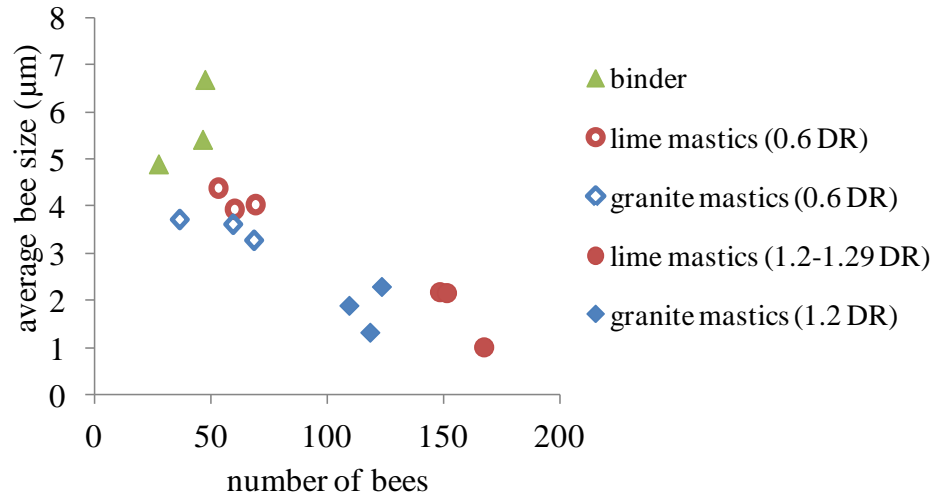


Figure 37: Average bee size vs. number of bees

As a general observation from Figure 37, lime mastics have a greater quantity of bees at the highest dust ratios by a large margin compared to their granite counterparts (i.e. keeping binder and dust ratio constant), and lime mastics have a higher average bee size for the intermediate dust ratios compared to their granite counterparts. This trend matches expectations and thus, provides support that physicochemical interactions between binder and filler contribute to the microstructural changes observed in AFM images.

Overall, AFM images provide another scale with which to clarify and support nanoindentation results by improving a fundamental understanding of the mechanisms of interaction between asphalt binder and filler.

## CHAPTER 9: DISCUSSION ON SYNTHESIS OF ALL RESULTS

The primary goal of this chapter is to synthesize results of binder and mastic viscoelasticity and cohesion measured by nanoindentation with AFM images of binder and mastic microstructure in order to provide links between composition, microstructure, and material properties. To accomplish this goal, cohesion results for RTFO-aged materials from nanoindentation data [81] are combined with creep-based viscoelastic nanoindentation results (from Chapter 6) and AFM images of binder microstructure (from Chapter 8) to more broadly characterize viscoelastic and cohesive properties of asphalt binder and mastic.

Viscoelasticity is critical to understanding how asphalt deforms under loading, and cohesion is directly related to fracture resistance. The goal of the creep nanoindentation experiments is to obtain the dynamic modulus  $|E^*|$  values, which are validated using DSR tests. The nanoindentation experiments are conducted within a very small volume of material, opening up many possibilities for future research in assessing mastic properties within an asphalt concrete sample. While enabling in-situ mastic testing with asphalt concrete, nanoindentation tests are conducted using a tip of sufficient size to measure bulk binder responses. The length scales are distinct from mechanical experiments with AFM, which utilizes a much smaller tip and can probe non-adsorbed binder. In this research, AFM is used only to identify the distribution of microstructures within binder in order to link microstructural implications of interactions between filler and binder to cohesion and viscoelasticity.

In this chapter, various factors and mechanisms influencing the observed linear viscoelastic and cohesive behavior are discussed, and relationships between trends in viscoelasticity and cohesion results among the tested materials are linked to microstructural data and differences.

## 9.1 Possible Reinforcement Mechanisms

With the results of linear viscoelastic properties, AFM imaging, and cohesion established, it is useful to describe the influence of various factors on the degree of stiffening, and thereby performance, within the framework of combined observations from the results. Transitioning from localized material factors to performance-related properties is often a dark art, with the filler and binder properties that govern the degree of stiffening, as well as other behavior, operating in a multiple-agent system that is still poorly understood. With the data reported here, factors contributing to stiffening potential and cohesive potential can be explored individually to improve understanding of the complex system.

### 9.1.1 Volume Filling in Mastics

The most basic type of reinforcement as binder develops into mastic comes from purely mechanical volume-filling effects. Volume-filling reinforcement is the stiffening caused by the presence of rigid inclusions in a less rigid matrix [8]. In this case, asphalt is stiffened simply by the replacement of a portion of the binder volume with more rigid filler inclusions. Mastic, as a composite, is expected to show less viscous behavior with increasing filler inclusions. This level of stiffening is assumed to be adequately described by the generalized self-consistent scheme (GSCS) micromechanical model [8]. The base GSCS model assumes spherical inclusions and does not consider physicochemical reinforcement or particle interactions.

A stiffening ratio  $|G^*|_{\text{mastic}} / |G^*|_{\text{binder}}$  is plotted in Figure 38 over all tested filler volume fractions, binder types, and filler types. The micromechanics model prediction based on the GSCS is also plotted in Figure 38 for comparison.

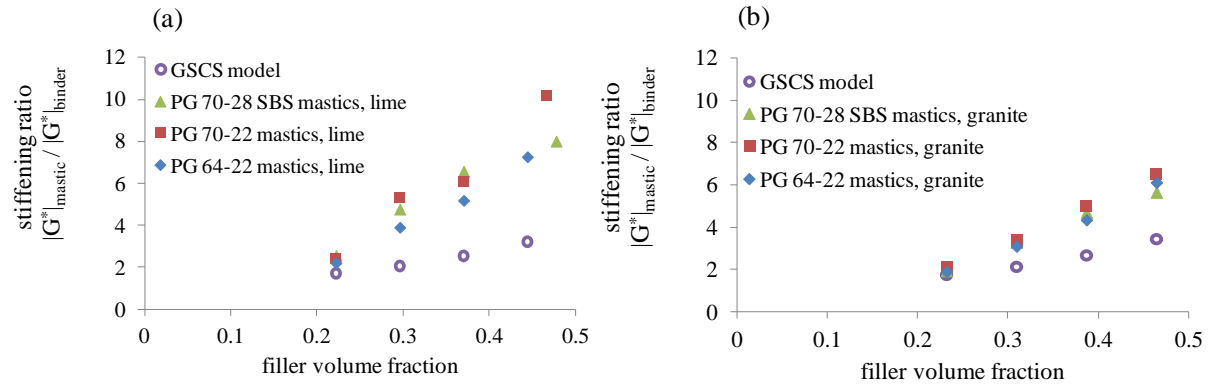


Figure 38: Stiffening ratio  $|G^*|_{\text{mastic}} / |G^*|_{\text{binder}}$  vs. filler volume fraction for (a) lime mastics and (b) granite mastics

The results indicate a progressively increasing  $|G^*|_{\text{mastic}} / |G^*|_{\text{binder}}$  stiffening ratio which diverges from the GSCS model prediction at higher volume fractions. Data over-predictions and sensitivity to filler type indicate that mastic stiffening effects beyond volume-filling, such as physicochemical reinforcement, are occurring, and increasing divergence of stiffening ratios from the model prediction at higher filler volume fractions likely indicate particle interactions. The results of Figure 38 confirm that volume-filling reinforcement cannot be entirely responsible for the observed trends in linear viscoelastic properties. A combination of microstructural effects are likely responsible for the observed increases in dynamic modulus with filler volume fraction, as no one mechanism can fully explain the observations. The AFM imaging and cohesion results strongly suggest effects beyond volume-filling reinforcement as binder microstructure is affected by the addition of filler, suggesting physicochemical interactions between filler and binder. Thus, an investigation of physicochemical interactions and particle interactions is conducted in Sections 9.1.2 and 9.1.3 within the context of results of linear viscoelastic properties, AFM imaging, and cohesion.

### 9.1.2 Physicochemical Interactions

It has been well-documented in the literature that physicochemical interactions between filler and binder lead to selective adsorption of polar components of asphalt binder onto filler surfaces [10], [41]. Physicochemical interactions lead to the formation of an adsorbed interphase layer on filler surfaces. In addition, the resultant viscoelastic matrix contains a lower concentration of polar components. The reduction in polar components is expected to result in a viscosity reduction in the “effective” non-adsorbed binder matrix, which some have speculated to improve fracture resistance [41] whereas the formation of an adsorbed layer on filler particles may have a stiffening effect [8]. Filler specific surface area is known to affect the extent of physicochemical interaction between binder and filler [10], [41]. Lime has significantly higher specific surface area compared to granite and thus, physicochemical interactions are anticipated to be greatest in lime mastics where greater filler surface area is available for adsorption of asphaltenes. The increased work of cohesion of lime mastics compared to granite could be related to greater extents of physicochemical interactions in lime mastics since the adsorption of polar binder constituents is anticipated to improve fracture resistance of the non-adsorbed binder matrix.

The results of AFM imaging analysis demonstrate changes in asphalt binder microstructure with the addition of filler (Table 8, Figure 35, Figure 36, and Figure 37), suggesting physicochemical interactions exist in mastics. The extent of change in binder microstructure proportions, as seen in Figure 35, was found to be greatest in lime mastics, as expected due to the high SSA of lime compared to granite and consistent with cohesion results which demonstrate greater work of cohesion for lime compared to granite mastics. Furthermore, it is speculated that the consistency in asphalt binder microstructure with addition of filler beyond a dust ratio of 0.6 for all binder and filler types evaluated (Figure 35) is related to the observed plateaus in work of cohesion from nanoindentation results. These results highlight the critical impact of filler physicochemical interactions with asphalt on fracture resistance.

Physicochemical interactions may also affect viscoelasticity. However, the effect of the formation of the adsorbed interphase layer and softening of the non-adsorbed matrix resulting from these interactions make direct quantification of physicochemical effects on viscoelasticity difficult. While it is well-established that loss of polar asphalt components to adsorption will soften the effective asphalt matrix in mastics, the effects of the adsorbed interphase layer on viscoelasticity remains to be quantified. Trends observed in the creep compliance results shown in Figure 17 and Figure 18 demonstrate lime mastics have a reduced creep compliance compared to that of granite mastics. As discussed, cohesion and AFM results indicate greater physicochemical interaction in lime mastics than granite mastics. These results imply that the effect of asphalt binder matrix softening does not have as significant an effect on viscoelasticity as the formation of the adsorbed interphase layer and / or particle interactions. Results in Figure 38 demonstrate some sensitivity in the stiffening effect of filler to binder type. The stiffening effect of filler addition would generally be expected to be greatest for the softest binder (i.e., PG 64-22). However, results demonstrate PG 70-22 mastics generally show the highest  $/E^*$  ratios while PG 64-22 mastics generally show the lowest  $/E^*$  ratios. Similarly, work of cohesion in mastics prepared with PG 64-22 was least affected by the addition of hydrated lime filler. These results suggest that the physicochemical interactions between binder and filler can significantly impact viscoelasticity and work of cohesion in mastics.

### **9.1.3 Particle Interactions**

At low volume fractions, particles are randomly distributed within the viscoelastic matrix. At higher volume fractions, there is a greater likelihood for particles to become interconnected, forming a structuralized framework eventually resulting in percolation of filler particles if the volume fraction is sufficiently high. The percolation threshold represents the emergence of filler connectivity whereby filler begins acting as the continuous phase in a discrete binder matrix. Particle interactions cannot be inferred from AFM which

only probes asphalt binder microstructure. However, trends in viscoelasticity can be used to ascertain emergence of filler particle connectivity.

Results presented in Figure 38 show a consistently increasing dynamic modulus with increasing filler which deviates significantly from GSCS model predictions, particularly for high filler volume fractions. These results suggest the existence of particle interactions in asphalt mastics. This is expected since stiffness ratios continue to increase, at higher rates [8], [65], for increasing filler volume fractions due to a combination of filler reinforcement mechanics. The structuralized framework is also captured by comparing the extreme cases of creep compliance results between binders and mastics in Figure 16, Figure 17, and Figure 18. The increased potential for percolation is observed by reduced creep compliance for mastics compared to binders. Hydrated lime is much more porous than granite, which leads to a higher fractional void content and hence, earlier percolation than granite [39]. Thus, particle interactions are expected to be most pronounced in lime mastics, which is consistent with viscoelasticity results that consistently demonstrate lime mastics are stiffer than granite for equivalent dust ratios.

The observed trends in terms of structuralization and evolution of particle interactions in viscoelasticity results are fundamentally different than trends in cohesion results. In cohesion results, a plateau in work of cohesion emerges at a critical filler concentration beyond which addition of filler did not affect work of cohesion. Figure 33 demonstrates differences in effects of granite and hydrated lime on work of cohesion, which could be related to physicochemical interactions as discussed but could also reflect differences in particle interactions.

Based on Figure 33, the range for the experimentally determined percolation threshold  $\phi_{crit}$  from this research is 0.20 – 0.30 filler volume concentration, given the limit in resolution of intervals for filler volume fraction. This is within the well-documented range from literature of 0.15 – 0.30 [65], based on percolation theory. Together, the nanoindentation and AFM results provide some new clues about the interactions between binder and filler in mastic.

# CHAPTER 10. CONCLUSIONS AND RESEARCH CONTRIBUTIONS

## 10.1 Summary of Main Findings

Nanoindentation techniques for determining the linear viscoelastic and cohesive properties of aged asphalt binders and mastics with varying filler volumetric concentrations were implemented to calculate and interpret important linear viscoelastic and cohesive properties from nanoindentation data through low-load sphero-conical (blunt) nanoindentation. Atomic Force Microscopy (AFM) images of asphalt binder microstructure within asphalt mastics were coupled with nanoindentation results to shed insight on reinforcement mechanisms in mastics. The salient findings can be summarized as follows:

1. The experimental techniques for creep-based nanoindentation on 3 binders and 24 mastics (RTFO-aged) were optimized and implemented for replicable and reproducible creep indentations at ultra-low loads. Creep compliance model parameters were fitted and extracted to plot dynamic modulus values for each of the 27 aged materials used in creep testing. Dynamic modulus values determined from nanoindentation and the DSR for two binders and two mastics (RTFO-aged) at the highest dust ratios were found to be in agreement at room temperature. Linearity in viscoelastic behavior was verified, and creep compliance trends were internally consistent with one another and with dynamic modulus trends.
2. AFM images provided an additional perspective and showed varying microstructural features across different mastics. Although differences between binders were not significant, the addition of manufactured (lime) and mineral (granite) fillers significantly changed the microstructure, resulting in a greater quantity of smaller bees with increased filler fraction. It is inferred that the observed changes in microstructure reflect physicochemical interactions between asphalt binder and mastic. While changes in microstructure are found to be

initially sensitive to filler concentration, relatively consistent microstructures, as measured by proportions of bees, were observed beyond a dust ratio of 0.6, indicating a possible limit in adsorption capacity.

3. Work of cohesion values are determined for 3 binders and 30 mastics (RTFO-aged) prepared with granite and lime fillers of varying concentrations. To the author's knowledge, this is the first determination of work of cohesion for asphalt binder and mastic by analytical methods through nanoindentation, and the first determination altogether of work of cohesion for mastics. Work of cohesion results were combined with AFM and creep-based nanoindentation results to more broadly characterize viscoelastic and cohesive properties of asphalt binder and mastic. The cohesion results, consisting of plots of work of cohesion versus filler volume fraction, demonstrated plateaus in work of cohesion values, which were sensitive to filler and binder type. Beyond the percolation threshold, additional filler did not seem to have an appreciable influence on work of cohesion. Verification at a variety of filler volume fractions has helped to reduce interpolation errors and has cast a clearer understanding of the relationship between work of cohesion and filler volume fraction.
4. The various factors influencing the stiffening potential of fillers were discussed within the framework of results of linear viscoelastic properties, AFM imaging, and cohesion. The microstructural phenomena observed in the AFM images are likely linked to physicochemical interactions which influence viscoelasticity and cohesion. The combined effects of volume-filling reinforcement, physicochemical interactions, and particle interactions comprise the filler reinforcement mechanisms.
5. The combination of these mechanisms is speculated to be related to the observed plateaus in work of cohesion and to mastic stiffening, which leads to an increased dynamic modulus. It is also speculated that the consistency in proportion of bees between dust ratios of 0.6 and 1.2 for all binder and filler types is related to the observed plateaus in work of cohesion. This suggests that physicochemical

interactions significantly impact the fracture resistance of binder. Meanwhile, a combination of the microstructural effects are likely responsible for the observed increases in dynamic modulus with filler volume fraction, as no one mechanism can fully explain the observations.

Most of the research reported in this dissertation has been published as manuscripts in journals:

- i. Veytskin, Y., Bobko, C.P., and Castorena, C. (2014). Nanoindentation investigation of asphalt binder and mastic viscoelasticity. *International Journal of Pavement Engineering* ahead-of-print, 1-14.
- ii. Veytskin, Y., Bobko, C.P., Castorena, C., and Kim, Y.R. (2015, under review). Nanoindentation investigation of asphalt binder and mastic cohesion. *Mechanics of Materials*.
- iii. Veytskin, Y., Bobko, C.P., and Castorena, C. (2015, under review). Nanoindentation and atomic force microscopy investigations of asphalt binder and mastic. *Journal of Materials in Civil Engineering (ASCE)*.

This research is an encouraging and robust proof of concept in performing nanoindentation creep and pull-off tests on a soft, adhesive, and highly viscoelastic material. The results of this study prove the feasibility of such a characterization using a combination of microscale experimental techniques, theoretical formulations from linear viscoelasticity and adhesion, and a reliable computational modeling scheme.

The results also show that the technique can be adapted to other adhesive materials that may require similar loading programs. The results and conclusions from this research instill confidence that future efforts to overcome current challenges in applying nanoindentation techniques to asphalt concrete materials will be successful.

### **10.3 Future Perspectives / Future Research Beyond the Dissertation**

This research has opened possibilities for assessing mastic properties as they exist in the mix. Testing of binder and mastic through nanoindentation is an important first step for testing individual components of asphalt concrete in isolation from an in-service, field-extracted asphalt pavement core, in a controlled laboratory environment. With nanoindentation, testing on the individual components of a field core could be enabled. This type of testing is impossible using conventional macroscopic experimental methods. All potential physicochemical, volume-filling, and particle interactions between and within material phases would remain unaffected, and the constituent components would be relatively undisturbed by the in-service extraction process.

As a research tool, nanoindentation has the potential to develop and facilitate this new type of unexplored method for forensic investigations of binders within pavements. This method could then potentially supplement and provide additional insights to well-established DSR testing methods. A multi-scale modeling approach would involve indenting on a pavement core composite for component properties and using these properties as inputs for micromechanical models to predict composite properties.

Currently, forensic studies on asphalt binder within asphalt mixtures rely on solvent extraction and recovery to obtain asphalt binder specimens from laboratory produced asphalt mixtures or field cores, which are then tested ex-situ. These methods utilize solvents, heat, and centrifuge to separate asphalt from aggregate. There is also concern over the potential impacts of the use of solvent and subsequently residual solvent on asphalt binder microstructures. Testing binder ex-situ, through this extraction and recovery process, also limits assessment of cohesive and adhesive properties of the binder within asphalt concrete, as these properties are influenced by physicochemical interactions with aggregate.

Potential future applications for forensic nanoindentation testing of asphalt binder and mastic include measurement of changes in mechanical properties induced by oxidative age hardening, and studying phase distributions and effective binder properties within asphalt concrete from the blending of reclaimed asphalt pavement (RAP) with virgin binders.

Nanoindentation testing of RAP is a promising topic to pursue given the finite availability of virgin asphalt. The asphalt industry and research communities are still struggling to determine a methodology for evaluating how old and new asphalt in RAP are blended, and this requires a fundamental understanding of phase structuralization and compatibility.

Future research beyond this dissertation could allow for temperature variation in the experimental setup to replicate in-service conditions and responses. Viscoelastic models often appear sufficient and fit data well over narrow time scales but may not capture global behavior when temperature variation is not implemented. In this case, the viscoelastic model for creep compliance would benefit from being more robust than the current GPL implementation. Temperature variation will lead to comprehensive mechanical characterization and will allow for the construction of a nanoindentation-based mastercurve through a synthesis of individual modulus values, which can then be compared with mastercurves from the DSR method. A cooling stage will allow for predictions of the glassy asymptote in binder and mastic dynamic modulus mastercurves. Updating the viscoelastic model for creep compliance with the inclusion of temperature-varying data will also render the model more useful for interconversion across a stiffness range associated with a wider temperature range. Ultimately, it is hoped that such a viscoelastic model, based on nanoindentation principles, will prove useful to the asphalt pavement community as a supplement to DSR tests and allow for forensic measurements of binder and mastic properties throughout a pavement's service life.

In addition to capturing global behavior, updating the GPL model will also improve mechanical understandings of primary and secondary creep. While we strive to achieve a full creep response in data collection, a full creep response has also been recognized as a complicating factor in creep analysis. Most current methodologies tend to focus on steady-state, secondary creep, with the assumption that the influence of primary creep can be neglected due to its transient nature. While this is possible in conventional creep testing where constant stress fields exist, this is a highly complex problem in nanoindentation since regions of the sample undergoing primary creep are continually entering the steady-state creep strain field and influencing the indenter displacement response. The inclusion of

primary creep within a relatively simple functional form could be contributing to higher sensitivities governing creep behavior, especially since primary creep exhibits higher stresses and strain rates than secondary creep. These issues could be manifesting themselves in different ways through a GPL representation.

A rigorous analysis of dynamic indentation behavior of viscoelastic materials has yet to be reported. Efforts can be made to introduce loading frequencies to characterize a dynamic modulus through frequency-domain testing. In addition to dynamic testing in the frequency domain, other loading modes could be investigated, including time-domain displacement-controlled tests, to instantiate the viscoelastic interconversion principle and compare results from time- and frequency-domain testing. Interconversion is often required when conditions do not allow a response function to be determined through direct experimental testing, or when a response function cannot be determined over the complete range of its domain from a single test type. Many commercial nanoindenters, including the one used in this research, have the ability to perform dynamic mechanical analysis, which uses oscillatory loads to determine the storage and loss moduli, but require significant input parameter optimization. Dynamic viscoelastic indentation offers an advantage over quasi-static creep test methods by significantly decreasing testing time through the measurement of properties over the frequency domain rather than the time domain.

Advancement of these methods towards the improved characterization of viscoelastic properties may require material-independent calibration procedures, softer reference materials, advances in compatibility between instrumented indentation and temperature capabilities for a range of materials, and optimized testing and analysis procedures that account for rheological behavior. A future objective in creep testing for the nanoindentation community at large is to further develop the experimental and analytical techniques for dynamic viscoelastic nanoindentation to determine dynamic viscoelastic responses over wide frequency ranges. These results could then be compared to bulk properties measured from a standard dynamical mechanical analysis.

Future research can investigate in-situ adhesion testing in nanoindentation to help determine the work of adhesion between binder and aggregate. This would likely require tip

modification techniques similar to those used in AFM, such as particle attachment or other changes in tip surface chemistry that have yet to be validated. Binder-aggregate interfacial energy at failure is of significant concern in asphalt pavements. This interfacial energy can provide indications of the adhesive bond between aggregate and binder. Macroscale research in adhesion within asphalt concrete is generally aimed at determining the propensity of binders and mastics, based on their surface energy components, to debond from aggregate surfaces. It is hoped that nanoindentation experiments will play a role in understanding the level of debonding and stripping between binder and aggregate that can be caused by moisture damage.

Lastly, spectroscopic studies can help address lingering questions regarding the properties of the interphase layer around filler. Questions remain as to the thickness and shape of an interphase layer and the precise role it plays reinforcement mechanisms. The effect of the formation of the adsorbed interphase layer and softening of the non-adsorbed matrix resulting from these interactions make direct quantification of physicochemical effects on viscoelasticity challenging. The effects of the adsorbed interphase layer on viscoelasticity of bulk materials remains to be quantified and may require supporting spectroscopic techniques.

## REFERENCES

1. Allen, R. G., Little, D. N., and Bhasin, A. (2012). Structural characterization of micromechanical properties in asphalt using atomic force microscopy. *Journal of Materials in Civil Engineering*, 24(10), 1317-1327.
2. Allen, R.G., Little, D.N., Bhasin, A., and Lytton, R.L. (2013). Identification of the composite relaxation modulus of asphalt binder using AFM nanoindentation. *Journal of Materials in Civil Engineering*, 25(4), 530-539.
3. Al-Rawashdeh, A. (2012). Performance assessment of warm mix asphalt (WMA) pavements in presence of water by using nano scale techniques, and traditional laboratory tests. PhD Thesis. Ohio University, Athens, Ohio.
4. Anderson, D.A., Christensen, D.W., Bahia, H. U., Dongre, R., Sharma, M.G., Antle, C.E., and Button, J. (1994). Binder characterization and evaluation; Volume 3: Physical Characterization. SHRP-A-369, Strategic Highway Research Program, National Research Council, Washington, D.C.
5. Bahia, H., Faheem, A., and Hintz, C. (2011). NCHRP Research Results Digest 357: Test methods and specification criteria for mineral filler used in hot mix asphalt. *Transportation Research Board*, NCHRP Project No. 9-45, Contractor Final Report.
6. Bobko, C.P. (2008). Assessing the mechanical microstructure of shale by nanoindentation: The link between mineral composition and mechanical properties. Ph.D. Thesis. Massachusetts Institute of Technology, Cambridge, Massachusetts.
7. Bradshaw, R. D., and Brinson, L. C. (1997). A sign control method for fitting and interconverting material functions for linearly viscoelastic solids. *Mechanics of time-dependent materials*, 1(1), 85-108.
8. Buttlar, W. G., Bozkurt, D., Al-Khateeb, G. G., and Waldhoff, A. S. (1999). Understanding asphalt mastic behavior through micromechanics. *Transportation Research Record: Journal of the Transportation Research Board*, 1681(1), 157-169.
9. Christensen, R. M., and Freund, L. B. (1984). Theory of viscoelasticity, an introduction. *Journal of Applied Mechanics*, 51, 226.

10. Clopotel, C. (2012). Filler reinforcement mechanisms in asphalt mastics. Ph.D. Thesis. University of Wisconsin-Madison, Madison, Wisconsin.
11. Cost, T. L., and Becker, E. B. (1970). A multidata method of approximate Laplace transform inversion. *International Journal for Numerical Methods in Engineering*, 2(2), 207-219.
12. Cumberland, D. J., and Crawford, R. J. (1987). *The Packing of Particles*. Elsevier: New York.
13. Daniel, J. S., and Kim, Y. R. (1998). Relationships among rate-dependent stiffnesses of asphalt concrete using laboratory and field test methods. *Transportation Research Record: Journal of the Transportation Research Board*, 1630(1), 3-9.
14. De Moraes, M.B., Pereira, R.B., Simão, R.A., and Leite, L.F.M. (2010). High temperature AFM study of CAP 30/45 pen grade bitumen. *Journal of Microscopy*, 239(1), 46-53.
15. Dean, J., Bradbury, A., Aldrich-Smith, G., and Clyne, T. W. (2013). A Procedure for Extracting Primary and Secondary Creep Parameters from Nanoindentation Data. *Mechanics of Materials*, 65, 124-134.
16. Denby, E. F. (1975). A note on the interconversion of creep, relaxation and recovery. *Rheologica Acta*, 14(7), 591-593.
17. Duan, Z., An, Y., Zhang, J., and Jiang, H. (2012). The effect of large deformation and material nonlinearity on gel indentation. *Acta Mechanica Sinica*, 28(4), 1058-1067.
18. Fischer, H. Dillingh, E., and Hermse, C. (2012). On the interfacial interaction between bituminous binders and mineral surfaces as present in asphalt mixtures. *Applied Surface Science*, 265, 495-499.
19. Gonda, V., den Toonder, J., Beijer, J., Zhang, G. Q., and Ernst, L. J. (2005). Finite thickness influence on spherical and conical indentation on viscoelastic thin polymer film. *Journal of Electronic Packaging*, 127, 33.
20. Goodall, R., and Clyne, T. W. (2006). A critical appraisal of the extraction of creep parameters from nanoindentation data obtained at room temperature. *Acta Materialia*, 54(20), 5489-5499.

21. Hefer, A. W., Bhasin, A., and Little, D. N. (2006). Bitumen surface energy characterization using a contact angle approach. *Journal of Materials in Civil Engineering*, 18(6), 759-767.
22. Helm, C. A., Israelachvili, J. N., and McGuiggan, P. M. (1992). Role of hydrophobic forces in bilayer adhesion and fusion. *Biochemistry*, 31(6), 1794-1805.
23. Huang, C. C., Wei, M. K., and Lee, S. (2011). Transient and steady-state nanoindentation creep of polymeric materials. *International Journal of Plasticity*, 27(7), 1093-1102.
24. Hsu, W. Y., Giri, M. R., and Ikeda, R. M. (1982). Percolation transition and elastic properties of block copolymers. *Macromolecules*, 15(4), 1210-1212.
25. Hui, C. Y., Baney, J. M., and Kramer, E. J. (1998). Contact mechanics and adhesion of viscoelastic spheres. *Langmuir*, 14(22), 6570-6578.
26. Jäger, A., Lackner, R., and Eberhardsteiner, J. (2007). Identification of viscoelastic properties by means of nanoindentation taking the real tip geometry into account. *Meccanica*, 42(3), 293-306.
27. Ji, G., Ouyang, Z., and Li, G. (2010). Effects of adhesive thickness on global and local Mode-I interfacial fracture of bonded joints. *International Journal of Solids and Structures*, 47(18-19), 2445-2458.
28. Ji, G., Ouyang, Z., Li, G., Xu, W., Jerro, D., and Pang, S.-S. (2011). Effects of adhesive thickness on global and local mixed mode I/II interfacial fracture of bonded steel joints. *ASME 2011 Pressure Vessels and Piping Conference Proceedings*, 21-29.
29. Johnson, K. L. (1995). *Contact Mechanics*. Cambridge University Press, Cambridge.
30. Johnson, K. L., Kendall, K., and Roberts, A. D. (1971). Surface energy and the contact of elastic solids. *Proceedings of the Royal Society of London. A. Mathematical and Physical Sciences*, 324(1558), 301-313.
31. Kim, Y. R., Lee, Y. C., and Lee, H. J. (1995). Correspondence principle for characterization of asphalt concrete. *Journal of Materials in Civil Engineering*, 7(1), 59-68.

32. Kinloch, A. J. (1987). *Adhesion and adhesives: science and technology*. Springer Science and Business Media.
33. Lakes, R. (2009). *Viscoelastic Materials*. Cambridge University Press, Cambridge.
34. Leaderman, H. (1958). Viscoelastic phenomena in amorphous high polymeric systems. *Eirich's Rheology*, 2, 1-61.
35. Lee, E. H., and Radok, J. R. M. (1960). *The contact problem for viscoelastic bodies*. *Journal of Applied Mechanics* 27(3): 438-444.
36. Lee, E. H., Radok, J. R. M., and Woodward, W. B. (1959). Stress analysis for linear viscoelastic materials. *Journal of Rheology*, 3, 41.
37. Lee, H. J., Daniel, J. S., and Kim, Y. R. (2000). Continuum damage mechanics-based fatigue model of asphalt concrete. *Journal of Materials in Civil Engineering*, 12(2), 105-112.
38. Lesueur, D. (2009). The colloidal structure of bitumen: Consequences on the rheology and on the mechanisms of bitumen modification. *Advances in Colloid and Interface Science*, 145(1), 42-82.
39. Lesueur, D., Petit, J., and Ritter, HJ. (2013). The mechanisms of hydrated lime modification of asphalt mixtures: a state-of-the-art review. *Road Materials and Pavement Design* 14(1), 1-16.
40. Little, D. N. and Bhasin, A. (2006). Using surface energy measurements to select materials for asphalt pavement. *Transportation Research Board*, NCHRP Project No. 9-37, Contractor Final Report.
41. Little, D.N. and Petersen, J.C. (2005). "Unique effects of hydrated lime filler on the performance-related properties of asphalt cements: physical and chemical interactions revisited." *Journal of Materials in Civil Engineering*, 17(2), 207-218.
42. Lu, H., Wang, B., Ma, J., Huang, G., and Viswanathan, H. (2003). Measurement of creep compliance of solid polymers by nanoindentation. *Mechanics of Time-Dependent Materials*, 7(3-4), 189-207.
43. Lyne, A. L., Wallqvist, V. and Birgisson, B. (2013). Adhesive surface characteristics of bitumen binders investigated by Atomic Force Microscopy. *Fuel*, 113, 248-256.

44. Marasteanu, M. O., Basu, A., Hesp, S. A., and Voller, V. (2004). Time–Temperature Superposition and AASHTO MP1a Critical Temperature for Low-temperature Cracking. *International Journal of Pavement Engineering*, 5(1), 31-38.
45. Marchildon, R.P. and Hesp, S.A.M. (2011). Development of microindentation tests for the specification grading of asphalt cements. *International Journal of Pavement Research and Technology*, 4(4), 222-230.
46. Mattice, J. M., Lau, A. G., Oyen, M. L., and Kent, R. W. (2006). Spherical indentation load-relaxation of soft biological tissues. *Journal of Materials Research*, 21(08), 2003-2010.
47. Maugis, D. (1992). Adhesion of spheres: the JKR-DMT transition using a Dugdale model. *Journal of Colloid and Interface Science*, 150(1), 243-269.
48. Mun, S., Chehab, G. R., and Kim, Y. R. (2007). Determination of time-domain viscoelastic functions using optimized interconversion techniques. *Road Materials and Pavement Design*, 8(2), 351-365.
49. Odegard, G. M., Gates, T. S., and Herring, H. M. (2005). Characterization of viscoelastic properties of polymeric materials through nanoindentation. *Experimental Mechanics*, 45(2), 130-136.
50. Olesiak, S. E., Oyen, M. L., and Ferguson, V. L. (2010). Viscous-elastic-plastic behavior of bone using Berkovich nanoindentation. *Mechanics of Time-Dependent Materials*, 14(2), 111-124.
51. Oliver, W. C., and Pharr, G. M. (1992). Improved technique for determining hardness and elastic modulus using load and displacement sensing indentation experiments. *Journal of Materials Research*, 7(6), 1564-1583.
52. Ossa, E.A., and Collop, A.C. (2007). Spherical indentation behavior of asphalt mixtures. *Journal of Materials in Civil Engineering*, 19(9), 753-761.
53. Ossa, E.A., Deshpande, V.S., and Cebon, D. (2005). Spherical indentation behavior of bitumen. *Acta Materialia*, 53(11), 3103-3113.
54. Oyen, M. L. (2006). Analytical techniques for indentation of viscoelastic materials. *Philosophical Magazine*, 86(33-35), 5625-5641.

55. Oyen, M. L. (2013). Nanoindentation of biological and biomimetic materials. *Experimental Techniques*, 37(1), 73-87.
56. Oyen, M. L. (2004). Spherical indentation creep following ramp loading. *MRS Proceedings*, 841, R5-9.
57. Park, S. W., and Kim, Y. R. (2001). Fitting Prony-series viscoelastic models with power-law presmoothing. *Journal of Materials in Civil Engineering*, 13(1), 26-32.
58. Pauli, A. T., Grimes, W., Beemer, A. G., Turner, T. F., and Branthaver, J. F. (2011). Morphology of asphalts, asphalt fractions and model wax-doped asphalts studied by atomic force microscopy. *International Journal of Pavement Engineering*, 12(4), 291-309.
59. Pauli, A. T., Grimes, W., Huang, S. C., and Robertson, R. E. (2003). Surface energy studies of SHRP asphalts by AFM. *Preprint – American Chemical Society, Division of Petroleum Chemistry*, 48(1), 14-18.
60. Pauli, A. T., Grimes, W., Wang, M., Lu, P., and Huang, S. C. (2013). Development of an Adherence Energy Test via Force-Displacement Atomic Force Microscopy (FD-AFM). *Multi-Scale Modeling and Characterization of Infrastructure Materials Proceedings*, RILEM Bookseries 8, 273-284.
61. Pellinen, T. K., Witczak, M. W., and Bonaquist, R. F. (2003). Asphalt mix master curve construction using sigmoidal fitting function with non-linear least squares optimization. *15th Engineering Mechanics Division Conference Proceedings*, 83-101.
62. Qiang, B., Greenleaf, J., Oyen, M., and Zhang, X. (2011). Estimating material elasticity by spherical indentation load-relaxation tests on viscoelastic samples of finite thickness. *IEEE Transactions on Ultrasonics, Ferroelectrics, and Frequency Control*, 58(7), 1418-1429.
63. Scher, H., and Zallen, R. (1970). Critical density in percolation processes. *The Journal of Chemical Physics*, 53(9), 3759-3761.
64. Shashidhar, N., and Romero, P. (1998). Factors affecting the stiffening potential of mineral fillers. *Transportation Research Record: Journal of the Transportation Research Board*, 1638, 94-100.

65. Shashidhar, N., and Shenoy, A. (2002). On using micromechanical models to describe dynamic mechanical behavior of asphalt mastics. *Mechanics of Materials*, 34(10), 657-669.
66. Shull, K. R. (2002). Contact mechanics and the adhesion of soft solids. *Materials Science and Engineering: R: Reports*, 36(1), 1-45.
67. Sirghi, L., Ponti, J., Broggi, F., and Rossi, F. (2008). Probing elasticity and adhesion of live cells by atomic force microscopy indentation. *European Biophysics Journal*, 37(6), 935-945.
68. Sirghi, L., and Rossi, F. (2006). Adhesion and elasticity in nanoscale indentation. *Applied Physics Letters*, 89(24), 243118-243118.
69. Sneddon, I. N. (1965). The relation between load and penetration in the axisymmetric Boussinesq problem for a punch of arbitrary profile. *International Journal of Engineering Science*, 3(1), 47-57.
70. Song, S., Paulino, G., and Buttlar, W. (2006). A bilinear cohesive zone model tailored for fracture of asphalt concrete considering viscoelastic bulk material. *Engineering Fracture Mechanics*, 73(18), 2829-2848.
71. Tarefder, R. A., Zaman, A. M., and Uddin, W. (2010). Determining hardness and elastic modulus of asphalt by nanoindentation. *International Journal of Geomechanics*, 10(3), 106-116.
72. Tarefder, R. and Faisal, H. (2013). Effects of dwell time and loading rate on the nanoindentation behavior of asphaltic materials. *Journal of Nanomechanics and Micromechanics*, 3(2), 17-23.
73. Tarefder, R., and Faisal, H. (2013). Modeling nanoindentation creep behavior of asphalt binder. *Advances in Civil Engineering Materials*, 2(1), 418-440.
74. Tarefder, R. and Faisal, H. (2014). Nanoindentation characterization of asphalt concrete aging. *Journal of Nanomechanics and Micromechanics*, 4(1), 1-8.
75. Ting, T. C. T. (1966). The contact stresses between a rigid indenter and a viscoelastic half-space. *Journal of Applied Mechanics*, 33, 845.

76. Tweedie, C. A., and Van Vliet, K. J. (2006). Contact creep compliance of viscoelastic materials via nanoindentation. *Journal of Materials Research*, 21(6), 1576-1589.
77. Underwood, B. S. (2011). Multiscale constitutive modeling of asphalt concrete. PhD Thesis. North Carolina State University, Raleigh, North Carolina.
78. Underwood, B. S., and Kim, Y. R. (2009). Determination of the appropriate representative elastic modulus for asphalt concrete. *International Journal of Pavement Engineering*, 10(2), 77-86.
79. Veytskin, Y., Bobko, C.P., and Castorena, C. (2015, under review). Nanoindentation and atomic force microscopy investigations of asphalt binder and mastic. *Journal of Materials in Civil Engineering (ASCE)*.
80. Veytskin, Y., Bobko, C.P., and Castorena, C. (2014). Nanoindentation investigation of asphalt binder and mastic viscoelasticity. *International Journal of Pavement Engineering* ahead-of-print, 1-14.
81. Veytskin, Y., Bobko, C.P., Castorena, C., and Kim, Y.R. (2015, under review). Nanoindentation investigation of asphalt binder and mastic cohesion. *Mechanics of Materials*.
82. Wu, S., Pang, L., Mo, L., Chen, Y., Zhu, G. (2009). Influence of aging on the evolution of structure, morphology and rheology of base and SBS modified bitumen. *Construction and Building Materials*, 23(2), 1005-1010.
83. Xu, X.-P., and Needleman, A. (1994). Numerical simulations of fast crack growth in brittle solids. *Journal of the Mechanics and Physics of Solids*, 42(9), 1397-1434.
84. Yu, N., Polycarpou, A. A., and Conry, T. F. (2004). Tip-radius effect in finite element modeling of sub-50 nm shallow nanoindentation. *Thin solid films*, 450(2), 295-303.
85. Yu, X., Burnham, N. A., Mallick, R.B. and Tao, M. (2013). A systematic AFM-based method to measure adhesion differences between micron-sized domains in asphalt binders. *Fuel*, 113, 443-447.
86. Zhu, Y., Sun, L., and You, K. (2009). Viscoelastic analysis of asphalt pavement using a regularized interconversion technique between creep and relaxation. *9th*

*International Conference of Chinese Transportation Professionals Proceedings*,  
2159-2164.

87. Zofka, A., and Nener-Plante, D. (2011). Determination of asphalt binder creep compliance using depth-sensing indentation. *Experimental Mechanics*, 51(8), 1365-1377.

# APPENDICES

## APPENDIX A

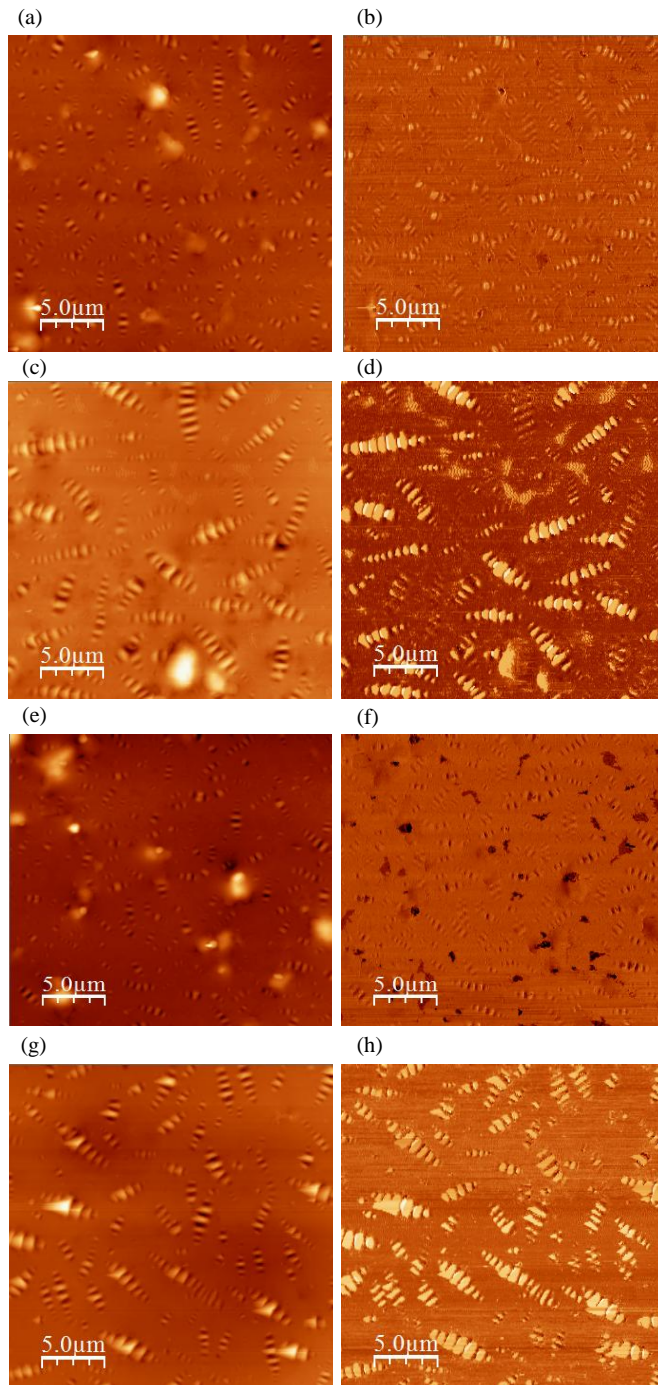


Figure A.1: (a) PG 70-28 SBS, 1.29 DR lime (height); (b) PG 70-28 SBS, 1.29 DR lime (phase); (c) PG 70-28 SBS, 0.6 DR lime (height); (d) PG 70-28 SBS, 0.6 DR lime (phase); (e) PG 70-28 SBS, 1.2 DR granite (height); (f) PG 70-28 SBS, 1.2 DR granite (phase); (g) PG 70-28 SBS, 0.6 DR granite (height); (h) PG 70-28 SBS, 0.6 DR granite (phase)

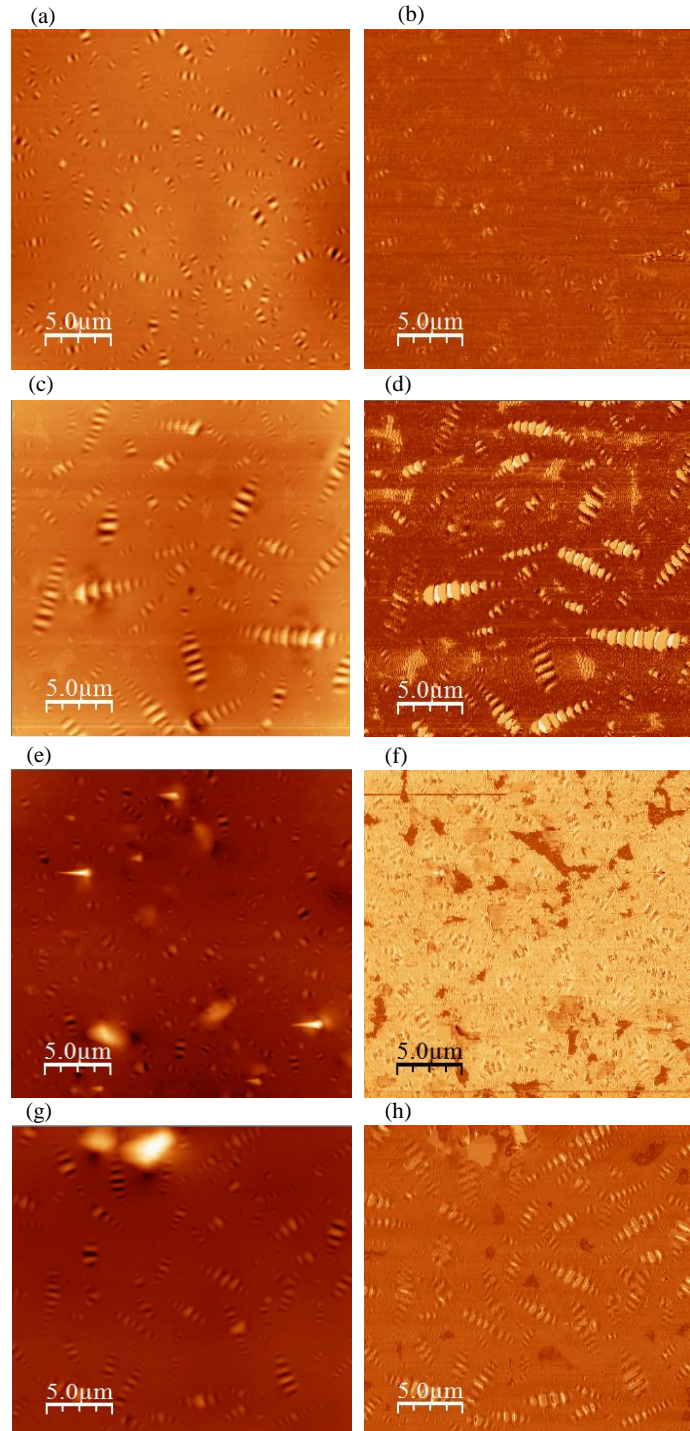


Figure A.2: (a) PG 70-22, 1.26 DR lime (height); (b) PG 70-22, 1.26 DR lime (phase); (c) PG 70-22, 0.6 DR lime (height); (d) PG 70-22, 0.6 DR lime (phase); (e) PG 70-22, 1.2 DR granite (height); (f) PG 70-22, 1.2 DR granite (phase); (g) PG 70-22, 0.6 DR granite (height); (h) PG 70-22, 0.6 DR granite (phase)

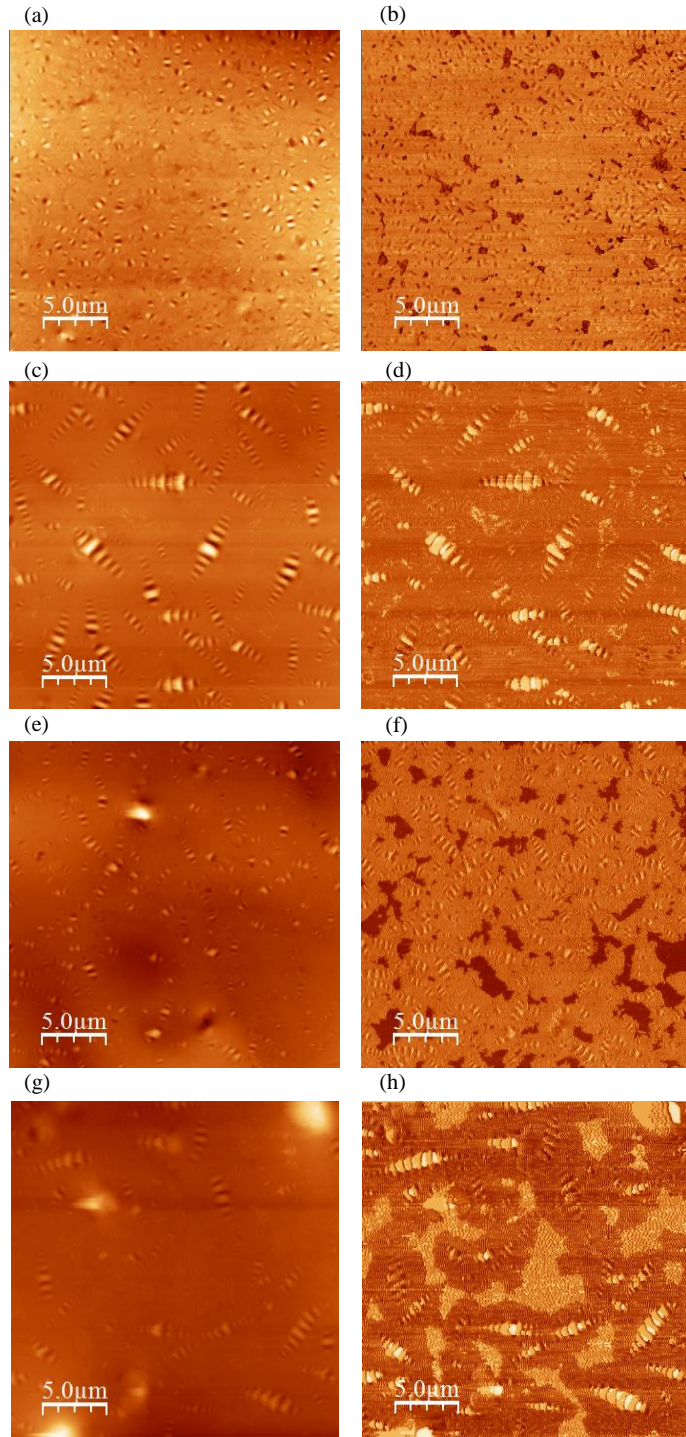


Figure A.3: (a) PG 64-22, 1.2 DR lime (height); (b) PG 64-22, 1.2 DR lime (phase); (c) PG 64-22, 0.6 DR lime (height); (d) PG 64-22, 0.6 DR lime (phase); (e) PG 64-22, 1.2 DR granite (height); (f) PG 64-22, 1.2 DR granite (phase); (g) PG 64-22, 0.6 DR granite (height); (h) PG 64-22, 0.6 DR granite (phase)

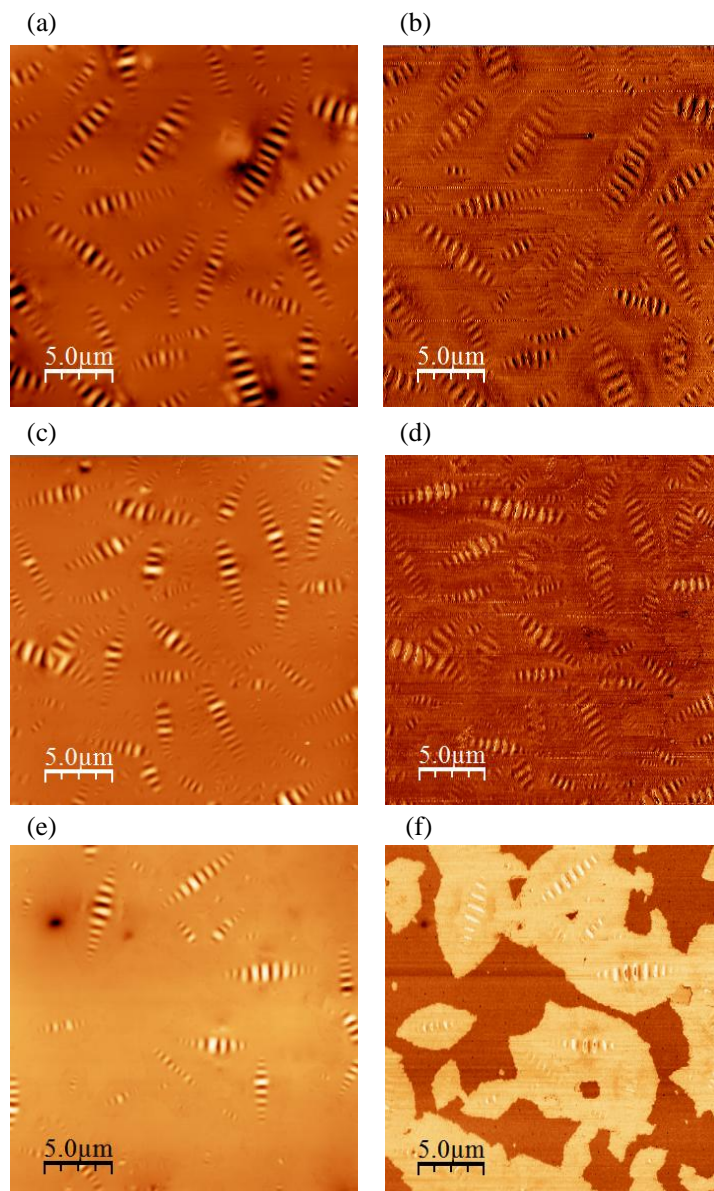


Figure A.4: (a) PG 70-28 SBS (height); (b) PG 70-28 SBS (phase); (c) PG 70-22 (height); (d) PG 70-22 (phase); (e) PG 64-22 (height); (f) PG 64-22 (phase)